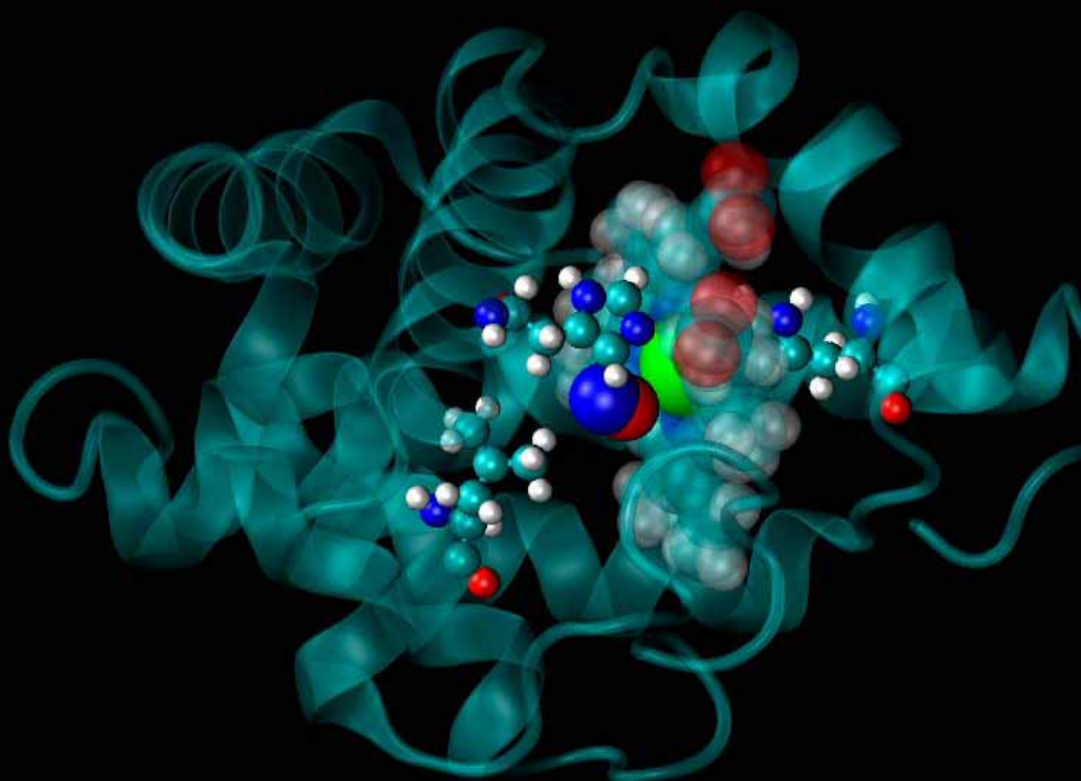
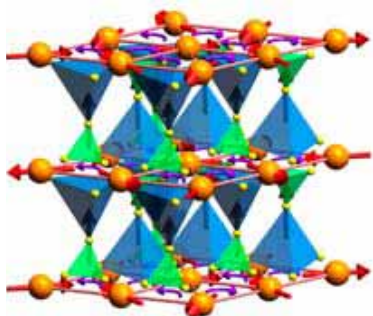
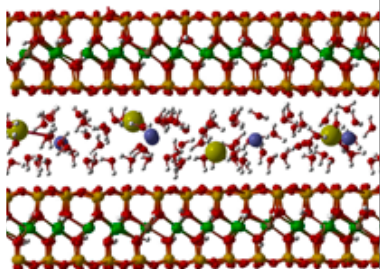


PAUL SCHERRER INSTITUT



Ultrafast Phenomena at the Nanoscale:

Science opportunities at the SwissFEL X-ray Laser



Cover Figures Descriptions

Right: Myoglobin interacting with small ligands (here nitric oxide) is one of the best-studied biochemical systems and allows the testing of experimental and computational strategies. Of primary interest are how chemical selectivity and biological function arise. The SwissFEL will expand and improve our knowledge about fundamental aspects of function and control at a molecular level. Courtesy of M. Meuwly, University of Basel.

Upper left: Understanding the diffusion of ions such as Cs and Na (blue and yellow spheres, respectively) between the layers of the mineral montmorillonite is a key step towards developing a realistic model for the movement of radioactive wastes in the environ-

ment. With the SwissFEL, we will be able to follow the diffusion in real time and hence test theoretical models at the nanometer scale. Courtesy of S. Churakov, PSI.

Lower left: The multiferroic state in $\text{RbFe}(\text{MoO}_4)_2$, as envisaged by M. Kenzelmann, ETHZ and PSI. Ordering of the magnetic moments (red arrows on the orange Fe atoms) leads to alternating spin currents on the triangles (pink arrows), which, together with the alternating crystal field environment, generate a macroscopic ferroelectric polarization (transparent vertical blue arrows). Using the SwissFEL, one may study the transient effect of an applied electric field on the magnetic order, with potential applications in novel switching devices.

Editorial Board

Bruce D. Patterson

Laura Heyderman
Chris Milne
Pierre Thibault
Kurt Ballmer
Urs Staub

Chairman

Magnetization Dynamics
Solution Chemistry and Surface Catalysis
Coherent Diffraction
Ultrafast Biochemistry
Correlated Electron Materials

With contributions from:

General

Abela, R. (PSI)
Braun, H. (PSI)
Mesot, J. (EPFL, ETHZ, PSI)
Ming, P. (PSI)
Pedrozi, M. (PSI)
Quitmann, Ch. (PSI)
Reiche, S. (PSI)
Shiroka, T. (ETHZ)
van Daalen, M. (PSI)
van der Veen, J.F. (ETHZ, PSI)

Magnetization Dynamics

Allenspach, R. (IBM Lab, Rüschlikon)
Back, Ch. (Univ. Regensburg)
Brune, H. (EPFL)
Eisebitt, S. (BESSY, Berlin)
Fraile Rodriguez, A. (PSI)
Gambardella, P. (ICN, Barcelona)
Hertel, R. (FZ Jülich)
Kenzelmann, M. (ETHZ, PSI)
Kläui, M. (Univ. Konstanz)
Nolting, F. (PSI)

Nowak, U. (Univ. Konstanz)
Rønnow, H. (EPFL)
Vaterlaus, A. (ETHZ)

Solution Chemistry and Surface Catalysis

Bressler, Ch. (EPFL)
Chergui, M. (EPFL)
Churakov, S. (PSI)
van Bokhoven, J. (ETHZ)
van der Veen, R. (EPFL, PSI)
Wokaun, A. (ETHZ, PSI)
Wolf, M. (FU Berlin)
Zietz, B. (EPFL, PSI)

Coherent Diffraction

Bunk, O. (PSI)
Diederichs, K. (Univ. Konstanz)
Froideval, A. (PSI)
Howells, M. (ESRF, Grenoble)
Kewish, C. (PSI)
Ourmazd, A. (Univ. Wisconsin)
Pfeiffer, F. (EPFL, PSI)
Robinson, I. (UC London)

Samaras, M. (PSI)
Schmitt, B. (PSI)
Schulze-Briese, C. (PSI)
van der Veen, J.F. (ETHZ, PSI)
van Swyghoven-Moens, H. (EPFL, PSI)

Ultrafast Biochemistry

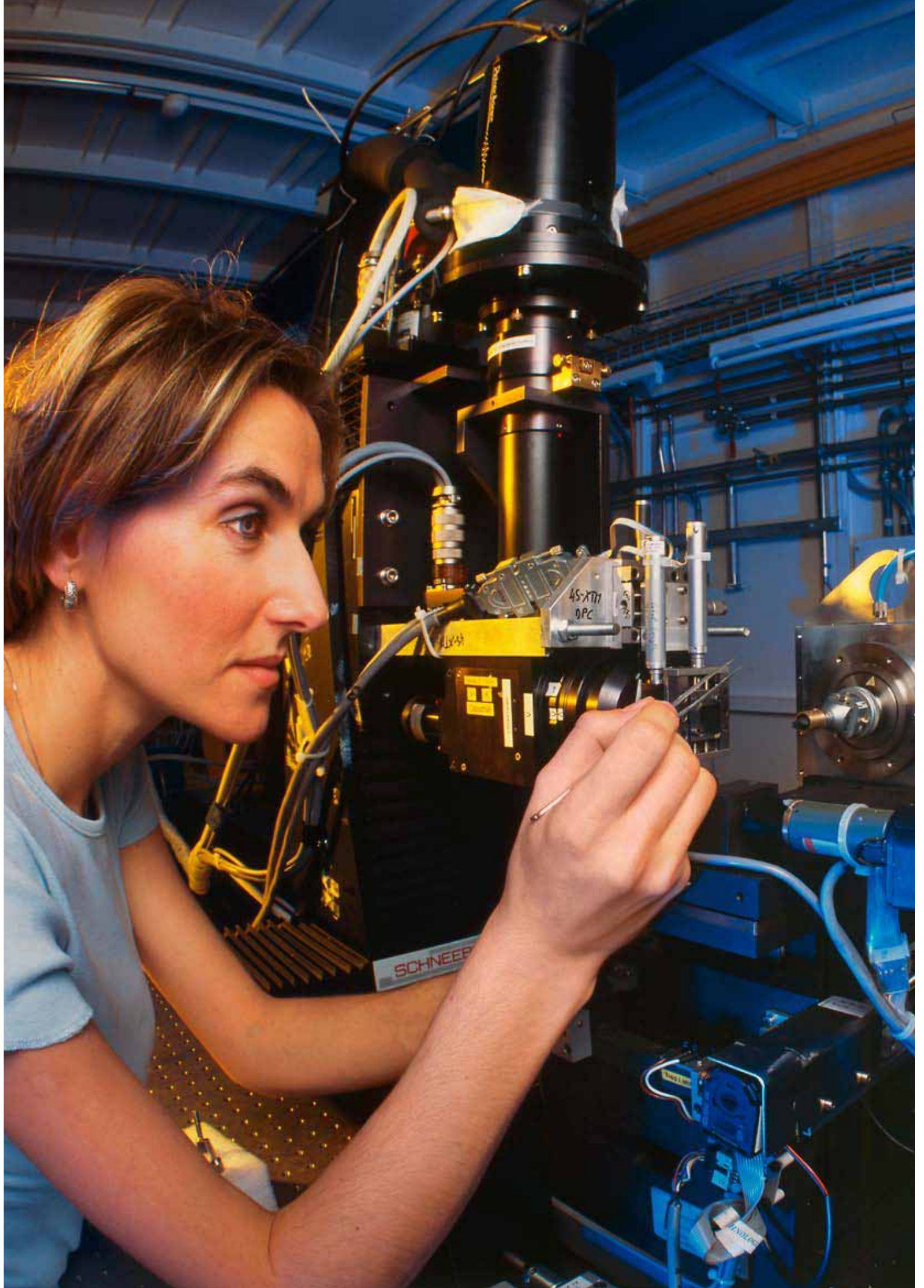
Chergui, M. (EPFL)
Kjelstrup, S. (NTNU, Trondheim)
Meuwly, M. (Univ. Basel)
Schuler, B. (Univ. Zurich)
van Thor, J. (IC, London)

Correlated Electron Materials

Chumakov, A. (ESRF, Grenoble)
Hengsberger, M. (Univ. Zurich)
Johnson, S. (PSI)
Mesot, J. (EPFL, ETHZ, PSI)
Osterwalder, J. (Univ. Zurich)
Schmitt, Th. (PSI)
Strocov, V. (PSI)
Wolf, M. (FU Berlin)

Table of contents

5	Foreword
6	Scientific Challenges
10	Introduction and Project Overview
18	I. Ultrafast Magnetization Dynamics on the Nanoscale Temporal spin behavior in magnetic solids at short length scales
32	II. Catalysis and Solution Chemistry Structure and lifetime of short-lived molecular states in solution or on a catalyst surface
46	III. Coherent Diffraction by Nanostructures Atomic-resolution structure of biological and inorganic nanostructures with lens-less imaging
62	IV. Ultrafast Biochemistry Initial events and fluctuations in biochemical processes at the atomic scale
76	V. Time-Resolved Spectroscopy of Correlated Electron Materials Mapping the flow of energy among strongly-coupled degrees of freedom
94	Machine and Building
102	Appendix A: The SwissFEL Science Workshop Series
106	Appendix B: Current SwissFEL Research Projects



From molecular pictures to molecular movies

In today's fast-moving society, standing still is effectively synonymous with being left behind. If it is to maintain, beyond the coming 10–15 years, its high international standing as a complex of large research infrastructures, the Paul Scherrer Institute (PSI) must now lay the foundation for a competitive future.

Experts worldwide foresee a strongly growing demand within science and technology for photon sources delivering ultra-short, coherent X-ray pulses. Such a source, called a free electron laser (FEL), is nothing less than a gigantic flash camera, allowing us to take a deeper look into matter than with any other machine before. By literally seeing molecules in action, scientists will be able not only to capture chemical and biological processes of direct relevance and benefit to society but also to improve them. It is a dream coming true! For the first time, it will not only be possible to take pictures of molecular structures, we will be able to make movies of their motion.

The new X-ray laser project at PSI, known as SwissFEL, will be an important addition to the existing complex of PSI facilities that serve interdisciplinary and international research teams from academia and industry. The SwissFEL is an essential element of Switzerland's strategic focus and will prolong our nation's leading position in scientific research for years to come. It will attract top scientists from Switzerland and abroad, and will strengthen the position of PSI as a world-class research institute. This new high-tech facility will also provide an important incentive for Swiss industry, through which existing highly-qualified jobs will be maintained and new ones created.

In the following pages, we present a wide range of important, open questions within science and engineering disciplines that SwissFEL will contribute towards solving. These questions, which form the 'scientific case' for SwissFEL, have been identified through a range of workshops organized over the past few years and by consultation with individual leading scientists. The scientific case presented here is the result of hard and dedicated work by about 20 research groups from Swiss universities and research institutes, as well as by PSI staff. It shows that Switzerland has an active scientific community eager to use the unique properties of SwissFEL, be it for optimizing catalytic processes, identifying polluting molecules, designing new pharmaceutical drugs or studying defects in engineering materials. As is usual with new facilities, new applications will emerge that no-one had ever imagined before. This is science and technology at its best, and PSI will be proud and honoured to make SwissFEL a reality.



Joël Mesot
Director, Paul Scherrer Institut

Scientific Challenges

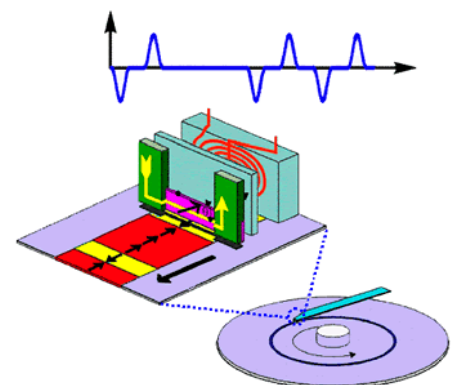
Three dominant trends in today's science and technology are 'smaller', 'faster' and 'more complex'. Nanotechnology entails the measurement and manipulation of matter on the molecular scale. The relevant time scale for dynamic processes is then the 'ultrafast' domain, defined by the femto-second vibration of an atom in a chemical bond. Complexity, which may manifest itself as chemical diversity, non-equilibrium states, and/or the lack of crystalline order, holds the promise of advanced materials with enhanced functionality. The predominant tool for investigating matter is *light*; the SwissFEL X-ray laser will be a unique light source which will expand the frontiers of knowledge – at the nanoscale, of ultrafast phenomena and in complex materials.

In close consultation with experts representing a wide range of scientific research, a selection was made of particularly relevant applications for the SwissFEL. As detailed below, the present Science Case emphasizes dynamical investigations of condensed matter and the "pre-damage" imaging of nanostructure objects. Further possibilities include time-resolved spectroscopy of plasmas and molecular gases, the study of *sub*-femto-second electron dynamics, the generation with intense X-ray pulses of new states of matter, and probing fundamental interactions.

The SwissFEL project has been conceived to address pressing scientific challenges of importance to society, in which it will doubtless make ground-breaking contributions. Possibilities for future upgrades have been included in the design. As with all cutting-edge scientific research, it is the talent of the operators and the creativity of the users that will ultimately reveal the most dramatic benefits of this powerful new instrument.

Magnetism: materials and processes for tomorrow's information technology

The astounding pace of development of modern technology mirrors society's demand for high-performance devices, such as computers and mobile telephones. These devices involve ever-increasing complexity, smaller components and higher data-storage capacity, which in turn demands the technological advancement of magnetic systems and poses ever more fundamental questions involving magnetism at faster time scales and on smaller length scales. Such demands and questions fuel new possibilities for exceptional measurements with the SwissFEL. Consider the example of current-induced magnetic domain-wall motion: although predicted over thirty years ago, it is only through recent advances in film deposition, lithography and



measurement instrumentation that this important effect could be implemented, quantified and understood.

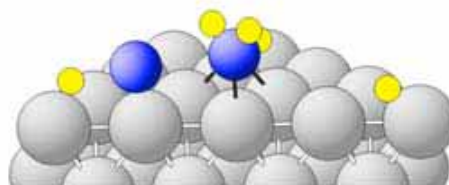
When it comes to developing a sound scientific basis for future applications of magnetism, we are faced with three major challenges. Firstly, we need to understand novel interactions within a magnetic system, such as spin-torque phenomena involving a spin current, or the manipulation of spin structures with laser pulses. Secondly, magnetic technology needs to be faster, moving to the femto-second regime, in order to dramatically accelerate information transfer. For this, it will be essential to understand and develop ultrafast magnetic processes. Finally, the development of new magnetic materials and the understanding of their behavior will be essential. This includes nanoscale magnets, which will meet the need for smaller device components, and complex multi-component systems, with multifunctional properties.

If we are to continue to address the major challenges in magnetism and to develop new technologies based on magnetic materials, it will be essential to understand the fundamental processes in magnetic systems. For this, the SwissFEL will be a powerful tool, with its combination of variable polarization – to provide magnetic sensitivity, spatial resolution – to reveal the details of the spin structures, temporal resolution – to observe both repetitive and stochastic magnetic events, and elemental specificity – to discern these processes in the individual components of a complex magnetic system.

Catalysis and solution chemistry: for a clean environment and a sustainable energy supply

Chemistry is the study of molecules and their reactions. Whether the molecules are biochemical in nature and located in the human body, or catalytic in functionality and located in the exhaust system of an automobile, their reactivity is determined by the interplay between their electronic and geometric structures. The ability to observe the fundamental first steps of a chemical reaction requires both spatial and temporal resolution. The SwissFEL will provide access to both the nanometer length scale – small enough to see the motion of small molecules – and the femto-second time scale – fast enough to resolve the vibration of molecular bonds. Researchers will be able to watch structural changes and electronic energy shifts, as chemical reactions take place in solution or on catalytic surfaces, resulting in the long-sought ‘molecular movie’.

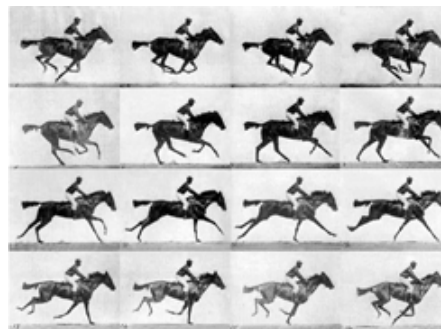
The challenge facing us is to make full use of this novel X-ray source, by developing techniques that probe the primary events in chemical processes. In Chapter II of this document, several methods are proposed that will exploit the SwissFEL to the full; whether we examine how the surface of a platinum nanocrystal enhances the conversion of carbon monoxide to carbon dioxide, or we measure how the spin-state of an iron atom at the center of a protein affects its ability to bind oxygen and deliver it to distant tissue, the results will be ground-breaking. By deepening our understanding of how structural arrangement and electronic configuration affect chemical reactivity, we will be able to design better catalysts, resulting in faster and cleaner chemical processes, as well as more efficient energy conversion and storage. As with any scientific endeavor, the impact of these measurements is unpredictable and will be judged by future generations. But being able to visualize molecular reactions, as they occur, has the potential to do nothing less than to revolutionize chemistry as a field of research.



Coherent diffraction: flash photography of matter

The common saying “*seeing is believing*” neatly summarizes the importance of making things visible. A century ago, Muybridge took a series of photographs of a galloping horse, convincing us that all four hooves do indeed leave the ground for a brief moment. Today, our imaging methods have been refined to the point where even fantasy becomes reality. However, what has remained a dream is taking snapshots so fast that even single atoms in the photographed object remain frozen at their positions. The SwissFEL produces extremely short X-ray pulses, corresponding to a ‘shutter time’ of just a few femto-seconds, enabling a series of such exposures (a ‘movie’) to be made.

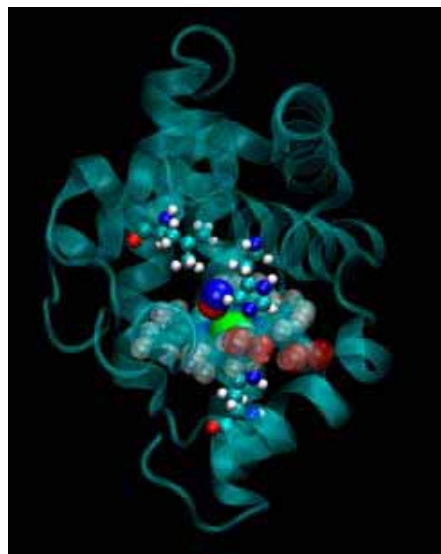
There is, however, an important difference with respect to traditional photography: a single SwissFEL pulse is so intense that the exposed part of the object is blasted away during the snapshot. This is both a blessing and a curse. The blessing is that the picture has already been taken before the object disintegrates; the curse is that the object has disappeared before a second picture can be taken. Hence, repeated pictures can only be taken if many copies of the object exist. Molecules are an example, and this is why molecular imaging is one of the great opportunities for the SwissFEL. Among the most important molecules to image are the proteins in our cell membranes, which control our life-processes, but whose structures have largely remained elusive. If copies can be made to form small crystals, this will be enough to take a single-shot picture of the molecule’s form and internal structure. If they cannot be crystallized, which often is the case, then a stream of copies of the single molecule can be made to pass the X-ray beam, thus allowing a repetition of snapshots, to make even the faintest of objects (e.g., small molecules) visible. Another difference with respect to everyday photography is that the flash images are made without a lens – the images are directly constructed from the angular distribution of the X-ray waves scattered by the object. PSI is one of the world-leading laboratories in diffractive imaging, thanks in large part to the unique pixel-detector technology which it has developed for this purpose. PSI is ready to take on these challenges. The benefits of this extraordinary type of flash photography with X-rays will be huge. Not only do we have a chance to unravel the structure of biological matter, but also to develop new drugs, to make movies of rupturing steel and hence improve its strength, and to visualize defects in electronic devices and make them better.



Biochemistry: shedding light on the processes of life

Life is sustained by processes occurring in the biomolecules, mainly proteins, that make up living tissue and organisms. The function of proteins is closely associated with their structural state, and synchrotron-based structural biology has been highly successful in determining the static structures of many proteins of vital importance to mankind. But functioning proteins are anything but static; important changes occur on a wide range of time scales, from hours to femto-seconds.

Studying the dynamics and kinetics of biochemical reactions is a very challenging endeavor. When applied with femto-second time resolution, optical spectroscopy matches the timescale of fundamental processes and covers frequencies that probe electronic and nuclear motion, but it does not include wavelengths of the order of



the chemical bond length. Hard X-rays from the SwissFEL will provide access to the nanometer length scale, small enough to see the motion of individual molecules and even of single atoms.

Structural changes in biological molecules can currently be resolved using pulsed X-rays at time scales of 0.1 - 1 milli-seconds, and in exceptional cases down to 100 pico-seconds, sufficient to follow modifications in the chemical environment of specific protein domains. Ideally, one wants to be able to sample the multiple transition states that are a general feature of biomolecules undergoing structural and functional changes. The SwissFEL will be able to detect the vibration of individual molecular bonds at the femto-second time scale typical of molecular vibrations.

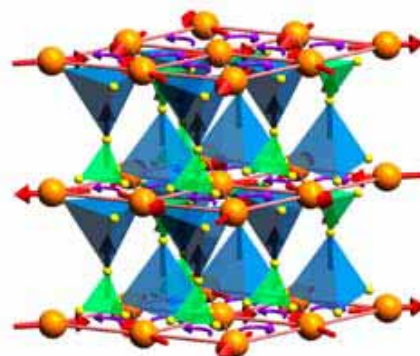
The promise of the SwissFEL is to allow biochemists, with techniques such as X-ray scattering in solution, X-ray diffraction by crystals and X-ray absorption spectroscopy, to observe the rapid structural changes undergone by biomolecules. Immediate systems to be analyzed are oxidation-reduction and photochemically active proteins, where relatively small reaction centers undergo dramatic structural changes, as well as the fundamental processes in natural and artificial photosynthesis, which are of paramount importance for the global energy supply. The challenge will be to develop new technologies and methods, which take full advantage of the novel X-ray source, to detect subtle functional changes in large, biologically-relevant proteins. This will truly add the fourth dimension of time to the discipline of structural biology.

Correlated electrons: the fascination of new materials

Correlated electron systems lie at the heart of modern information technology. They provide physics with some of its most elegant systems and encompass its most challenging problems. In one limit, where the electrons are completely delocalized, we have the metallic state. Here, theoretical work based on the idea of electrons forming a *liquid* with quantum mechanical properties has formed the cornerstone of our understanding of normal metals since its inception in the 1950's.

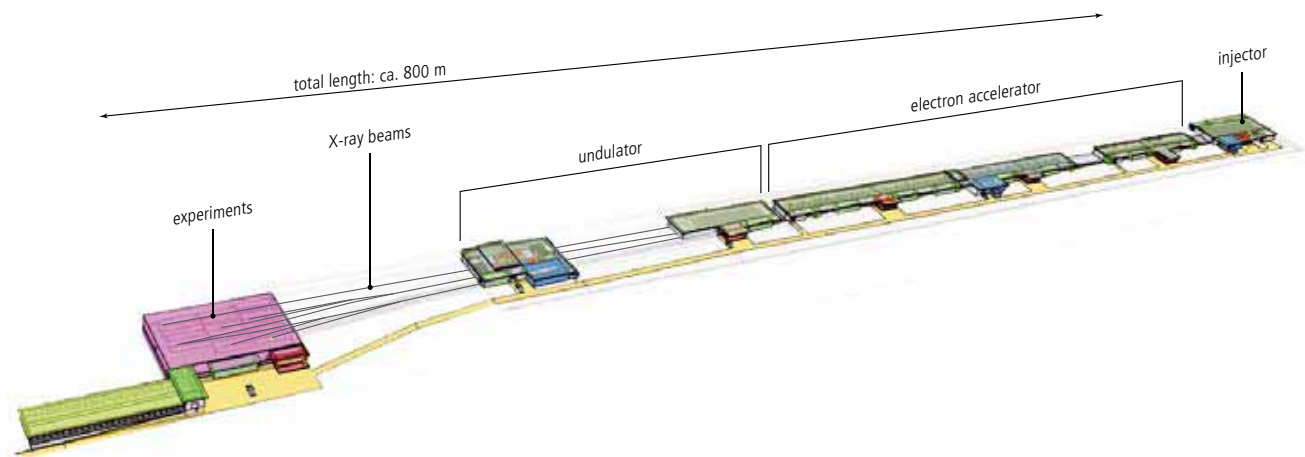
In the opposite limit, the electrons are localized on the lattice sites of a system, and, as a consequence, the system is an *insulator*. Interactions between electrons, spins and the lattice may then give rise to various types of ordered / disordered states. Much of contemporary condensed matter physics is concerned with developing a unified description of these states, and with finding an explanation of how new exotic ground-states, displaying properties such as superconductivity, emerge from them.

Increasing experimental and theoretical evidence indicates that fast fluctuations at the nanometer scale are at the origin of the complex phase diagrams reported, for example, in magneto-resistive manganites or in superconducting cuprates. Experiments at the SwissFEL facility will allow us, on the one hand, to image the dynamics of the various degrees of freedom at the molecular level, and on the other hand, by means of pump-probe techniques, to investigate how co-existing or competing states are inter-related. Such information is essential for a deeper theoretical understanding of these fascinating materials and for realizing their large potential for technological innovation.



Introduction and Project Overview

The SwissFEL – a national facility for ultrafast phenomena at the nanoscale



Organization of the SwissFEL Science Case

The present document, the Science Case for the SwissFEL project, is organized as follows:

- An introduction defines the mission, strategy and design considerations of the facility and places the project in the national and international research arenas. Overviews are given of the project organization and time-schedule.
- The scientific case for the SwissFEL, in the research areas of magnetism, chemistry and catalysis, imaging of nanostructures, biochemistry and novel materials, is then presented in five chapters, written at approximately the level of a graduate student in natural science. A number of blue “Infoboxes” have been included to provide additional background information.
- The operating principle and the proposed design of the SwissFEL machine and building are then briefly presented.
- The appendices list the scientific workshops which have formed the basis of this scientific case and the research projects which have been initiated to develop ideas relating to the SwissFEL machine and its applications.

Scientific Motivation

The SwissFEL X-ray free electron laser (FEL) will allow us to take an in-depth look into matter in motion. Operating as a flash camera, it will take snapshots on extremely short length and time scales. The SwissFEL will help us to understand and optimize processes of direct relevance to society, for example in clean energy production and pollution abatement, high-performance information technology, and the vital biochemical functions of living cells. The SwissFEL will be a *discovery machine*, enabling us to capture these processes for the first time, in action, and at the molecular level. The SwissFEL will be a research tool whose mission is to understand and improve our environment and to promote innovation in Switzerland.

Realization

The SwissFEL embodies the strategy of the Paul Scherrer Institut: a) to build and operate large facilities to perform cutting-edge interdisciplinary research in physics, chemistry, biology, energy technology, environmental sciences and medicine, b) to support universities and vocational schools in the training of scientists, engineers and technical staff, and c) to promote the transfer of research results to industry. The specifications and design of the SwissFEL are determined by the scientific demands of the users, on the one hand, and by the technical expertise of the machine scientists, on the other. Essential to the project strategy is construction of the facility at PSI, where the required expertise in photon science and machine physics is available, and where research teams, in collaboration with Swiss academia, will be able to achieve the ambitious goals.

The SwissFEL will be realized *for users by users*, to address important societal needs in energy supply, novel materials, a cleaner environment and health care. With its emphasis on ultrafast processes at the nanoscale, the SwissFEL will significantly expand the existing PSI large facilities Swiss Light Source (SLS) and Swiss Neutron Source (SINQ). And as is the case with these facilities, the SwissFEL will be tightly networked to the international scientific community.

International context

The SwissFEL has a number of unique features which distinguish it from other X-ray FEL projects worldwide. The SwissFEL will deliver *hard* X-ray pulses, down to 1 Å (= 0.1 nanometer) wavelength, as will only three other projects: LCLS (Stanford), SCSS (Harima, Japan) and the European X-FEL (Hamburg) (see Table 11). Of these, only the LCLS is presently in operation. Other projects, mostly in the planning phase, are concerned with the construction of *soft* X-ray FELs, with wavelengths which are too long to spatially resolve molecules in matter.

Project	Start of operation	Electron beam energy	Minimum photon wavelength (λ_{\min})	Peak brilliance @ λ_{\min}	Repetition rate	Number of X-ray pulses/macropulse
		GeV	Å	10^{33} ph / s mm ² mrad ² 0.1 % b.w.	macro-pulses/sec.	
LCLS	2009	13.6	1.5	1	120	1
SCSS	2010	8	1.0	0.5	60	1
European X-FEL	2014	17.5	1.0	5	10	3250
SwissFEL	2016	5.8	1.0	0.1 – 1	100	2

Table I1. A comparison of the SwissFEL with approved hard X-ray FEL projects.

In comparison to the LCLS in Stanford and the European X-FEL in Hamburg, the SwissFEL will be more compact and cost-effective, thanks to a low electron-beam emittance, low charge-per-pulse, compact undulators, and optimization of the FEL process. Whereas the European X-FEL will produce bursts of high-repetition rate X-rays, the SwissFEL will be operated at a constant pulse rate, well-matched to the read-out time of PSI's world-leading 2-dimensional X-ray detectors. Another unique aspect of the SwissFEL will be the use of synchronized far-infrared terahertz radiation from an independent source, to switch magnetic devices and prepare excited molecules, prior to being probed with the X-ray pulses.

Free electron lasers amplify light by accelerating an electron beam to almost the speed of light in a linear accelerator and then passing it through a long undulator. This is completely different from conventional lasers. The latter, of normal laboratory size, are being improved to reach shorter wavelengths, by "high harmonic generation" (HHG) frequency conversion. In Europe, there are two large projects based on this principle (ELI and HiPER). HHG sources will operate in the vacuum-ultraviolet (VUV) and soft X-ray wavelength regions, albeit within a much more limited spectral range and a much lower average flux than the FELs. Intense *hard* X-ray pulses, down to 1 Å wavelength, can only be generated in a high-energy free electron laser such as the SwissFEL. To further enhance performance, it is planned to use the HHG effect to "seed" the SwissFEL pulses, implying a close collaboration with the high-power conventional laser community.

A facility serving national needs – "SwissFEL: a Swiss FEL"

The principal scientific areas of investigation to be covered by the SwissFEL have been identified in close consultation with Swiss research groups, and a series of workshops was held on a range of disciplines (see Appendix A). The science case presented in the following chapters reflects these topics, and it includes contributions from the colleagues listed on the inside cover. We estimate that at present more than 20 Swiss research groups have an immediate need for the capabilities of the SwissFEL, and the number of inter-

ested groups is expected to increase, reflecting the growing international commitment to the study of ultrafast phenomena. In addition, Swiss laser and accelerator experts are discussing joint projects, e.g., for innovative seeding schemes for the SwissFEL. Meanwhile, PSI and the ETHZ are in the process of establishing a Joint Professorship in Ultrafast Hard X-ray Physics and a Center for Ultrafast Science. Collaborative research efforts with the ETHZ and EPFL and with Swiss cantonal universities are underway: for a list of SwissFEL-related research projects, see Appendix B.

Also important is the involvement of Swiss industry in the project; a well-attended SwissFEL Industry Information Day at PSI in 2009 demonstrated the active interest of Swiss companies. Finally, the SwissFEL will be an excellent training ground for young scientists, engineers and technicians. Experience has shown that these qualified persons readily find employment in technical professions within Switzerland.

The SwissFEL design

The SwissFEL design (see Fig. I1) is based on an electron accelerator, consisting of a high-brightness electron gun, a booster, three sections of linear accelerator (linac) and two bunch compressors (BC). Electrons are extracted at energies from 2.1 to 5.8 GeV and fed to two undulators, long arrays of alternately-poled permanent magnets, where intense, coherent X-ray pulses are generated for two X-ray beamlines, “Athos” and “Aramis”, operating in parallel. Important specifications of the SwissFEL are summarized in Table I2.

Photon energy (wavelength)	180 eV – 12.4 keV (7 – 0.1 nm) extendable to 50 eV – 15 keV (25 - 0.08 nm)
Peak X-ray power	10 GW
Soft X-rays (< 1.6 keV)	Optional circular polarization (for magnetic contrast) Transform-limited pulses (using seeding technology)
Hard X-rays (> 1.6 keV)	<20 fs pulse duration (in “low-charge” mode)
Synchronized pump sources	Visible, IR lasers Dedicated THz source
Pulse repetition rate	100 Hz, to 2 beamlines in simultaneous operation (extendable to 400 Hz)

Table I2. Important specifications of the SwissFEL facility.

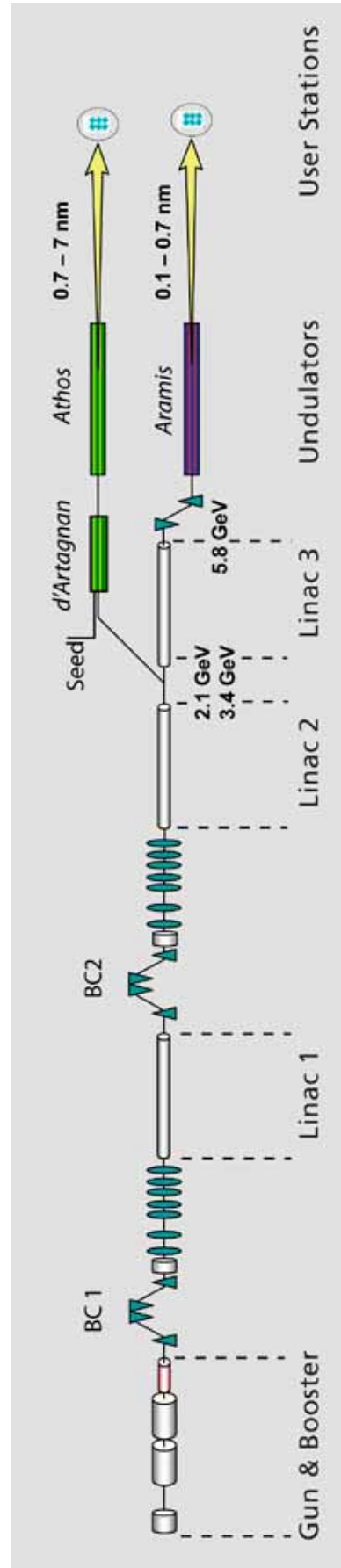


Fig. I1. A schematic of the proposed SwissFEL facility. “Seeding” of the Athos beamline is accomplished with a HHG seed source and the small “d’Artagnan” undulator.

The photon energy range of the SwissFEL, 180 eV – 12.4 keV (extendable to 50 eV – 15 keV), covers the wide range of scientific applications described in detail in Chapters I through V of the present report (see Fig. I2).

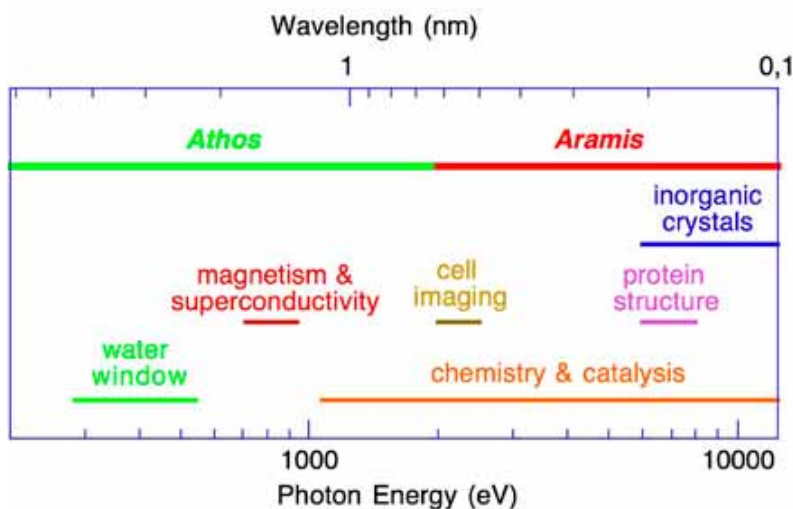


Fig. I2. The range of X-ray wavelengths (photon energies) produced by the Athos and Aramis beamlines of the SwissFEL covers a wide range of scientific investigations. In the “water window”, carbon and nitrogen compounds are visible to X-rays, while a water background is transparent.

The SwissFEL design includes possibilities for future enhancements. Among them are:

- An extension of the minimum photon energy of the Athos beamline to 50 eV (maximum photon wavelength to 25 nm) by using the seeding undulator d’Artagnan and the 2.1 GeV electron beam as a coherent radiation source. This would allow high-resolution spectroscopic measurements at the L-absorption edges of the elements Mg, Al, Si and P.
- An extension of the maximum photon energy of the Aramis beamline to 15 keV (minimum photon wavelength to 0.08 nm) by increasing the maximum electron energy from 5.8 to 6.5 GeV. This would allow novel experiments at the ultra-narrow (30 neV) Mössbauer resonance of ^{57}Fe , at 14.4 keV (e.g., see Chapter V).
- An increase in the repetition rate of the SwissFEL from 100 to 400 Hz, which is still compatible with detector readout and adjustments of the beamline and sample.
- The construction of one or two additional hard or soft X-ray beamlines, depending upon demand, and associated experimental areas.

Project organisation

The SwissFEL is presently defined as a “project” within PSI, with a direct connection to the PSI directorate (see Fig. I3).

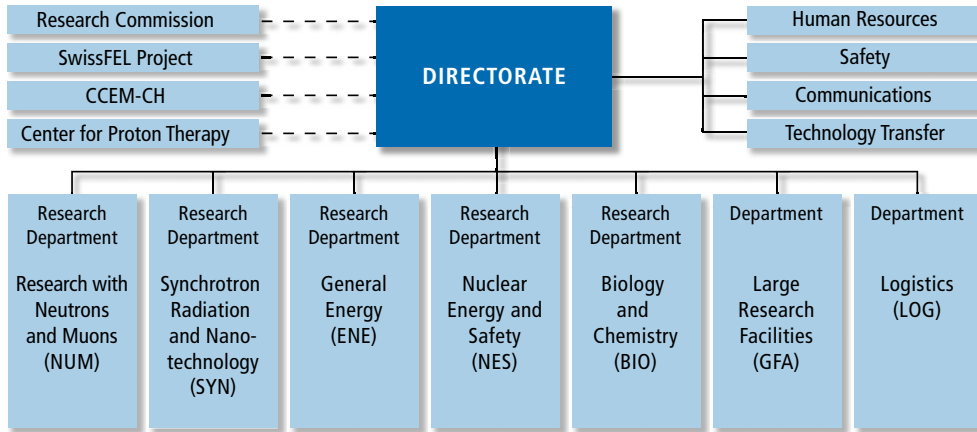


Fig. I3. The SwissFEL is officially a “project”, directly connected to the PSI directorate.

The organisation chart of the SwissFEL project is shown in Figure I4. There are two SwissFEL project leaders, Dr. Hans Braun, for the machine, and Dr. Rafael Abela, for photonic applications, who direct the activities of the “management unit”, comprising in addition the machine and photonics coordinators and a dedicated support group. A tight integration of the SwissFEL across the entire PSI is effected by the “coordination board”, which includes all of the PSI infrastructure and research department heads. In a flexible matrix configuration, expertise of the individual departments flows into the SwissFEL project as short- or long-term “workpackages”. The PSI directorate maintains contact with representatives of academia and governmental commissions via a “sounding board”, and it also receives regular reports from separate advisory committees for the accelerator and for science applications.

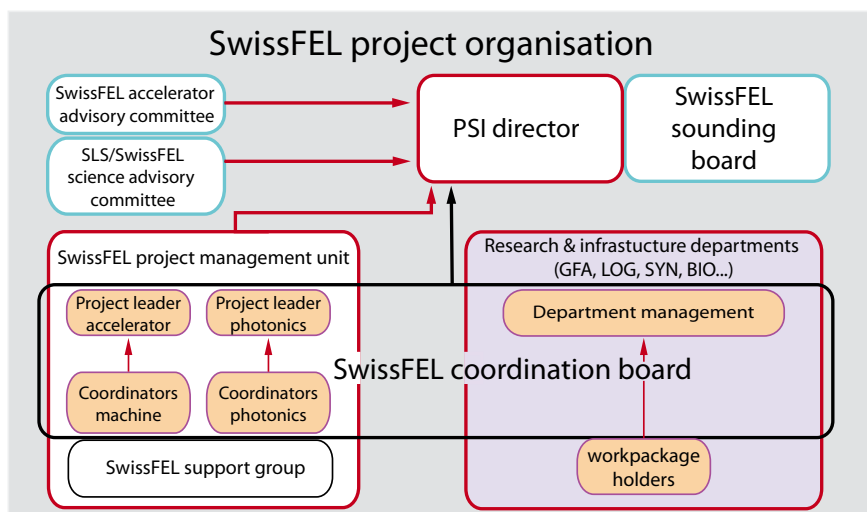


Fig. I4. The organizational diagram of the SwissFEL project, showing the close connections, via the coordination board, to the PSI infrastructure and research departments GFA, LOG, SYN, NUM, ENE, NES and BIO.

Schedule

The time schedule of the SwissFEL project is shown in Figure I5. Major milestones are:

- Presentation and evaluation by the ETH Board: February 2010
- Presentation to key institutions: 2010
- Implementation of the project in the “Forschungsbotschaft”: Spring 2010
- Evaluation of the Forschungsbotschaft by the Federal Parliament: 2011 Session

Assuming a positive parliamentary decision, the civil construction work and installation of the technical infrastructure will start in early 2012. It is foreseen to divide the construction into two phases, with completion of the electron accelerator and the hard X-ray Aramis beamline in 2016. This configuration of the SwissFEL will satisfy approximately 65 % of the scientific requirements discussed in the SwissFEL workshops and presented in Chapters I-V of this document. Construction of the soft X-ray Athos beamline would then begin early in 2017, with completion of the entire facility a year later. This two-phase construction schedule allows additional time for research and development of enhanced seeding technologies for the Athos beamline.

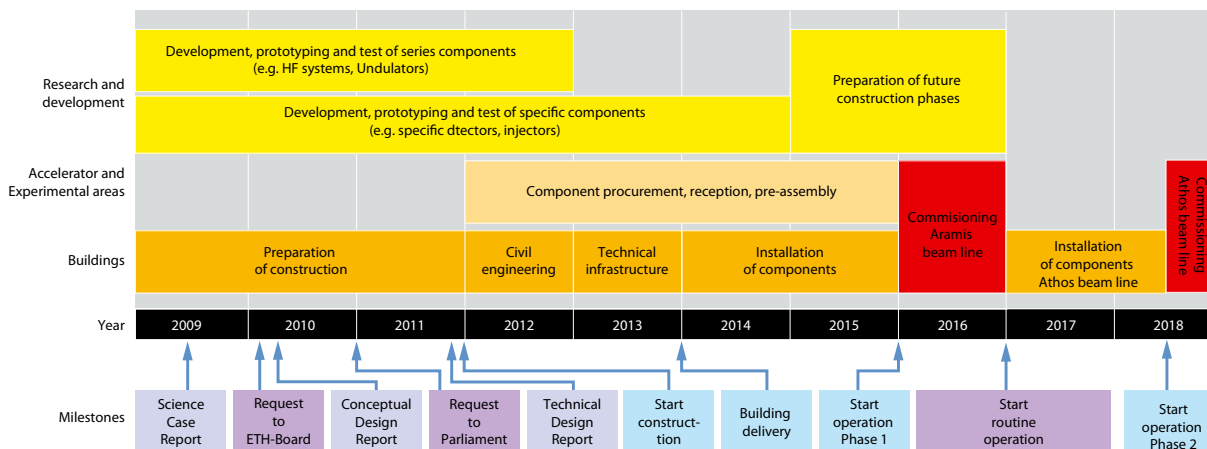


Fig. I5. Time schedule for the SwissFEL project.

Present and future X-ray sources

Light is the preferred tool for investigating matter. Consider visual inspection with the optical microscope, or the quantitative study of electronic properties with laser spectroscopy. Ultrashort laser pulses, lasting a few femtoseconds (10^{-15} s) allow spectroscopy to be performed as a function of time, making dynamic processes accessible to study.

The *atomic* structure of matter becomes visible when the wavelength of the light is reduced to the nanometer scale (10^{-9} m) – the X-ray regime. And X-rays bring the additional benefit of being wavelength-specific to the individual chemical elements.

The development of ever brighter X-ray sources, in particular, of successive generations of synchrotrons (see Fig. I.i1), has strongly influenced that of condensed matter science. Synchrotrons are based on circular electron accelerators and provide a brilliance which is 10^{12} times that of a laboratory device. Their principal achievement has been the almost routine atomic structure determination of large biomolecules in the crystalline state. The 3rd-generation Swiss Light Source (SLS) synchrotron is an intense, almost continuous, tunable source, which provides soft and hard X-rays to 17 experimental stations during 5000 hours per year.

Despite their unquestioned value in condensed matter science, synchrotrons cannot provide the ultrashort and ultra-intense pulses required to investigate fast processes; they produce radiation damage to the sample, which limits data quality, and their X-rays are incoherent, like the chaotic radiation from a light bulb. In contrast to the synchrotron, X-ray Free Electron Lasers, such as the SwissFEL, are based on *linear* electron accelerators. Tunable X-rays, both soft and hard, are generated in ultra-bright, ultrashort pulses and simultaneously delivered to typically 2 experimental stations. When tightly focused, a single X-ray pulse will locally destroy the sample, but not before the unperturbed scattering or spectroscopic signature is recorded. As is the case with all laser light, the SwissFEL radiation will be highly coherent. It can be seen from Fig. I.i1 that the increase in peak brilliance from the SLS to the SwissFEL (12 orders of magnitude) is the same as from the tube laboratory sources to the SLS!

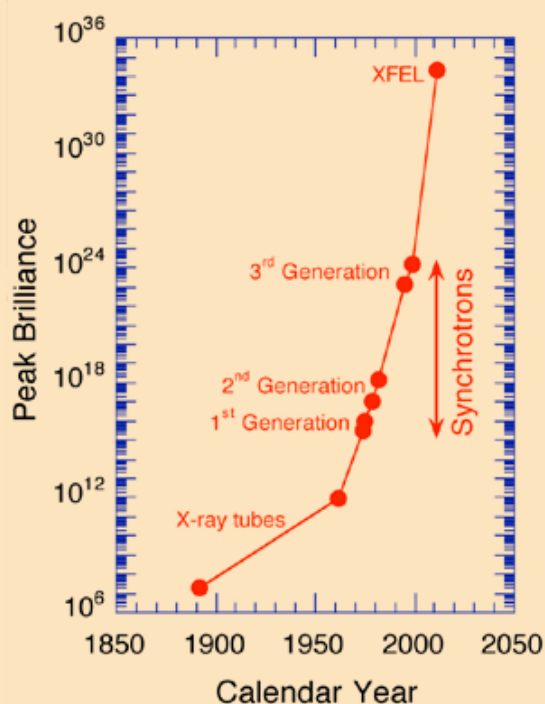


Fig. I.i1. History of the peak brilliance (in photons/s/mrad²/mm²/0.1% bw) of X-ray sources.

I. Ultrafast Magnetization Dynamics on the Nanoscale

Temporal spin behavior in magnetic systems at short length and time scales

- Time and length scales in magnetism
- Magnetically sensitive X-ray measurement techniques
- Ultrafast manipulation of the magnetization
- Instabilities in low-dimensional magnetism

Magnetism is responsible for one of the oldest inventions, the magnetic compass, and further applications have revolutionized our world, through, e.g., ferrite core memory to today's high-density data storage. In modern magnetic storage devices, of the order of 400 gigabits can be written per square inch at a rate of one bit per two nanoseconds. Faster reversal, on the sub-ps time scale, has been demonstrated, but its origins still remain to be investigated.

The fact that many fundamental magnetic processes take place on the nanometer length and picosecond time scales, and the high magnetic sensitivity of resonant, circularly-polarized X-rays, make the SwissFEL a versatile instrument for state-of-the-art research in magnetism. Of particular current interest are the ultrafast disappearance, creation and modification of magnetic order and the novel quantum effects which arise in two-, one- and zero-dimensional systems. The Swiss-FEL, with coherent, high-brightness, circularly-polarized X-rays at energies resonant with the 3d-transition metal ions, corresponding to nm wavelengths, is capable of single-shot lensless imaging of nanometer-scale magnetic structures. Furthermore, the combination of high-energy, half-cycle THz pump pulses and the synchronized, sub-picosecond SwissFEL probe pulses will permit the investigation in real time of ultrafast magnetic interactions.

Time and length scales in magnetism

The rich variety of characteristic magnetic lengths and times accessible by the SwissFEL is summarized in Figure I.1 and Tables I.1,2 [1,2]. Time-scales τ are determined by the interaction energies E via the Heisenberg relation $\tau \approx 1/\nu = h/E$, where Planck's constant $h = 4.14 \times 10^{-15}$ eV s. For example, if the reorientation of a magnetic moment requires expenditure of an energy E , it will relax to its equilibrium orientation in a time of order $\tau = h/E$. Reference is made in the Tables to the following material-dependent constants: J – magnetic exchange interaction, K – crystal-line anisotropy, M_s – saturation magnetization and k_F – electron Fermi momentum.

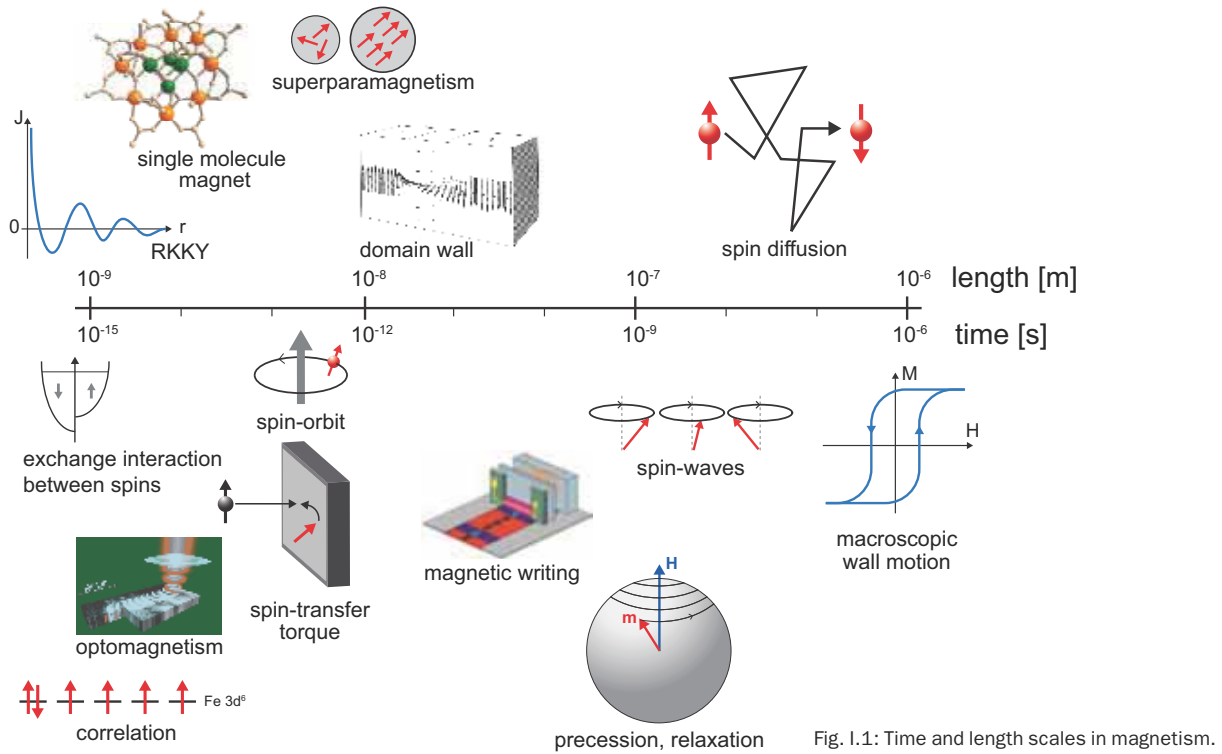


Fig. I.1: Time and length scales in magnetism.

Distance over which a diffusing electron maintains its polarization	$\sim 10 \times$ mean free path
Bloch domain wall width	$\sim 1 \mu\text{m}$
Minimum size of a magnetic particle before superparamagnetic fluctuations destroy its ferromagnetism	$\sim (J/K)^{1/2} \sim 20 \text{ nm}$
The exchange length determines the diameter of a vortex core	$\sim (J/2\pi M_s^2)^{1/2} \sim 1 \text{ nm}$
Wavelength of the RKKY spin-density oscillations of the conduction electrons near a magnetic ion	$\sim \pi/k_F \sim 0.2 \text{ nm}$

Table I.1: Magnetic length scales

Atomic moment reversal due to field- or current-induced domain wall motion, with a velocity of ~ 100 m/s	$d_{\text{wall}}/v_{\text{wall}} \sim 200 \text{ ps}$
Magnetization precession and damping, according to the LLG-equation (see Infobox)	$\sim 50 \text{ ps}$
Spin-orbit interaction between the electron spin and its orbital motion	1–100 meV $\rightarrow \tau \sim 50\text{--}5000 \text{ fs}$
Jahn-Teller interaction, which stabilizes an elastic distortion to avoid a degenerate electronic ground-state	$\sim 50 \text{ meV} \rightarrow \tau \sim 100 \text{ fs}$
Spin-wave energy, at intermediate wave-vector	1–1000 meV, $\rightarrow \tau \sim 5\text{--}5000 \text{ fs}$
Electrostatic crystal-field interaction of oriented 3d-orbitals with neighboring ions	$\sim 1 \text{ eV} \rightarrow \tau \sim 5 \text{ fs}$
Inter-electronic exchange energy J arising from the Pauli principle	$\sim 5 \text{ eV} \rightarrow \tau \sim 1 \text{ fs}$
Correlation energy, responsible within an atom for enforcing Hund's rules	$\sim 5 \text{ eV} \rightarrow \tau \sim 1 \text{ fs}$

Table I.2: Magnetic time scales

XMCD: A simple example

This simple explanation of X-ray Magnetic Circular Dichroism is due to Gallani [22]. Consider an 8-electron atom, with the electron configuration $(1s^2 2s^2 2p^4)$ in an applied magnetic field \vec{B} . Due to the Zeeman splitting of the 2p states, the $|l=1, m=1\rangle$ state is unoccupied. Using circularly-polarized X-rays, we excite the $1s \rightarrow 2p$ transition (see Fig. I.i1). The dipole selection rule requires that $\Delta m = \pm 1$, and the conservation of angular momentum implies that for right- (RCP) and left-circular (LCP) polarization, $\Delta m = +1$ and -1 , respectively. The RCP transition, to the empty $|1, 1\rangle$ state, results in strong absorption, while, because the $|1, -1\rangle$ state is occupied, LCP X-rays are not absorbed. In this way, angular momentum conservation laws and selection rules lead to a circular dichroic, polarization-dependent absorption.

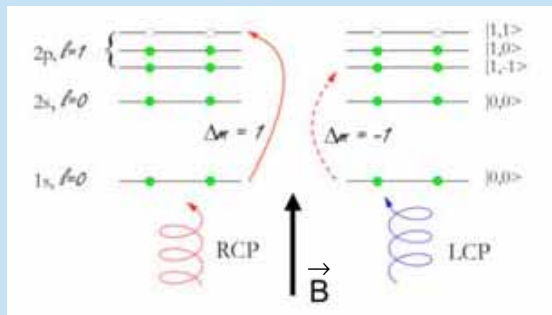


Fig. I.i1. A simple, 8-electron atom example of X-ray circular dichroism.

Magnetically sensitive X-ray measurement techniques

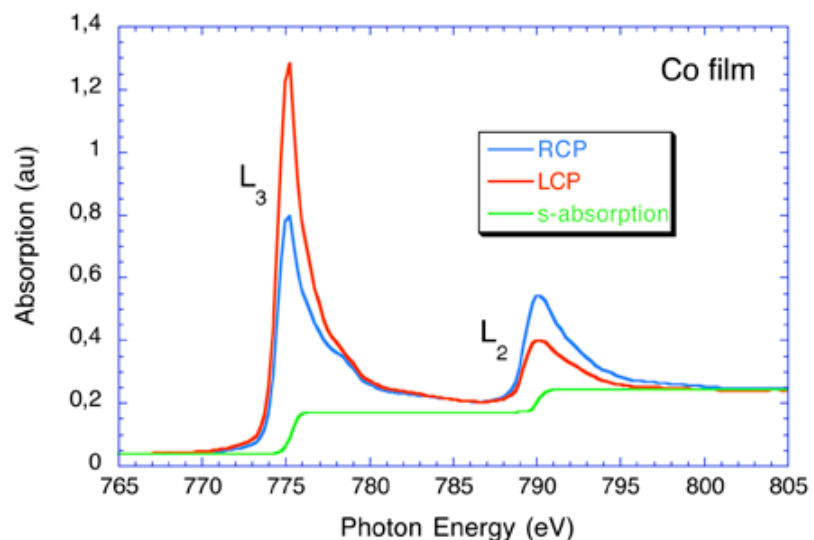
X-ray Magnetic Circular Dichroism (XMCD)

XMCD is the X-ray equivalent of the magneto-optical Kerr effect; the quantity measured is the dependence of the absorption on X-ray helicity close to a magnetically-sensitive resonant absorption edge. An example is the spin-orbit-split $2p \rightarrow 3d$ transitions (L_2 and L_3 edges) of the transition-metal ions. The origin of X-ray magnetic dichroism is explained for a simple example in the Infobox. In contrast to the magneto-optical Kerr effect, XMCD involves a localized initial state, and hence provides chemical and orbital selectivity. If many-body effects can be neglected, XMCD sum-rules can yield both the orbital and spin magnetic moments μ_L, μ_S , of the resonant ion (see Fig. I.2). Note that the XMCD contrast is a strong effect: at resonance, the dichroic X-ray interaction per atom can exceed that of 40 electrons! Application of the XMCD technique at the SwissFEL will profit from flexible wavelength tuning, and ultrafast pump-probe measurements will follow the individual time evolutions of the spin and orbital moments in the sample.

Magnetic-contrast holography

With the strong XMCD contrast of resonant magnetic scattering and the high coherence of the SwissFEL, it is possible to perform time-resolved lensless magnetic imaging (see also Chapter III). An elegant X-ray holographic method for thin magnetic films has been developed by Eisebitt et al. [4] (Fig. I.3). Since the experiment is performed at a synchrotron, spatial-filtering is required to produce transverse coherence, and a monochromator

Fig. I.2. An XMCD measurement at the L -edges of cobalt for right and left circularly polarized light [3]. The dichroic signal A is defined as the energy-integrated difference between the RCP and LCP absorption (minus the magnetically-insensitive s -band absorption). The XMCD sum-rule then states that $\mu_S = \mu_B(A_{L3} - 2 A_{L2})/A_{iso}$ and $\mu_L = \mu_B(A_{L3} + A_{L2})/A_{iso}$. XMCD measurements at the SwissFEL will allow one to follow the ultrafast time-dependence of spin and orbital moments, for example, in the study of optomagnetism (see Infobox).



is used to provide sufficient longitudinal coherence. The magnetic thin-film sample, which spans a hole in the sample support, transmits the resonant, circularly-polarized object beam, and close to the sample is a smaller hole, through which an undisturbed reference beam is transmitted. The two beams interfere on their way to the CCD area detector, where they produce a holographic image, and a simple Fourier transform is sufficient to reconstruct a real-space image of the sample.

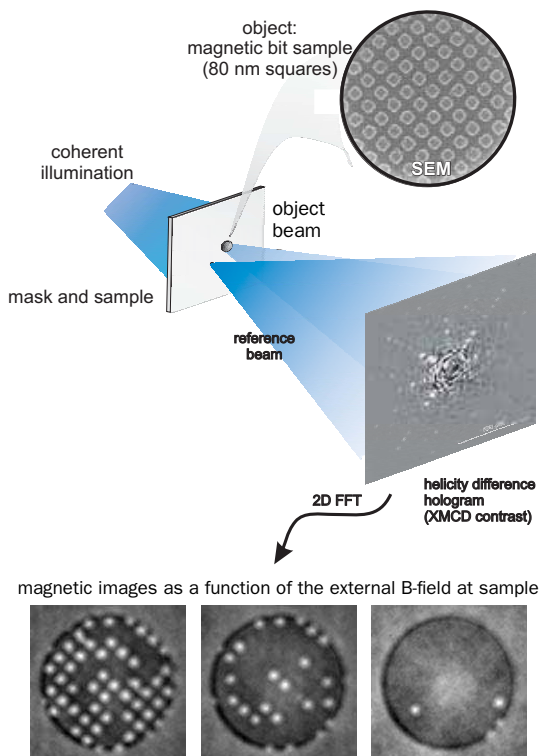


Fig. I.3. The magnetic holography method of Eisebitt et al. [4,5]. As described in the text, synchrotron light, filtered to introduce coherence, passes through either the sample or the reference pin-hole and interferes to produce a holographic image. This hologram is Fourier-transformed to reconstruct the real-space object, in this case a collection of magnetic squares.

The spatial resolution of the technique is presently limited by the diameter of the reference beam aperture (100 nm). But with enhanced data analysis techniques, it should be possible to approach the diffraction limit given by the soft X-ray wavelength (1.6 nm at 775 eV). Due to the limited coherent flux currently available from 3rd generation synchrotrons, collection of a single image requires several minutes of exposure time. With the high peak intensity of the SwissFEL, it will be possible to collect a holographic image in a single shot. Considering that the sample is a thin membrane, this may be a destructive experiment, requiring a fresh sample for each successive measurement. One could then envisage re-

peated, single-shot pump-probe investigations, on similarly-prepared samples, of sub-ps magnetic behavior triggered by laser or THz pump pulses. Although fine sample-dependent details may vary from shot to shot, the basic switching process remains the same.

Spin-polarized time-of-flight (TOF) photoelectron spectroscopy

A direct measurement of the electron polarization can be performed by using photoemission, where electrons are ejected from the sample surface, and where spin analysis is performed, e.g., via Mott scattering. For sufficiently high photon energies, band-structure-dependent final state effects can be neglected. The photoelectric cross-sections for the magnetic sub-shells of magnetic elements peak in the photon energy range 30–100 eV, which will be accessible by the SwissFEL. Spin-analysis using Mott detectors is highly inefficient, and laser-induced magnetic phenomena can be extremely fast (sub-ps). Thus the high peak intensity and the short pulse duration of the SwissFEL make it very attractive for such measurements. Furthermore, with a pulsed photon source, a simple electron time-of-flight (TOF) detector can be used to provide energy resolution (see Fig. I.4). One concern is that the high peak intensity of the SwissFEL will briefly produce a high density of low-energy photoelectrons near the sample surface, causing space-charge effects, which may distort the photoelectron energy distribution. However, since the interaction is to a good approximation electrostatic, the electron spin-polarization will not be affected.

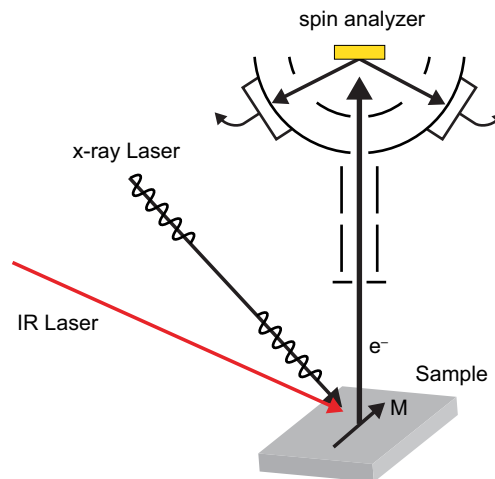


Fig. I.4. Schematic plan of a spin-polarized time-of-flight (TOF) photoelectron spectrometer. Energy resolution is provided by TOF detection. Because the Mott-scattering spin analyzer can simultaneously detect both spin orientations, true single-shot operation is possible.

The three-temperature model of magnetism

The three-temperature model (Fig. I.i2) for magnetization dynamics [10] has been invoked to help explain the sub-ps demagnetization observed by Beaurepaire et al. [8]. The model assumes that the electron motion (el), the electron spins (mag) and lattice phonons (lat) represent three mutually-interacting thermal reservoirs. The internal equilibration of the reservoirs occurs at the plasma frequency (el), the spin-wave frequency (mag) and the phonon scattering rate (lat). Furthermore, the reservoirs interact with one another via the electron-phonon interaction (el-lat), the spin-lattice relaxation rate (mag-lat) and the spin-orbit interaction (el-mag).

Note that the 3-temperature model is purely thermodynamic in nature and hence fails to account for the wavelength of the excitation. With a tunable source such as the SwissFEL, the dependence of bath temperature on wavelength can be investigated [12].

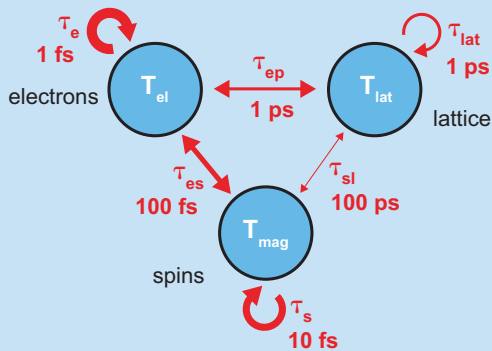


Fig. I.i2. A schematic diagram of the three-temperature model, showing the time constants for equilibration and interaction of the reservoirs. Fundamental criticism of the model may be clarified with ultrafast pump-probe experiments at the SwissFEL.

Ultrafast manipulation of the magnetization

Microwaves and terahertz pulses

Dynamic magnetic phenomena can be initiated by a short magnetic field pulse. Using a laser-triggered strip-line, a thin-film sample can experience a 0.01 T magnetic pulse with a rise-time of approximately 100 ps, corresponding to an excitation bandwidth of 10 GHz. In 1999, using pulses of relativistic electrons from the SLAC accelerator directed into the sample, Ch. Back et al. [6] produced multi-tesla fields lasting a few ps, which were large enough to initiate a full magnetization reversal within the plane (see Fig. I.5). Although during the field pulse the magnetization only rotates by approximately 10 degrees (see the Infobox on the Landau-Lifshitz-Gilbert equation of motion), as soon as it tips out of the sample plane, M begins to feel the large shape anisotropy from the proximity of the film surfaces.

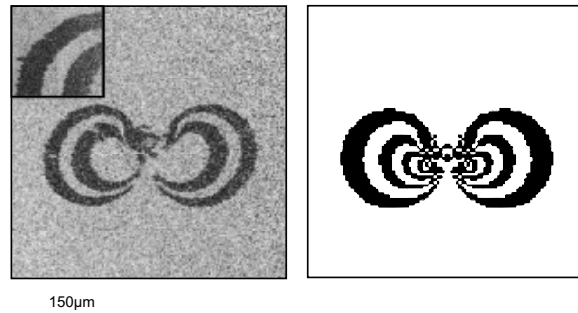


Fig. I.5. Magnetization reversal pattern observed in a thin Co film (with the in-plane easy magnetization direction horizontal), caused by irradiation with a 4.4 ps relativistic electron pulse [6]. The resulting magnetic field at the lowest field reversal point, 110 μm from the beam center, was 0.23 T. The left-hand frame is the pattern measured with spin-polarized electron microscopy, and the right-hand frame is a simulation using the LLG-equation, including the effect of shape anisotropy.

The design of the SwissFEL foresees a separate source of terahertz (THz) radiation, capable of delivering high-energy electromagnetic pump pulses which are synchronized with the X-ray probe pulses from the SwissFEL. The intensity (power/area) delivered by an electromagnetic pulse is $I = B_0^2 c / 2\mu_0$, implying that a 100 μJ , half-cycle THz pulse (0.5 ps) focused to 1 mm^2 will produce a peak magnetic field $B_0 = 1.3$ T, i.e., more than 100 times that of a strip-line, and with a THz excitation bandwidth. This offers the possibility of probing the ultimate limit of magnetization dynamics, which is at least a factor 1000 faster than conventional field-induced spin switching.

A further possibility for rapidly perturbing the magnetic moments in a dynamic XMCD experiment is X-ray detected ferromagnetic resonance, using continuous-wave or pulsed microwave (GHz) radiation [7]. When resonant with the Zeeman-split energy levels of the magnetic ions, the microwaves excite damped magnetic precession, the details of which are sensitive to dynamic couplings and magnetization relaxation. If several magnetic species are simultaneously present in the sample, the elemental selectivity of XMCD allows the dynamics of each to be studied individually. The high peak brightness and excellent time resolution of the SwissFEL would be very beneficial for this technique, avoiding the present restriction to samples with very low damping.

Laser-induced phenomena

In 1996, Beaupaire et al. published a very remarkable observation [8]: a Ni film exposed to an intense 60 fs pulse from an optical laser becomes demagnetized in less than a picosecond. Using the magneto-optical Kerr effect as probe, an ultrafast decrease is observed in the magnetization, followed by a slower recovery (see Fig. I.6). This observation, together with later measurements using other methods of detection, raised the fundamental question, as yet unanswered, of where the spin angular momentum of the electrons goes and how it can be transferred so quickly.

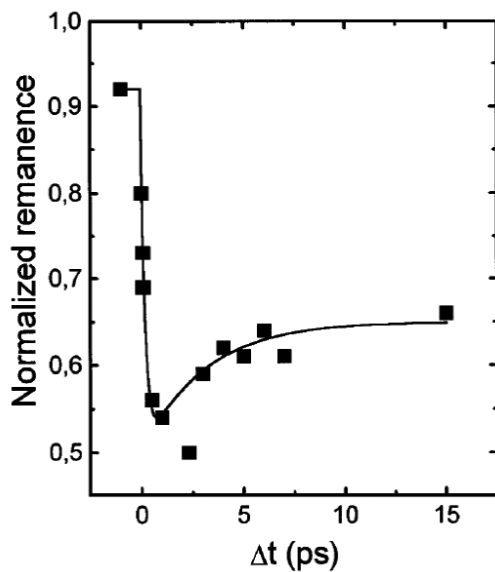


Fig. I.6. Sub-picosecond demagnetization of a Ni film following an optical laser pulse, observed with the magneto-optical Kerr effect [8]. This observation stimulated much speculation on the as yet unanswered question of how angular momentum can be transferred so efficiently from the spin system to the lattice.

The three-temperature model, which invokes separate temperatures to characterize the electron kinetic energy (T_{el}), the electronic spin order (T_{mag}) and the lattice vibrations (T_{lat}) (see Infobox), has been used to describe the demagnetization process. It is assumed that the laser pump pulse initially delivers energy to the electron reservoir T_{el} and that each reservoir individually remains in equilibrium. But due to their relatively weak intercoupling, the three temperatures may differ significantly, giving rise to strong non-equilibrium effects which have not yet been investigated.

Microscopic models have difficulty in explaining how the laser excitation of the conduction electrons can cause such a rapid transfer of angular momentum away from the spin system or indeed what is its destination. Among the proposals put forward are: hiding the angular momentum in electronic orbits, or transferring it to the lattice via special hot-spots in the electron band structure with exceptional spin-orbit coupling or via an enhancement of the spin-orbit interaction by the presence of phonons [9].

A *phenomenological* treatment of the entire de- and remagnetization process using an atomic analog of the LLG equations, with the magnetization M replaced by the atomic spin S , has been published by Kazantseva et al. [10]. These authors introduced an effective field acting on the atomic moments which includes a stochastic, fluctuating component, which they then related to the LLG damping constant α using the fluctuation-dissipation theorem (see Infobox).

From their atomistic numerical simulations (see Fig. I.7), Kazantseva et al. [10] find that the magnetization can be non-zero in spite of a spin temperature T_{mag} which exceeds the Curie temperature of Ni ($T_C = 631$ K), leading them to question the concept of equilibration of the spin system and hence of a spin temperature. The authors find that the coupling constant which governs the post-pulse recovery of the magnetization is the same as that responsible for the ultrafast demagnetization. They explain the much slower recovery, and the fact that the recovery is slower for a more complete demagnetization, with the concept of a magnetic entropic barrier (see Chapter IV) – i.e., if the magnetization vanishes, it takes time for the system to reorganize itself.

In addition to this, now classic, example of ultrafast demagnetization, some systems show the phenomena of ultrafast *magnetization*. For example, intermetallic FeRh undergoes a transition at 360 K from a low-temperature anti-ferromagnetic phase to a high-temperature ferromagnetic phase, which is accompanied by an isotropic lattice expansion. This transition can be induced

The Landau-Lifshitz Gilbert Equation

To describe the time-evolution of the magnetization subjected to a magnetic field H , one uses the Landau-Lifshitz Gilbert equation, which has the form:

$$\frac{d\vec{M}}{dt} = \gamma\mu_0\vec{M} \times \vec{H} + \frac{\gamma\mu_0\alpha}{M_s}\vec{M} \times (\vec{M} \times \vec{H})$$

where $|\vec{M}| = M_s$. $\gamma = -g_{Landé}\mu_B/\hbar$ is the gyromagnetic ratio ($= -1.76 \times 10^{11} \text{ rad s}^{-1} \text{ T}^{-1}$, for $g=2$), and α is the damping constant. The resulting motion of the magnetization is that of a damped precession about the effective field \vec{H} (see Fig. I.i3). The first term causes a precession with angular frequency $\omega = \gamma H$, and the second term exponentially damps the precession at the rate $\alpha\omega$. In a one-tesla field, the precession period is 36 ps, and the damping time $1/\alpha\omega$ may be a factor 100 longer.

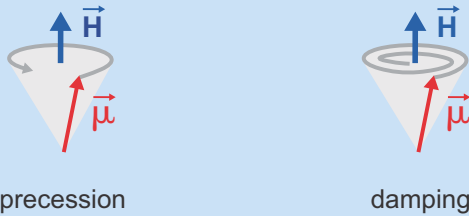
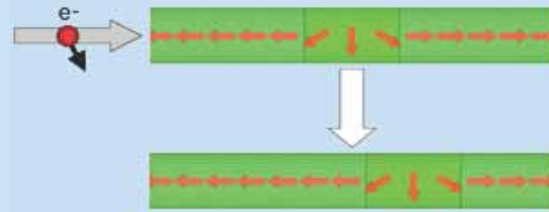


Fig. I.i3. The Landau-Lifshitz Gilbert equation of motion for the magnetization in an effective field H , which may include external and internal magnetic interactions.

Spin-torque: ultrafast switching by spin currents



Beyond the conventional switching by applied external fields, magnetization manipulation can also be achieved by using spin transfer from spin-polarized currents that flow in a magnetic structure. This leads to ultra-fast reversal of nano-pillar elements as well as current-induced domain wall motion. Here the magnetization dynamic timescales are not limited by the gyromagnetic ratio and can be potentially much faster.

Including a spin-polarized current (\vec{u} is proportional to the current density and the spin-polarization of the current), the extended Landau-Lifshitz Gilbert equation now reads:

$$\frac{d\vec{M}}{dt} = \gamma\mu_0\vec{M} \times \vec{H} + \frac{\alpha}{M_s}\vec{M} \times \frac{d\vec{M}}{dt} - (\vec{u} \cdot \vec{\nabla}) \frac{\vec{M}}{M_s} + \beta \frac{\vec{M}}{M_s} \times \left[(\vec{u} \cdot \vec{\nabla}) \frac{\vec{M}}{M_s} \right]$$

with the last two terms accounting for the adiabatic and non-adiabatic spin-torque. The strength of the effect is given by u and the non-adiabaticity parameter β .

Spin currents can be generated by spin-injection, spin pumping and, on a femtosecond timescale, by exciting spin-polarized charge carriers with a fs laser [23]. Furthermore, heating the electron system with a short laser pulse will generate large temperature gradients, and the resulting spin currents and spin-torque-induced ultra-fast magnetization dynamics can be ideally probed using the SwissFEL.

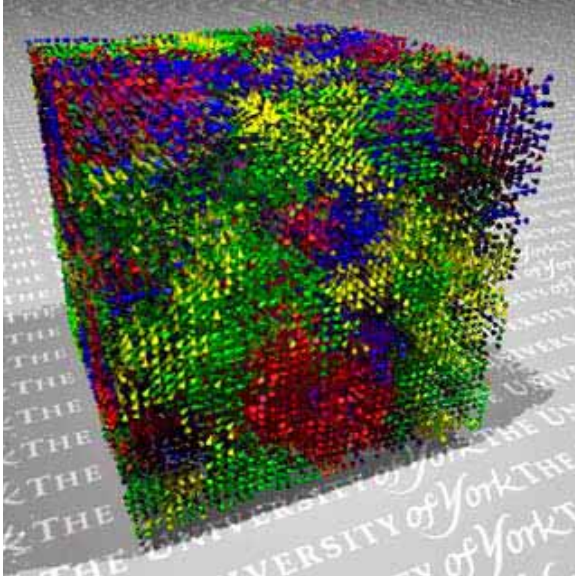


Fig. I.7. A frame from a phenomenological, atomistic simulation using the LLG and Langevin dynamics approaches [10]. After rapid demagnetization, the spin system must choose between many possible magnetized states and thus is confronted with an entropic barrier.

by an ultrashort laser pulse [11]. Preliminary results using 50 ps X-ray probe pulses from a synchrotron suggest that the establishment of ferromagnetic order precedes the increase in lattice constant, possibly answering the chicken-or-egg question as to which is the cause and which is the effect.

Finally, in experiments with a direct connection to magnetic data storage, it has been found that ultrafast pulses of circularly-polarized laser light can, via the inverse Faraday effect, even reverse the direction of magnetization in a sample (see the optomagnetism Infobox). The above examples of the ultrafast manipulation of magnetization with optical pulses point to a rich variety of possibilities for SwissFEL pump-probe investigations for both fundamental science and practical applications. Ultrafast perturbation of a magnetic spin system is also possible using the spin-transfer torque phenomenon, which is the basis for spintronic schemes of data processing (see Infobox) [12].

Langevin dynamics and the fluctuation-dissipation theorem

In their numerical treatment of ultrafast magnetization recovery after an optical pulse, Kazantseva et al. [10] used the formalism of Langevin dynamics to relate the amplitude of a fluctuating magnetic field experienced by a local moment to the strength of the viscous damping it undergoes. The general relationship between fluctuations and damping is expressed in the fluctuation-dissipation theorem (FDT), which we derive here for the simple case of the one-dimensional Brownian motion of a particle [24].

Consider a particle with mass M and velocity $v(t)$ which interacts with the local environment via both a viscous force, characterized by the mobility μ , and a randomly fluctuating force $f(t)$. The resulting (Langevin) equation of motion is:

$$M\dot{v}(t) + \frac{1}{\mu}v(t) = f(t)$$

or, with the definitions $\gamma = 1/M\mu$ and $A(t) = f(t)/\mu$:

$$\dot{v}(t) + \gamma v(t) = A(t)$$

This equation has the steady-state solution (for $\gamma t \gg 1$):

$$v(t) = \int_0^t e^{\gamma(u-t)} A(u) du$$

We require that $A(t)$ have a zero mean value ($\langle A(t) \rangle = 0$), a vanishing autocorrelation time and a time-independent variance ($\langle A(t_1)A(t_2) \rangle = A^2 \delta(t_1 - t_2)$, $A = \text{const.}$).

The (steady-state) variance of the velocity is then:

$$\begin{aligned} \langle v^2(t) \rangle &= e^{-2\gamma t} \int_0^t du \int_0^t e^{\gamma(u+w)} \langle A(u)A(w) \rangle \\ &= A^2 e^{-2\gamma t} \int_0^t du e^{2\gamma u} = \frac{A^2}{2\gamma} (1 - e^{-2\gamma t}) \rightarrow \frac{A^2}{2\gamma} \end{aligned}$$

Making use of the equipartition theorem:

$$\frac{1}{2} M \langle v^2 \rangle = \frac{kT}{2}$$

we find the following condition:

$$\gamma = \frac{M}{2kT} A^2$$

or:

$$\frac{1}{\mu} = \frac{1}{2kT} \int_{-\infty}^{\infty} \langle f(0)f(t) \rangle dt$$

This relation between the viscous and random forces is a special case of the more general FDT.

Optomagnetism

A large effort is presently being made to use intense, fs pulses of circularly-polarized light to write magnetic information in thin film media. The goal is to explore the limits of high-speed magnetic writing. The production of an effective magnetic field by a circularly-polarized light wave is called the inverse Faraday effect. This is the basis of optomagnetism, i.e. the manipulation of the magnetization by laser light.

A circularly-polarized light wave can produce an effective magnetic field as follows [25]:

Beginning from the expression for the energy density of a light wave,

$$W = \epsilon \epsilon_0 E(\omega) E^*(\omega),$$

one can compute an effective magnetic field as

$$\mu_0 H_{\text{eff}} = \frac{\partial W}{\partial M} = \epsilon_0 E(\omega) E^*(\omega) \frac{\partial \epsilon}{\partial M}$$

An expression due to Onsager relates the off-diagonal elements of the dielectric tensor and the magnetization:

$$\epsilon_{ij} = \alpha M + \beta M^3 + \dots$$

The resulting effective field (see Fig. I.i4):

$$\mu_0 H_{\text{eff}} = \alpha \epsilon_0 E(\omega) E^*(\omega)$$

can be as large as 1 T.

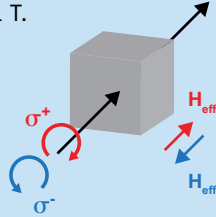


Fig. I.i4. Circularly polarized light can, in an optomagnetic medium, create a large effective magnetic field.

A demonstration of sub-ps magnetic writing has been made by Stanciu et al. [26] using 40 fs pulses in GdFeCo (see Fig. I.i5), but fundamental questions remain regarding how the ultrafast transfer of angular momentum occurs.



Fig. I.i5. Magnetic microstructures written into GdFeCo with right- and left- circularly polarized light [26]. The SwissFEL will allow the investigation of this process on fs and nm scales, which is important both for a microscopic understanding and for potential data storage applications.

Instabilities in low-dimensional magnetism

In the previous Section, measurements and simulations were discussed of ultrafast magnetization phenomena in three dimensions; here possibilities are considered for using the SwissFEL to investigate the quantum-fluctuating behavior of low-dimensional magnetic systems [13].

In many magnetic insulators, magnetic moments interact through an exchange of electrons between neighboring sites. Such exchange interactions are short-ranged. If these interactions are isotropic, such systems can be described by the well-known Heisenberg Hamiltonian, which is given by:

$$H_{\text{Heisenberg}} = -J \sum_{\langle ij \rangle} \vec{S}_i \cdot \vec{S}_j$$

where J is the exchange energy, and the summation is over nearest-neighbor spins; If J is positive, the spins \vec{S}_i and \vec{S}_j tend to align ferromagnetically. For an ordered magnetic phase, the temperature-dependent change in the saturation magnetization can be calculated [14] in this model as $M_s(0) - M_s(T) \propto N_{\text{sw}}(T)$, where

$$N_{\text{sw}}(T) \propto \int \frac{k^{d-1}}{\exp[\epsilon(k)/k_B T] - 1} dk$$

is the density of spin-waves excited at the temperature T . For $d=3$ dimensions, this integral is proportional to $T^{3/2}$, giving the well-known Bloch 3/2-law.

For dimensions lower than $d=3$, the expression for $N_{\text{sw}}(T)$ diverges, implying that fluctuations will prevent the occurrence of long-range magnetic order. This is a fundamental result, which has been rigorously proven by Mermin and Wagner [15], and which means that many types of magnetic systems do not order at any finite temperature.

Some systems are disordered even at *zero* temperature, where thermal fluctuations are absent, due to the presence of quantum fluctuations in the ground state. This can happen if a static arrangement of magnetic moments is not an eigenstate of the Hamiltonian, causing quantum fluctuations to generate a new type of ground state. These disordered systems form ferromagnetically or antiferromagnetically-coupled spin liquids, and their quantum fluctuations, as described by the intermediate scattering function $S(Q,t)$ (see chapter V), represent a particularly rich field of investigation for the SwissFEL.

Two-dimensional case ($d=2$)

As an example of the dynamics of a 2d-magnetic structure, consider the case of an infinite in-plane anisotropy ($S_z=0$): the so-called xy -model: $H_{xy} = -J \sum_{\langle ij \rangle} (S_i^x S_j^x + S_i^y S_j^y)$

As for the 2d-Heisenberg model, there is no magnetic order at finite temperature in the xy -model. However, it is found that spin correlations cause the formation at low temperature of a disordered array of magnetic vortices, with radii of order R . The cost in exchange energy incurred by the formation of such a vortex is $\pi J \ln(R/a)$, where a is the lattice constant, and the gain in entropy represented by the varying position of the vortex center is $2k_B \ln(R/a)$. Hence the free energy $F = \ln(R/a)(\pi J - 2k_B T)$ becomes negative below the Kosterlitz-Thouless transition, at the temperature $T_{KT} = \pi J / 2k_B$, which separates a non-vortex from a vortex phase. At low temperatures, the $S=1/2$ layered perovskite ferromagnet K_2CuF_4 is approximately described by the xy -model, going through a Kosterlitz-Thouless transition at 5.5 K.

A further example of (quasi) 2d-magnetic dynamics is that of vortex core reversal in thin magnetic nanostructures (see Infobox).

One-dimensional case ($d=1$)

Magnetism in one dimension in the zero-temperature limit is particularly interesting, because it arises from quantum fluctuations. Consider first the isotropic $J>0$ Heisenberg model for a one-dimensional chain of N spins $S=1/2$, with periodic boundary conditions. The (ferromagnetic) ground state can be represented as $|\Psi_0\rangle = |\uparrow\uparrow\uparrow\dots\uparrow\rangle$. In the Bethe Ansatz, the excited states of the system are built up as a superposition of states with discrete numbers of flipped spins. If we confine ourselves to single-spin ($r=1$) excitations:

$$|n\rangle = |\uparrow\uparrow\uparrow\dots\uparrow\downarrow\uparrow\dots\rangle$$

(here the n^{th} spin has been reversed), we can write the excited state as

$$|\Psi_1\rangle = \sum_{n=1}^N a(n) |n\rangle$$

It is then a straightforward exercise to compute from the Schrödinger equation (for convenience, written in terms of the raising and lowering operators S_{\pm}) the excited-state energy E_1 , and one finds, for large N , that excitations exist with arbitrarily small excitation energies $E_1 - E_0$; i.e., the excitation spectrum is *gapless*. Higher level excitations, involving multiple spin flips $r = 2, 3, 4, \dots$, become increasingly cumbersome to handle, but the *gapless* spectrum is retained (Figure 1.8a shows the analogous result for the 1d-*antiferromagnetic* spin $1/2$ chain [16]).

Magnetic vortex core switching

The magnetic vortex is a very stable, naturally-forming magnetic configuration occurring in thin soft-magnetic nanostructures. Due to shape anisotropy, the magnetic moments in such thin-film elements lie in the film plane. The vortex configuration is characterized by the circulation of the in-plane magnetic structure around a very stable core of only a few tens of nanometers in diameter, of the order of the exchange length. A particular feature of this structure is the core of the vortex, which is perpendicularly magnetized relative to the sample plane. This results in two states: “up” or “down”. Their small size and perfect stability make vortex cores promising candidates for magnetic data storage.

A study by Hertel et al. [27] based on micromagnetic simulations (LLG equation) has shown that, strikingly, the core can dynamically be switched between “up” and “down” within only a few tens of picoseconds by means of an external field. Figure 1.i6 below simulates the vortex core switching in a 20 nm thick Permalloy disk of 200 nm diameter after the application of a 60 ps field pulse, with a peak value of 80 mT. Using field pulses as short as 5 ps, the authors show that the core reversal unfolds first through the production of a new vortex with an oppositely oriented core, followed by the annihilation of the original vortex with a transient antivortex structure. To date, no experimental method can achieve the required temporal (a few tens of ps) and spatial (a few tens of nm) resolution to investigate this switching process. The combination of the high-energy THz pump source and circularly-polarized SwissFEL probe pulses will allow such studies.

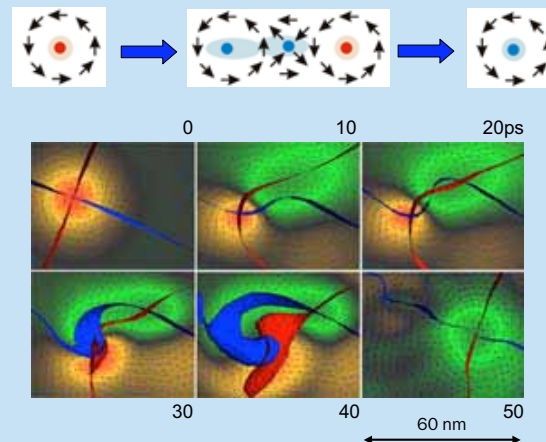


Fig. 1.i6. Numerical simulation [27] of the proposed switching process of a magnetic vortex core. The SwissFEL will provide the spatial and temporal resolution required to visualize this process.

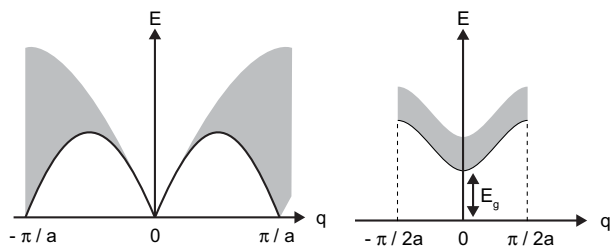


Fig. 1.8: a) The spin-wave dispersion relation for a 1d $S=1/2$ antiferromagnetic chain [16]. The shaded region corresponds to two-magnon excitations. b) The dispersion relation for a 1d Peierls spin $1/2$ chain [13], showing the opening of an energy gap E_g . Note that the Brillouin zone is reduced by half.

One of the simplest ways for a material to avoid magnetic order and develop macroscopic quantum correlations is through the creation of an energy gap E_g in the excitation spectrum. Since E_g is of the order of the exchange interaction, the gap introduces a time-scale for fluctuations which is typically on the order of femtoseconds. One such phenomenon is the *spin* Peierls effect. This is related to the better-known charge Peierls metal-insulator transition (see Chapter V).

In the spin-Peierls effect, a uniform 1d, $S=1/2$ spin chain undergoes a spontaneous distortion, causing dimerization, and hence the appearance of two different exchange couplings $J \pm \delta J$ (see Fig. 1.9). For δJ sufficiently large, $S=0$ singlet pairs are formed on the stronger links, implying a non-magnetic state and a finite energy gap to the excited states (see Fig. 1.8b). The Peierls state is stable if the resulting lowering of magnetic energy more than compensates for the elastic energy of the lattice distortion. Note that the distortion is a distinctive feature which is visible with hard X-ray diffraction. The spin-chain compound CuGeO_3 is an inorganic solid which undergoes a spin-Peierls transition at 14 K.

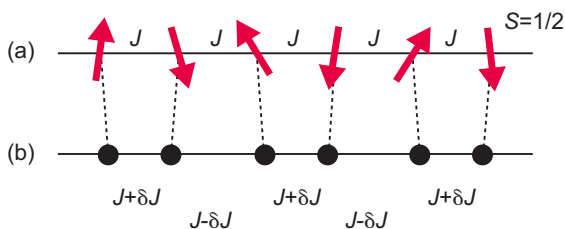


Fig. 1.9. Schematic representation of the spin-Peierls transition, caused by a dimerization of neighboring sites along a 1d $S=1/2$ Heisenberg chain.

A more subtle quantum effect also leads to an energy gap in the excitation spectrum of an antiferromagnetic Heisenberg chain of *integral* spins [17]. As conjectured by Haldane, neighboring $S=1$ spins can be resolved into

two $S=1/2$ degrees of freedom, effectively forming singlet bonds (see Fig. 1.10). This valence bond state is responsible for the existence of a Haldane energy gap, since long wavelength spin excitations cannot be generated without breaking the valence bonds. A consequence of the Haldane mechanism is a spatial correlation function for magnetic excitations which decays exponentially with distance, compared with the power-law dependence in the case of gapless excitations. An inorganic material which demonstrates the Haldane phenomenon is Y_2BaNiO_5 .

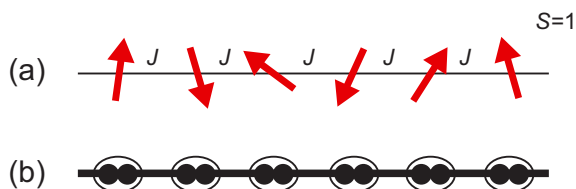


Fig. 1.10. The Haldane mechanism in a 1d $S=1$ Heisenberg chain, which produces a valence bond state and a gapped excitation spectrum.

The Haldane mechanism is also used to describe the dynamic behavior of *finite* 1d $S=1$ antiferromagnetic chains, as investigated in Mg-doped Y_2BaNiO_5 by inelastic neutron scattering [18]. The finite chains are generated by the non-magnetic Mg impurities, and the ends of the chains represent $S=1/2$ impurities with a strong nano-scale correlation, with the result that the Haldane gap becomes a function of chain length. In an applied magnetic field, the triplet spin excitations undergo Zeeman splitting, eventually becoming a new ground state (see Fig. 1.11). Thus the Zeeman transitions are hybrid excitations with both local and cooperative properties. They therefore serve as probes of the quantum correlation functions, which are otherwise difficult to access. The temperature and field ranges for such studies vary with the material, but effects can be observed in many systems at $T \sim 1$ K and $B \sim 1$ T. Some quantum magnets show *magneto-electric* interactions [19], which may allow perturbation of the quantum states by electric or optical pulses. In this case, it will be possible to probe the temporal evolution of macroscopic quantum correlations in a pump-probe experiment at the SwissFEL.

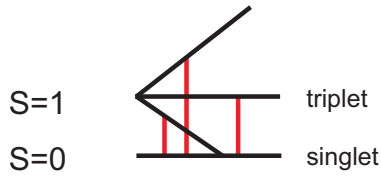


Fig. I.11: The occurrence in a singlet spin liquid at high magnetic field of a quantum phase transition [18].

Zero-dimensional case ($d=0$)

The extreme brightness of the SwissFEL allows measurements of magnetic phenomena on dilute samples consisting of isolated nanoparticles, with effectively zero dimension. A recent realization of such nanoparticles is the single-molecule magnet, manganese acetate (Mn_{12}Ac) shown in Fig. I.1, in which 12 magnetic Mn ions, with a total spin $S=10$, are held in close proximity by an organic molecular framework. Another example is the creation of magnetic nanodots by sub-monolayer deposition onto a high-index surface of a metal (see Fig. I.12). If they have a magnetic anisotropy above the superparamagnetic limit, such nanoparticles may exhibit room-temperature ferro- or antiferromagnetic order, and undergo sub-nanosecond quantum tunnelling between

different magnetization directions [21]. Details of this tunnelling, including field-enhancement of the rate, are an attractive topic in ultrafast magnetization dynamics, suitable for study with the SwissFEL.

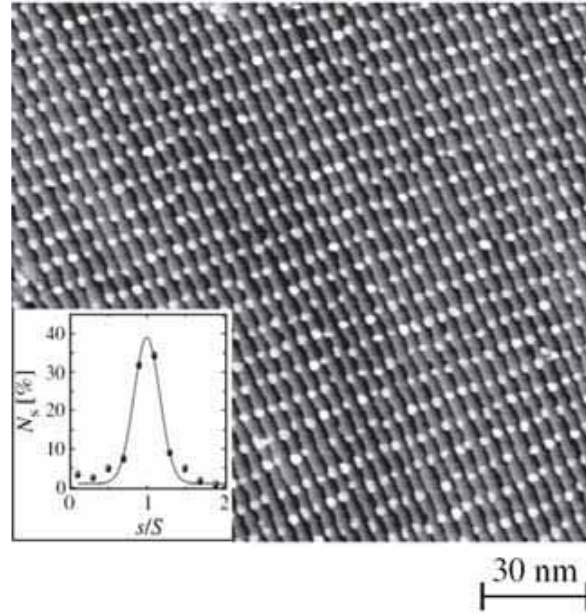


Fig. I.12. Cobalt nanodots created [20] by the deposition of 0.3 monolayers on the gold (788) surface. The inset shows the distribution of dot sizes s around the mean size $S=70$ atoms.

Summary

- *Present magnetic storage devices are limited to densities of 400 gigabits/square inch (i.e. one bit/ $40 \times 40 \text{ nm}^2$) and reading/writing times of 2 ns, while standard synchrotron-based magnetic studies are limited by the 100 ps pulse duration. The SwissFEL will investigate magnetic phenomena well beyond these values.*
- *Fundamental magnetic interactions occur on the nanometer and sub-picosecond length and time scales – which are very well matched to the capabilities of the SwissFEL.*
- *With its provision of circularly-polarized radiation, high transverse coherence and femtosecond pulse duration, the SwissFEL will accommodate the X-ray measurement techniques of particular relevance to ultrafast magnetism: X-ray magnetic circular dichroism (XMCD), magnetic-contrast holography and time-of-flight, spin-analyzed photoemission.*
- *A synchronized terahertz pump source at the SwissFEL will provide magnetic field pulses with an amplitude of approximately 1 tesla and a duration of approximately 1 picosecond, for high-bandwidth excitation in ultrafast pump-probe experiments.*
- *Synchronized femtosecond pulses of optical laser light will also be available for pumping at the SwissFEL. These cause rapid heating of the electrons of the sample, which, through as yet not understood interactions, may demagnetize a sample, cause a transition from an antiferromagnetic to a ferromagnetic state or reverse the magnetization direction. Pump-probe XMCD experiments at the SwissFEL will follow the ultrafast behavior of the spin and orbital moments during these processes.*
- *Low-dimensional systems fail to develop long-range magnetic order. The quantum fluctuations of such spin liquids represent a rich field of application for the SwissFEL.*

References

- [1] Vaz, C. A. F., Bland, J. A. C., and Lauhoff, G., "Magnetism in ultrathin film structures," *Rep. Prog. Phys.* **71**, 056501 (2008).
- [2] Stöhr, J. and Siegmann, H. C., *Magnetism: From Fundamentals to Nanoscale Dynamics* (Springer, Berlin, 2006).
- [3] Fraile Rodríguez, A., (private communication).
- [4] Eisebitt, S., et al., "Lensless imaging of magnetic nanostructures by X-ray spectro-holography," *Nature* **432**, 885-888 (2004).
- [5] Eisebitt, S., (private communication).
- [6] Back, C. H., et al., "Minimum field strength in precessional magnetization reversal," *Science* **285**, 864-867 (1999).
- [7] Boero, G., et al., "Double-resonant X-ray and microwave absorption: Atomic spectroscopy of precessional orbital and spin dynamics," *Phys. Rev. B* **79**, 224425 (2008).
- [8] Beaurepaire, E., Merle, J. C., Daunois, A., and Bigot, J. Y., "Ultrafast spin dynamics in ferromagnetic nickel," *Phys. Rev. Lett.* **76**, 4250-4253 (1996).
- [9] Koopmans, B., Kicken, H., Van Kampen, M., and de Jonge, W. J. M., "Microscopic model for femtosecond magnetization dynamics," *J. Magn. Mater.* **286**, 271-275 (2005).
- [10] Kazantseva, N., Nowak, U., Chantrell, R. W., Hohlfeld, J., and Rebei, A., "Slow recovery of the magnetisation after a sub-picosecond heat pulse," *Europhys. Lett.* **81**, 27004 (2008).
- [11] Thiele, J. U., Buess, M., and Back, C. H., "Spin dynamics of the antiferromagnetic-to-ferromagnetic phase transition in FeRh on a sub-picosecond time scale," *Appl. Phys. Lett.* **85**, 2857-2859 (2004).
- [12] Kläui, M., (private communication).
- [13] Lacroix, C. in *Magnetism: A Synchrotron Radiation Approach* (ed. É. Beaurepaire, H. B., F. Scheurer) (Springer, Berlin, 2006).
- [14] Bloch, F., "Zur Theorie des Ferromagnetismus", *Z. für Phys A. Col.*, 206-219 (1930).
- [15] Mermin, N. D. and Wagner, H., "Absence of ferromagnetism or antiferromagnetism in one- or two-dimensional isotropic Heisenberg models," *Phys. Rev. Lett.* **17**, 1133-1136 (1966).
- [16] Cloiseau, J. D. and Pearson, J. J., "Spin-wave spectrum of the antiferromagnetic linear chain," *Phys. Rev.* **128**, 2131-2135 (1962).
- [17] Haas, S., Riera, J., and Dagotto, E., "Dynamical properties of antiferromagnetic Heisenberg spin chains," *Phys. Rev. B* **48**, 3281-3286 (1993).
- [18] Kenzelmann, M., et al., "Structure of end states for a Haldane spin chain," *Phys. Rev. Lett.* **90**, 087202 (2003).
- [19] Zapf, V.G., Kenzelmann, M., Wolff-Fabris, F., Balakirev, F., and Chen, Y., "Magnetically – induced electric polarization in an organo-metallic magnet," *cond-mat/0904.4490* (2009).
- [20] Weiss, N., et al., "Uniform magnetic properties for an ultrahigh-density lattice of noninteracting Co nanostructures," *Phys. Rev. Lett.* **95**, 157204 (2005).
- [21] Dressel, M., Gorshunov, B., Rajagopal, K., Vongtragool, S., and Mukhin, A. A., "Quantum tunneling and relaxation in Mn-12-acetate studied by magnetic spectroscopy," *Phys. Rev. B* **67**, 060405 (2003).
- [22] Gallani, J.-L., private communication.
- [23] Malinowski, G., Longa, F.D., Rietjens, J.H.H., Paluskar, P.V., Huijink, R. Swagten, H.J.M. & Koopmans, B., "Control of speed and efficiency of ultrafast demagnetization by direct transfer of spin angular momentum", *Nature Physics* **4**, 855-858 (2008).
- [24] Cowan, B. *Topics in Statistical Mechanics* (World Scientific, Singapore, 2005).
- [25] Ziel, J. P. v. d., P.S.Pershan, and L.D.Malstrom, "Optically-induced magnetization resulting from the inverse Faraday effect," *Phys. Rev. Lett.* **15**, 190-193 (1965).
- [26] Stanciu, C. D., et al., "All-optical magnetic recording with circularly polarized light," *Phys. Rev. Lett.* **99**, 047601 (2007).
- [27] Hertel, R., Gliga, S., Fahnle, M., and Schneider, C. M., "Ultrafast nanomagnetic toggle switching of vortex cores," *Phys. Rev. Lett.* **98**, 117201 (2007).

II. Catalysis and Solution Chemistry

Structure and lifetime of short-lived molecular states in solution or on a catalytic surface

- Chemical time scales
- X-ray probes of chemical dynamics
- CO chemistry on Ru (001): thermal vs. electronic excitation
- The high- and low-spin states of $[\text{Fe}^{\text{II}}(\text{bpy})_3]^{2+}$

In order to obtain a complete microscopic understanding of a chemical process, whether it be synthetic, catalytic, or biochemical, one needs to identify the geometrical and electronic structures of the short-lived molecular intermediate states involved and to determine the rates of transition between them. This deeper understanding will lead to the ability to manipulate these reactions, allowing us to control and enhance them to suit our purposes. Since molecular vibrations can lead to the breaking and reforming of chemical bonds, the vibrational period represents a fundamental time-scale for chemical processes. For example, the C=C bond of an ethene molecule acts as a spring, and the characteristic stretch vibrational mode of the resulting harmonic oscillator has a period of 19 fs. With its nm spatial and fs temporal resolution, the SwissFEL is a unique tool for the investigation of chemical states on this time scale: The scattering of hard X-rays and photoelectrons from the atoms of the molecule provides a detailed geometrical structure, and the energy-dependent X-ray absorption and emission spectra reveal details of the electronic orbitals involved. This interplay between electron orbitals and geometric structure is at the very heart of chemistry, as it is the energy and shape of a molecule which determine its reactivity. The SwissFEL will allow us to visualize chemistry with unprecedented accuracy, permitting us to construct a molecular movie of reactions as they take place.

Chemical time scales

A principal application of the SwissFEL will be the study of molecular dynamics and reactivity in solution and in heterogeneous catalysis. (Note that applications in *bio*-chemistry are the subject of Chapter IV.) Time scales of a range of chemical phenomena in *solution* are shown in Figure II.1. At the slow end of the scale is the diffusional rotation of a molecule in a solvent. The recombination of photo-dissociated molecules occurs on the ps to ns scales, depending upon whether the recombining reactants arise from the same (geminate) or different (non-geminate) parent molecules. Several types of deactivation processes may occur in an intact photoexcited molecule: “Internal conversion” (10–100 fs) is an electronic reconfiguration in which the total electronic spin is conserved, while slower “intersystem crossing” (1–10 ns) involves a change of spin. Molecular cooling and vibrational energy transfer from a high to a low vibrational state generally occur in 1–100 ps. The exchange of a water molecule in the solvation shell surrounding an ion requires approximately 250 ps, and further ultrafast processes in ionized water are shown schematically in Figure II.2, including the formation and stabilization of the solvated electron within 1 ps, which has proven to be critically important in both photocatalysis and electrochemistry [1].

Catalysis is the enabling technology in a large number of processes for the production of goods, the provision of clean energy, and for pollution abatement. Heterogeneous catalysis occurs at the interface between a gas or liquid and a solid catalytic surface; the surface of a catalytically active solid provides an energy landscape which enhances reactivity. A large number of processes are active here on the nanometer scale (see Fig. II.3), with characteristic times ranging from sub-fs, for electron transfer, to minutes, for the oscillating patterns studied by Ertl et al. [3] and to even months, for the deactivation of catalytic processes. The cartoon in Figure II.3 “schematically depicts, at the molecular level, the richness of the phenomena involved in the transformation of reactants to products at the surface of a material. A molecule may scatter off the surface, experiencing no or some finite degree of energy exchange with the surface. Alternatively, molecule-surface energy transfer can lead to accommodation and physical adsorption or chemical adsorption. In some cases, physisorption is a precursor to chemisorption, and in some cases, bond dissociation is required for chemisorption. Charge transfer plays a critical role in some adsorption processes. Once on the surface, the adsorbed intermediates may diffuse laterally with a temperature-dependent rate, sampling surface features including adatoms, vacancies and steps. They may become tightly bound to a defect site. Various ad-

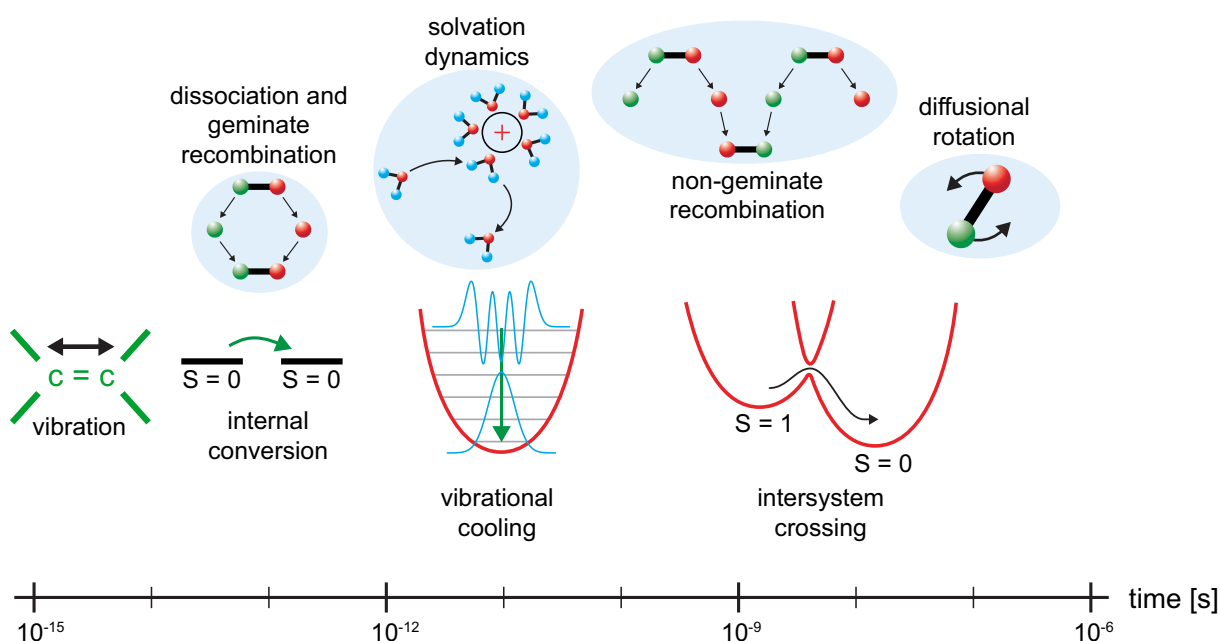


Fig. II.1: The time scales for chemical processes in solution match well the capabilities of the SwissFEL.

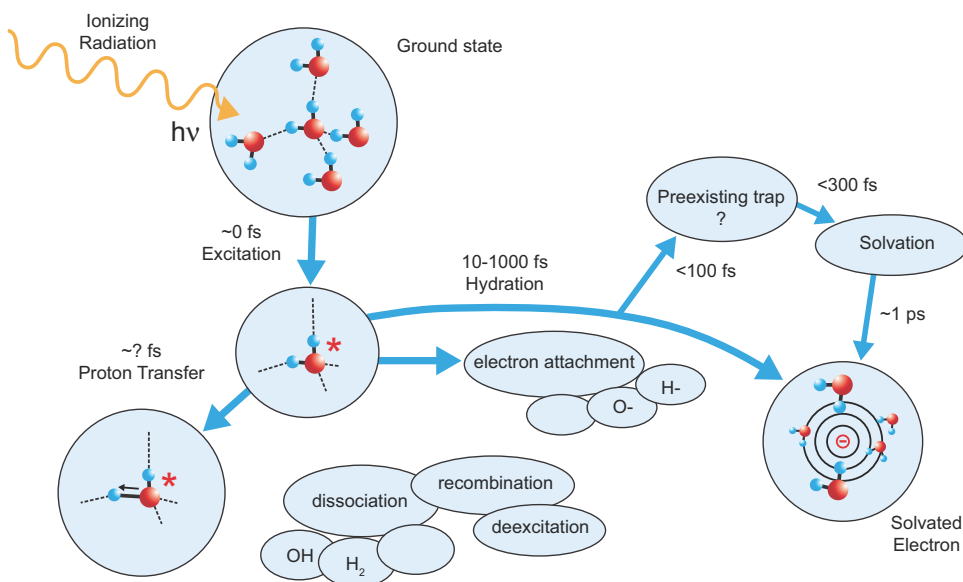


Fig. II.2. Ultrafast processes in water, following a photoionization event [1]. The formation and stabilization of a solvated electron is fundamental in photocatalysis and radiation chemistry.

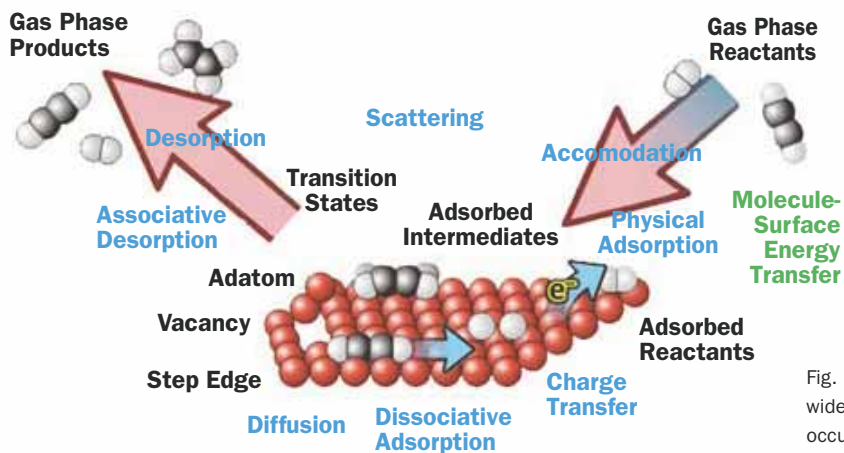


Fig. II.3. A schematic representation of the wide range of ultrafast nanoscale phenomena occurring on a catalytic surface [2].

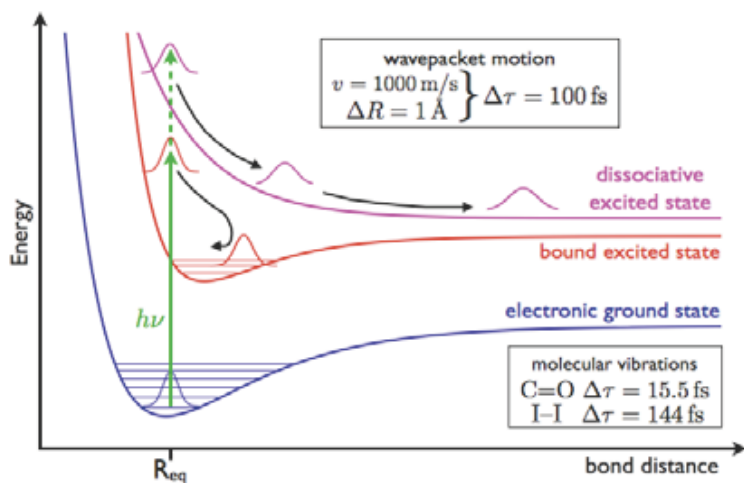


Fig. II.4. Impulsive photo-excitation of a molecule in the wave-packet picture. During a typical reaction, the excited-state packet moves a distance of the order of $\Delta R = 1$ Å.

sorbed intermediates may meet, either at defect sites or at regular lattice sites, and form short-lived transition state structures and ultimately product molecules. Finally, products desorb from the surface with a temperature dependent rate, imparting some fraction of the energy of the association reaction to the surface” [2].

Within the Born-Oppenheimer approximation, as a chemical system moves from a configuration of high energy towards a potential minimum, the electrons are assumed to instantaneously follow the motion of the much heavier nuclei. The uncertainty in nuclear position during the reaction is then represented by a wave-packet, and the time development during the reaction can be viewed as the motion of the packet along a trajectory on the potential energy surface. A schematic impulsive photo-excitation process and the resulting wave-packet motion are shown in Figure II.4, where one sees that for a typical 0.1 nm atomic displacement and 100 fs vibrational timescale, the velocity for wave-packet motion is of order 1000 m/s. It should be noted that the Born-Oppenheimer approximation may break down, particularly for light chemical elements. Such non-adiabatic couplings are prevalent at critical points on the potential energy surface, where two surfaces repel one another at an avoided crossing, or where they meet at a point – a conical intersection. It is at these critical points that chemical reactions occur. Also at metal surfaces, non-adiabatic couplings are frequently observed between adsorbate motion and electronic excitations in the metal substrate.

It is clear that predominant mechanisms of solution and surface catalytic processes are active on the nm length and fs to ns time scales. This richness of behavior serves as a strong justification for the SwissFEL, as a powerful tool for the study of ultrafast chemistry.

THz initiation of surface reactions

The intensity (power/area) delivered by an electromagnetic wave is $I = \epsilon_0 E_0^2 c / 2$, implying that a half-cycle 100 μJ pulse of THz radiation, focused to 1 mm², will produce a peak electric field $E_0 = 4 \times 10^8$ V/m, which is comparable to the field exerted on an adsorbed atom by a scanning tunneling microscope tip used to manipulate atoms [15]. One thus envisages the collective control of atomic positions using the THz pulse (Fig. II.i1).

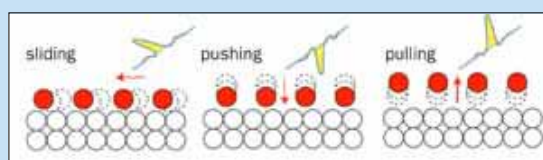


Fig. II.i1. Collective control of adsorbed atoms using the electric field of a half-cycle THz pulse [15].

Since the phonon frequencies of the host and the local vibration frequencies of adsorbed atoms and molecules lie in the terahertz region, THz pulses can resonantly excite these modes. Finally, E_0 from the THz pulse is of order 1‰ of the field felt by the electron in a Bohr H-atom, opening the possibility of using dynamic Stark control to influence a chemical reaction (Fig. II.i2).

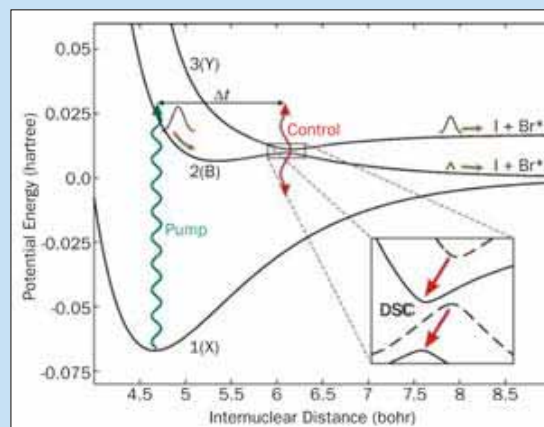


Fig. II.i2. Dynamic Stark control can be used to influence the outcome of a chemical reaction, in this case the photodissociation of IBr [16].

A micro-liquid jet in vacuum

The investigation with the SwissFEL of chemical dynamics in solution will require a rapidly renewable liquid sample, which is compatible with the beamline vacuum. These requirements can be met with a high-velocity fluid jet from a small nozzle, at the limit for laminar flow. Fig. II.i3 shows the example of a 6 μm diameter jet, with a flow velocity of 120 m/s, which, when outfitted with a small-aperture skimmer, can be attached to an X-ray photoelectron spectrometer at 10^{-9} mbar.

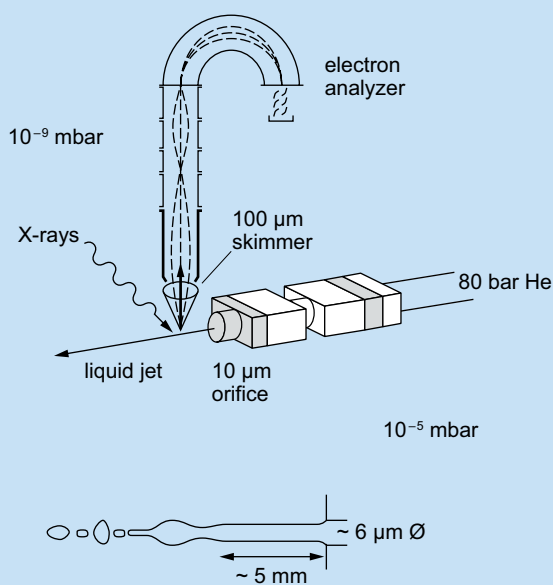


Fig. II.i3. A micro-liquid jet in vacuum, suitable even for X-ray photoemission spectroscopy in ultra-high vacuum [17, 18].

X-ray probes of chemical dynamics

Since important chemical processes are often irreversible, principal SwissFEL applications will use the pump-probe method: An external fast trigger, e.g., an optical, IR, or THz pulse, initiates a reaction, typically involving vibration, relaxation, and/or dissociation, and the SwissFEL delivers a synchronized hard- or soft-X-ray pulse to probe the subsequent processes. Historically, ultrafast chemistry experiments have been performed with fs laser pump pulses as the reaction initiator. The intriguing possibility of using non-ionizing THz radiation to initiate a surface catalytic reaction in the electronic ground state is the subject of an Infobox. As with the majority of high-intensity SwissFEL experiments, it will be necessary to refresh the sample between measurements, for example using a high-speed liquid jet for solutions (see Infobox) or a movable surface for catalytic reactions.

In a solution environment, optical pump pulses pose a problem in the ultrafast regime: As the desired time resolution improves, not only the probe pulse, but also the pump pulse must become shorter. Since it is the pump *energy* which determines the degree of photoexcitation in the sample, the peak intensity must increase as the pulse duration decreases. By delivering a large number of photons in such a short period of time, competing excitation processes in both the sample and the solvent become increasingly relevant. In order to avoid such potential complications as nonlinear sample excitation, multiphoton solvent ionization and, at longer pump wavelengths, tunneling ionization, a balance must be maintained between generating a sufficient level of sample excitation and ensuring that only the photoreaction of interest is being probed, and not a highly excited plasma. To achieve this balance, it will be necessary to perform laser spectroscopic pump-probe measurements in the optical regime prior to the SwissFEL measurements, using the same pump conditions as will be used with the X-ray probe.

Two basic methods are proposed to probe intermediate chemical states with X-rays: scattering and absorption/emission spectroscopy.

X-ray scattering to probe chemical structure

Monochromatic hard X-rays (>3 keV) will easily penetrate a liquid jet (see Infobox) and are scattered into a 2d-detector by the solute and solvent molecules. Depending on the angular range collected, one speaks of small-angle (SAXS) or wide-angle (WAXS) X-ray scattering; there

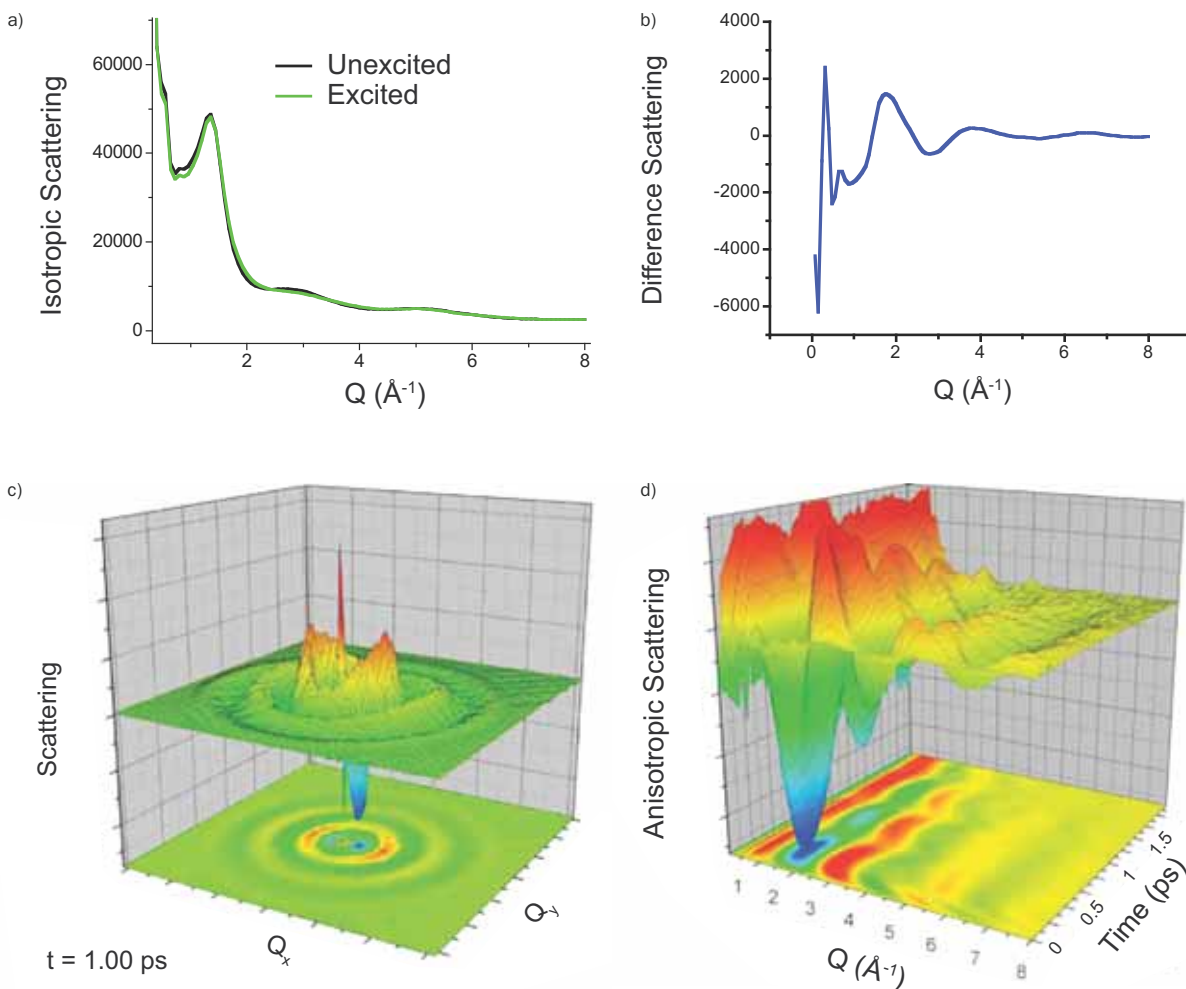


Fig. II.5. Pump-probe scattering simulation for one I₂ solute molecule surrounded by 100 solvent hexane molecules [4]. a) The isotropic part of the unexcited (black) and excited (green) scattering at a particular pump-probe delay, as a function of the scattering vector. b) The difference scattering: excited minus unexcited. c) A contour plot of the difference scattering, at a 1 ps pump-probe delay. The polarization of the pump laser pulse (along the x-direction) is responsible for the anisotropic X-ray scattering. d) The time- and scattering-vector-dependent anisotropic part of the difference scattering, showing the vibration of the excited-state.

is an inverse relation (related to Bragg's law for crystal diffraction) between the scattering angle and the length scale responsible for the scattering. Advantages of X-ray scattering for pump-probe investigations of chemical processes include the use of a fixed X-ray wavelength, a straightforward data analysis and the ability to probe large structural motions. Disadvantages of scattering are the necessity of an elaborate 2d-detector and the unavoidable background scattering from solvent molecules. The latter may be alleviated by choosing a resonant photon energy with enhanced scattering from the solute atoms. Although X-ray scattering is based on coherent interference, in the case of scattering from dissolved molecules, the long transverse coherence

length of the SwissFEL radiation is not of particular advantage – indeed, the speckles resulting from coherent scattering by widely separated molecules will occur on an angular scale which is too fine to resolve.

As an example of the information available from pump-probe solution scattering, consider the simulated scattering by photoexcited molecular iodine dissolved in hexane, performed by B. Zietz (EPFL, PSI). From the scattering profiles in Figures II.5a and b, one can appreciate the challenge to obtain an acceptable signal-to-noise ratio. This task will be made still more difficult by pulse-to-pulse fluctuations in the SwissFEL intensity. Because of the linear polarization of the pump laser pulse (along the x-direction in the simulation), favorably-

Single-shot XANES / XES

When performing pump-probe X-ray spectroscopy with the SwissFEL, it will be highly advantageous to avoid the requirement of tuning the incoming X-ray wavelength, hence allowing for single-shot data collection. This is possible using X-ray emission spectroscopy (XES), where monochromatic X-rays cause characteristic fluorescence over a wide range of wavelengths. Alternatively, one can make use of the broadband emission mode of the SwissFEL, with detuned undulator modules, to perform single-shot X-ray near-edge absorption spectroscopy (XANES).

XES requires an efficient energy-dispersive X-ray detector. A possible design for such a detector, based on a deeply-etched, flexible silicon analyzer and the very successful MYTHEN detector from PSI [19] is shown in Fig. II.i4.

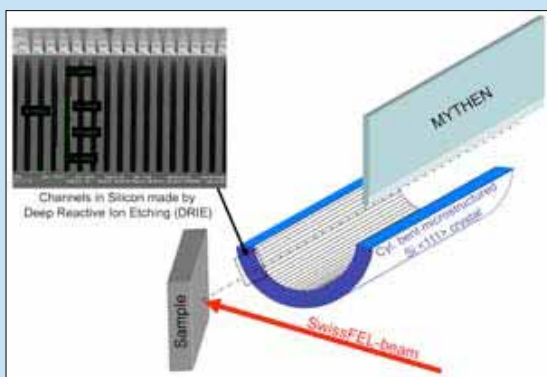


Fig. II.i4. A novel design for a compact energy-dispersive detector for single-shot XES experiments. Deeply-etched channels in the Si-crystal analyzer [20] allow it to be bent to produce focussing onto the linear-array MYTHEN detector.

oriented I_2 molecules will be preferentially excited, leading to the anisotropic X-ray scattering pattern in Figure II.5c. This anisotropy avoids the problem of the pulse-to-pulse variations, since both excited and unexcited scattering is registered in a single measurement. Finally, the time-dependence of the anisotropic scattering, shown in Figure II.5d, includes an oscillating component, corresponding to the excited-state wave-packet vibration of I_2 , and a decrease in anisotropy, due to diffusional rotation. By controlling the pump laser wavelength and fluence, one can influence such processes as dissociation, solvent caging effects, geminate recombination, and non-geminate recombination, making pump-probe X-ray scattering a prolific source of chemical information.

X-ray spectroscopy to probe electronic and geometric structure

X-ray spectroscopic signatures of the solute molecule contain a wealth of element-specific information about, e.g., valence, bonding configuration and local structure. The probing X-rays must either be tunable in energy around a resonant atomic absorption edge, ranging from the soft X-ray regime (e.g., C, N, O) to the hard X-ray regime (Fe, Ru, Pt), or be of sufficient bandwidth to cover the principal spectroscopic features of interest. Detection can be as simple as a transmission measurement or as complex as an energy-dispersed fluorescence measurement. In an X-ray absorption measurement, one differentiates between XANES (X-ray absorption near-edge structure) measurements, taken within 40 eV of the absorption edge, and EXAFS (extended X-ray absorption fine structure) measurements, extending up to 1 keV above the edge (see Fig. II.6).

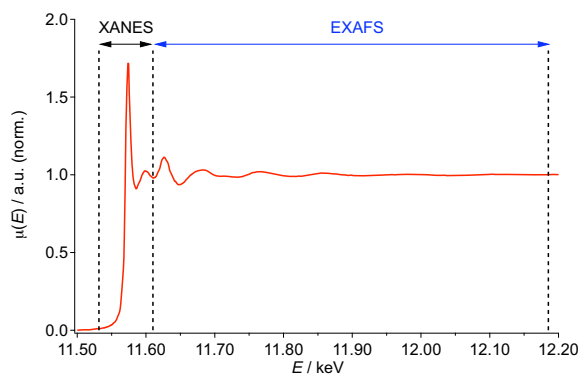


Fig. II.6. A plot of the dependence of X-ray absorption on photon energy, showing the near-edge (XANES) and extended (EXAFS) photon-energy regions. The data is taken at the Pt L_3 -absorption edge in a photocatalytically active diplatinum complex [5].

In an EXAFS measurement, the incoming X-ray photon energy is set to a value $E = E_0 + \Delta E$, above an absorption edge. This causes the emission, to first approximation, of a spherical photoelectron wave from the absorbing atom with kinetic energy ΔE , and hence a de Broglie wavelength $\lambda_e = h / \sqrt{2m_e \Delta E}$. This spherical wave then reflects on the nearest-neighbor atoms, at the distance R_1 , returning (after a round-trip distance $2R_1$) to the absorbing atom with the phase shift $\Delta\phi = 4\pi R_1 / \lambda_e$. Constructive interference at the absorbing atom of the (virtual) photoelectron waves will occur if $\Delta\phi$ is an integral multiple of 2π , causing a maximum in the quantum mechanical probability of the original photoelectron absorption. Hence, as the incoming photon energy is scanned above the absorption edge, λ_e will vary, and the photoabsorption probability will oscillate. A Fourier analysis of the absorption signal yields the distance to the nearest-neighbors, as well as that to more distant shells. In this way, EXAFS provides a sensitive signature of the local geometric structure around the absorbing atom and of the type of neighboring atoms. For the SwissFEL, performing a pump-probe EXAFS experiment requires tuning the XFEL wavelength, by combined variation of the accelerated electron energy and of the undulator gap. Furthermore, careful shot-by-shot normalization of the incoming intensity is necessary.

The full-bandwidth SwissFEL pulses will have an intrinsic spectral width of approximately 0.1%, which, at moderate X-ray energies, will provide sufficient bandwidth to perform single-shot measurements of particular XANES features. The SwissFEL will further present the possibility, through detuning of the individual undulator modules, of generating a tailored single-shot bandwidth of the order of 1–2%, at the cost of beam intensity. In either case, an energy-dispersive detector is required (see Infobox).

In contrast to scattering (and EXAFS), the interpretation of XANES is complicated and enriched by the combination of geometrical structure and electronic effects, involving consideration of a large number of unoccupied electronic states of the central atom and its neighbors (see Fig. II.7 and the Infobox) as well as more complicated multiple scattering pathways due to the long de Broglie wavelength of the photoelectron near the absorption edge.

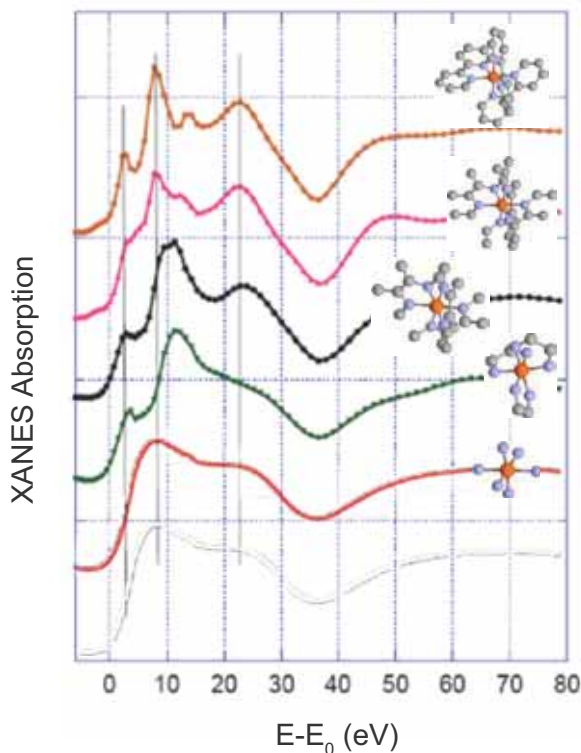


Fig. II.7. A theoretical near-edge XANES X-ray absorption spectrum, calculated using the program MXAN [6] for the Fe K-edge in the ground state of $[\text{Fe}^{\text{II}}(\text{bpy})_3]^{2+}$ and showing the effect of adding subsequent coordination shells of neighboring atoms.

An example of the power of XANES to determine the atomic arrangement of a chemisorbed species is provided by the static measurements at the Pt L_3 -edge of CO on the catalytic surface of Pt nanoparticles, shown in Figure II.8 [7].

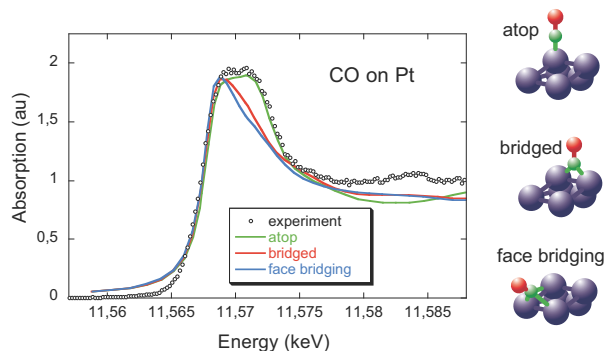


Fig. II.8. Static XANES measurements of CO adsorbed on the surface of Pt nanoparticles, demonstrating that the adsorption site is “atop” [7]. With pump-probe experiments at the SwissFEL, such measurements can be performed on short-lived intermediate states.

XES and RIXS

Whereas the XANES (X-ray absorption near-edge structure) technique yields information on the local coordination, valence and electronic structure of the absorbing atom, the emission spectroscopies XES (X-ray emission spectroscopy) and RIXS (resonant inelastic X-ray spectroscopy), being sensitive to electron-electron interactions in the occupied levels, yield complementary information: In addition to the local symmetry and coordination, XES gives orbital splittings and spin- and oxidation-states. The resonant technique, RIXS, provides access to low-energy excitations arising from local (e.g., *d-d*), nearest-neighbor (e.g., charge-transfer) and collective (e.g., plasmon) interactions and is described more fully in Chapter V.

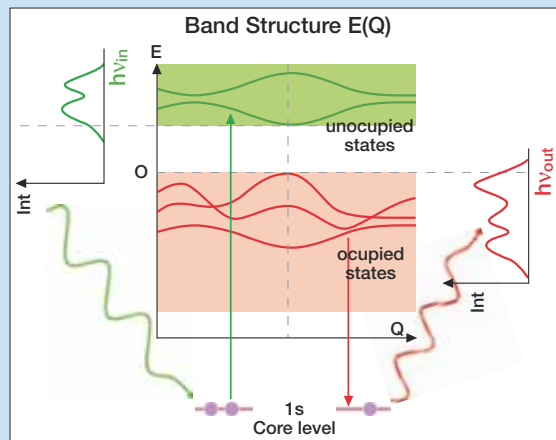


Fig. II.i5. A schematic comparison of the XANES (green) and XES (red) techniques. The former probes unoccupied states and the latter occupied states.

An alternative single-shot X-ray spectroscopic method, suitable for use in a pump-probe SwissFEL experiment in chemical dynamics, is X-ray *emission* spectroscopy (XES). Here, a probe pulse of monoenergetic X-rays, with photon energy close to and greater than a resonant absorption edge, is applied to the laser-excited sample, and the X-ray fluorescence spectrum is measured in a wide-acceptance, energy-dispersive detector. XANES and XES yield complementary information: XANES on the *unoccupied* electronic levels and XES on the occupied levels (Infobox). A strong enhancement of the (inelastic) fluorescence yield occurs when the incoming radiation is resonant with an electronic transition. The measurement, called resonant inelastic X-ray spectroscopy (RIXS), is then sensitive to low-lying excitations of the absorbing ion, of its immediate neighborhood, or even of the entire sample (see Chapter V).

Finally, another related spectroscopic option to probe chemical systems is the non-resonant inelastic (Raman) scattering of hard X-rays. Because it is far from resonance, the scattered photon yield is very small. But the ability to observe low-energy absorption features using penetrating radiation is of great interest for phenomena occurring, for example, at interfaces covered with a water layer, such as the liquid-phase electrochemistry at a water-covered fuel-cell electrode.

The combination of scattering and spectroscopic techniques provided by the SwissFEL, over a wide range of important elemental absorption edges and in a pump-probe experimental arrangement, makes it an invaluable tool for understanding the short-lived molecular structures and electronic states involved in solution-phase and catalytic chemical reactions.

CO chemistry on Ru (001): thermal vs. electronic excitation

As an example of the type of ultrafast chemical phenomena which occur on a catalytic surface, and which lend themselves to pump-probe investigations at the SwissFEL, results are presented from the oxidation of carbon monoxide on ruthenium [8]. This is a model reaction for catalytic processes of great practical interest, e.g. for the automotive industry.

Consider a Ru (001) surface with co-adsorbed CO and atomic oxygen (see Fig. II.9); the goal is the catalytic oxidation of CO to less toxic CO₂. According to conventional wisdom, surface catalysis is initiated by energy transfer in thermal equilibrium from the substrate phonons to the chemical adsorbates. However, in the present instance, heating of the substrate simply causes desorption of CO. Upon photoexcitation with a visible laser, energy is transferred to near-surface conduction elec-

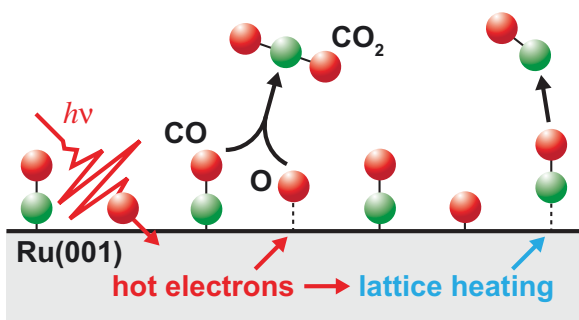


Fig. II.9. Photo-induced processes involving CO and O adsorbed on a Ru (001) surface. The laser pump pulse excites the conduction electrons of the substrate, which transfer their energy to either CO desorption or CO₂ formation [8].

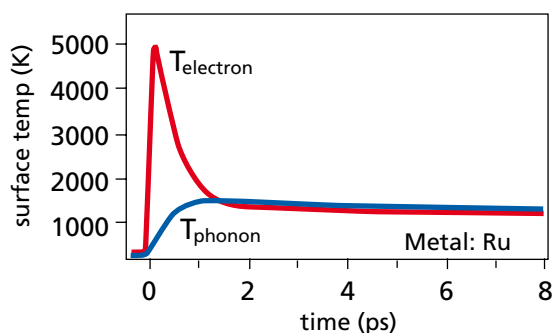


Fig. II.10. A two-temperature model for the energy exchange between the Ru conduction electrons, phonons and adsorbates. The electron temperature has a much shorter time constant than the phonons [8].

trons. Time-resolved experiments of molecular yields [9] have established that the energy then flows from the hot electrons to the adsorbates in two different ways: via excitation of the substrate phonons or by direct transfer of hot electrons to the adsorbates. The result of model calculations for the time-dependent temperatures of the electron and phonon heat reservoirs is shown in Figure II.10.

Energy transfer to the adsorbates via phonons is relatively slow compared to the direct action of hot electrons. This can be understood in terms of the wave-packet diagram in Figure II.11. Since the phonon reservoir can only accept energy from the hot electrons in units of the small energy $\hbar\omega_{\text{phonon}}$, many units must accumulate in order to initiate a catalytic reaction. Alternatively, a hot electron can directly hop to an adsorbate, forming an excited, antibonding ionic species, which leads to rapid wave-packet motion away from the surface.

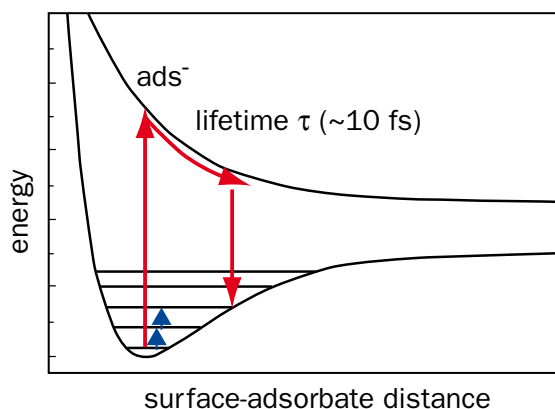


Fig. II.11. Adsorbate wave-packet motion for slow phonon (blue arrows) and rapid hot electron (red arrows) excitations [8].

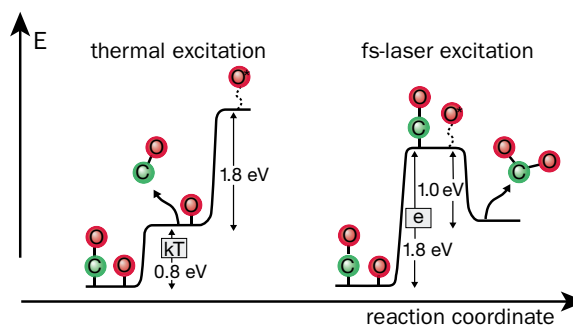


Fig. II.12. A comparison of the slow, phonon-mediated desorption of CO (left) and the fast, hot-electron mediated oxidation reaction (right) on the (001) surface of Ru [8].

The resulting picture of CO and O catalytic photochemistry on Ru (001) is thus as follows (see Fig. II.12): The conventional “slow” channel of energy transfer (left) proceeds via the stepwise excitation of Ru phonons, resulting in CO desorption, before the oxidation reaction is activated. However, if photoexcited hot electrons are present, a “fast” reaction channel is opened up (right), whereby adsorbed oxygen becomes activated, combines with CO and desorbs as CO₂. The experimental proof of this hot electron channel is provided by exciting the surface with two separate laser pulses. When the pulse separation is sufficiently long that the electron reservoir can cool down in between, only the phonon channel is active. If the pulses are applied in rapid succession, however, the electrons can heat up sufficiently to open the fast hot electron channel.

These ultrafast investigations of catalytic CO oxidation were performed using fs laser pulses. The elemental specificity, sensitivity to electronic configuration and wavelength-matching to atomic dimensions provided in addition by the SwissFEL open a multitude of further experimental possibilities. The identification of an ultrafast photosensitive hot-electron channel for the initiation of catalytic reactions is very promising for ultrafast pump-probe studies of heterogeneous catalysis with the SwissFEL.

The high- and low-spin states of [Fe^{II}(bpy)₃]²⁺

The molecule iron(II) tris-bipyridine, in aqueous solution, shows an ultrafast photocycle with a variety of particularly interesting features. As in oxygenated myoglobin and hemoglobin, the central Fe²⁺ ion in [Fe^{II}(bpy)₃]²⁺ is 6-fold coordinated, providing an approximately octahedral environment. Similar to the crystal field splitting experienced by octahedrally-coordinated metal ions in transition metal oxides (see Chapter V), the bipyridine ligand fields in [Fe^{II}(bpy)₃]²⁺ cause a splitting of the five Fe 3d-orbitals into a three-fold t_{2g} and a two-fold e_g state (see Fig. II.13). This splitting results in an S=0 low-spin singlet ground-state and an S=2 high-spin quintet excited state. The high-spin state is accompanied by a lengthening Δr(Fe-N) of the Fe-N bonds, since the e_g states are of anti-bonding character.

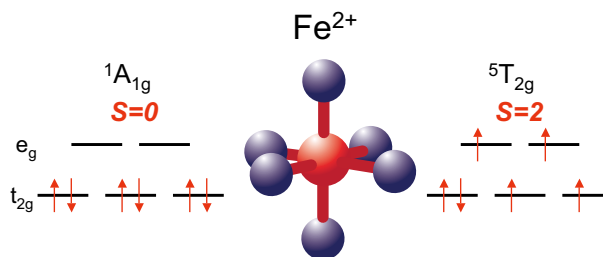


Fig. II.13. The ligand-field splitting of Fe²⁺ in [Fe^{II}(bpy)₃]²⁺, caused by the quasi-octahedrally coordinated N-atoms, leading to a low-spin singlet ground-state and a high-spin quintet excited state.

Molecular complexes having low- and high-spin states with a small energy difference, and for which transitions between them can be induced by temperature or pressure, are called spin-crossover systems. The state energies and transition rates are sensitive to the nature and the bonding distance of the ligand groups. As discussed in Chapter V, a large ligand-field splitting allows Hund’s rule to be violated, stabilizing a low-spin state. In the biologically important hemoglobin, this ligand sensitivity leads to a cooperative effect in oxygen affinity: In the oxygenated state, the local environment of the iron ion is nearly planar, and a large ligand splitting stabilizes the S=0 low-spin state, reinforcing the oxygen binding. In a reducing environment, the iron-oxygen bond is broken, producing a “domed” geometry around the iron, with a small ligand splitting, for which the high-spin S=2 state is more stable. In this way, the oxygen affinity shows a non-linear on-off dependence on the local oxygen concentration.

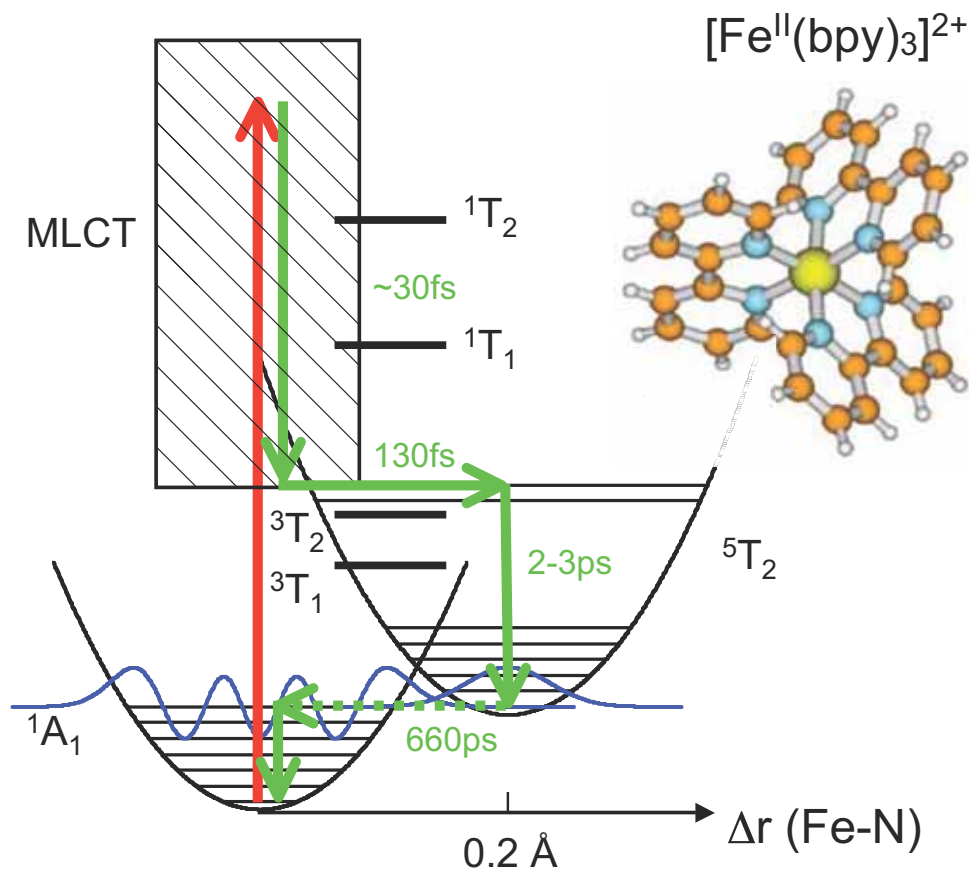


Fig. II.14. The electronic states [10] and the photocycle in iron tris-bipyridine. “MLCT” refers to metal-ligand charge transfer states. Understanding such ultrafast structural changes is an ideal type of study for the SwissFEL.

It has been found spectroscopically that photoexcitation of $[\text{Fe}^{\text{II}}(\text{bpy})_3]^{2+}$, in which an iron $3d$ -electron is excited into the continuum of metal-to-ligand charge transfer states, leads to a short-lived high-spin state, via the photocycle shown in Figure II.14. By probing the photoexcited system with 70 ps synchrotron X-ray pulses, the geometric structure of the high-spin quintet state could be measured [11], revealing an increase in the Fe-N bond distance of 0.2 \AA . The relaxation back to the singlet ground-state was measured to be 660 ps , in agreement with laser spectroscopic results [12]. By careful selection of a feature in the XANES region of the energy spectrum sensitive to the Fe-N bond distance, the arrival of the molecule in the high-spin state from the initially excited MLCT states, within 150 fs , was measured for the first

time [13] using the femtosecond hard X-ray slicing beamline at the Swiss Light Source [14]. Of particular interest are the unusually fast singlet \rightarrow quintet and quintet \rightarrow singlet intersystem crossings – much faster than the conventional wisdom shown in Figure II.1 – which avoid the $1T$ and $3T$ states. These unexpectedly high conversion rates are indicative of relaxation in the strongly non-Born-Oppenheimer regime.

The laser-sliced synchrotron beamline produces approximately 200 X-ray photons per pulse, at 1% bandwidth and a 2 kHz repetition rate, resulting in long measurement times at only a few selected settings of photon energy and pump-probe delay. With of the order of 10^{11} photons per pulse at $100\text{--}400\text{ Hz}$, the SwissFEL will bring a vast improvement in flux to such experiments.

Summary

- *A chemical process implies a redistribution of electronic charge, which alters the forces acting on the nuclei, resulting in a dynamic change of the geometric structure on the time scale of a molecular vibration (10 fs).*
- *A laser pump pulse induces optical transitions and produces hot electrons, which can efficiently trigger a chemical reaction. Energetic terahertz pulses, of ps duration, can influence chemical processes on catalytic surfaces, by physically displacing atoms, by exciting molecular or phonon vibrations, or via the Stark-mixing of electronic levels.*
- *X-ray scattering yields sub-nm-scale geometrical information, but is complicated by contributions from molecules of the solvent and the unexcited fraction of the solute.*
- *EXAFS, XANES, and XES provide both structural information and details of electronic structure, with elemental specificity. Both XANES and XES can be performed at the SwissFEL in single-shot mode, where sufficient photons are available in one pulse to obtain a spectral measurement.*
- *The industrially-relevant oxidation of CO on a catalytic metal surface demonstrates the existence of both electron- and phonon-mediated excitation mechanisms. Mediation via photoexcited hot electrons provides an ultrafast chemical pathway suitable for probing fs processes.*
- *The spin-crossover molecule iron(II) tris-bipyridine in aqueous solution, a model case for the biological action of hemoglobin, shows unusually fast intersystem crossings between low- and high-spin states, possibly involving non-Born-Oppenheimer dynamics.*
- *The extremely bright, ultrafast pulses of the SwissFEL will allow the detailed study of short-lived intermediate states in chemical reactions, leading to the optimization, and eventually control, of important chemical processes.*

References

- [1] Nilsson, A., Nordlund, D., and Ogasawara, H., (private communication).
- [2] BNL, Surface Chemical Dynamics Program, http://www.bnl.gov/chemistry/programs/Surface_dynamics.asp.
- [3] Ertl, G., "Research with surface science", *Chin. J. Catal.* **28**, II-V (2007).
- [4] Zietz, B., (private communication).
- [5] Van der Veen, R. M., et al., "EXAFS structural determination of the Pt-2(P2O5H2)(4)(4-) anion in solution," *Chimia* **62**, 287-290 (2008).
- [6] Benfatto, M. and Chergui, M., (private communication).
- [7] Safonova, O. V., et al., "Identification of CO adsorption sites in supported Pt catalysts using high-energy-resolution fluorescence detection X-ray spectroscopy," *J. Phys. Chem. B* **110**, 16162-16164 (2006).
- [8] Wolf, M., Ultrafast Surface Dynamics Group, <http://users.physik.fu-berlin.de/~femtoweb/newfemtos/welcome.php>.
- [9] Wagner, S., et al., "Activated associative desorption of C plus O -> CO from Ru(001) induced by femtosecond laser pulses," *New J. Phys.* **10**, 125031 (2008).
- [10] Daku, L. M. L., Vargas, A., Hauser, A., Fouqueau, A., and Casida, M. E., "Assessment of density functionals for the high-spin/low-spin energy difference in the low-spin iron(II) tris(2,2'-bipyridine) complex," *Chem. Phys. Chem.* **6**, 1393-1410 (2005).
- [11] Gawelda, W., et al., "Structural determination of a short-lived excited iron(II) complex by picosecond X-ray absorption spectroscopy," *Phys. Rev. Lett.* **98**, 057401 (2007).
- [12] Gawelda, W., et al., "Ultrafast nonadiabatic dynamics of Fe-II(bpy)(3) (2+) in solution," *J. Am. Chem. Soc.* **129**, 8199-8206 (2007).
- [13] Bressler, C., et al., "Femtosecond XANES study of the light-induced spin crossover dynamics in an iron(II) complex," *Science* **323**, 489-492 (2009).
- [14] Beaud, P., et al., "Spatio-temporal stability of a femtosecond hard-X-ray undulator source studied by control of coherent optical phonons," *Phys. Rev. Lett.* **99** 174801 (2007); *Phys. Rev. Lett.* **100**, 099901 (2008).
- [15] Ogasawara, H., Nordlund, D., and Nilsson, A. "Ultrafast coherent control and characterization of surface reactions using FELs," in *Proceedings of the 27th International Free Electron Laser Conference (JACoW/eConf C0508213, Stanford, California, USA, 2005)*.
- [16] Sussman, B. J., Townsend, D., Ivanov, M. Y., and Stolow, A., "Dynamic Stark control of photochemical processes," *Science* **314**, 278-281 (2006).
- [17] Winter, B. and Faubel, M., "Photoemission from liquid aqueous solutions," *Chem. Rev.* **106**, 1176-1211 (2006).
- [18] Aziz, E. F., (private communication).
- [19] Bergamaschi, A., et al., "Performance of a single photon counting microstrip detector for strip pitches down to 10 micrometer," *Nucl. Instrum. Methods A* **591**, 163-166 (2008).
- [20] David, C., (private communication).

III. Coherent Diffraction by Nanostructures

Atomic-resolution structure of biological and inorganic nanostructures with lensless imaging

- The challenges of bio-imaging
- Lensless imaging
- Protein nanocrystals and 2d-crystals
- Imaging of single biomolecules
- Space- and time-correlations in coherent scattering
- Lensless imaging of inorganic nanostructures

The high transverse coherence of the SwissFEL will allow nanostructures such as biomolecular complexes and crystal defects to be imaged at atomic resolution using the technique of lensless imaging. This diffraction technique relies on the solution of the phase problem. Furthermore, the SwissFEL's high peak brilliance and short pulse length offer solutions to the major problems in structural biology: the limited availability of high-quality crystals and the sample degradation through radiation damage. The ability to image single biomolecules with the SwissFEL would bring enormous benefit: of the more than 51'000 structures in the Protein Data Bank, less than 200 are of the difficult to crystallize but biologically vital membrane proteins. In parallel to the challenge of injecting individual nanocrystals or biomolecules into the SwissFEL beam, highly intelligent procedures for the collection and analysis of large numbers of low-statistic coherent speckle patterns must be developed. By combining lensless imaging with a suitable pump source, the SwissFEL will in addition allow the study of the dynamics of nanostructures, both organic and inorganic.

The challenges of bio-imaging

The advent of synchrotron radiation X-rays has revolutionized the imaging of biological structures, at the level of organisms, tissues, cells, sub-cellular structures, protein complexes and individual biomolecules. Typically 40% of the allocated beam time at a 3rd generation synchrotron source is used for the bio-imaging techniques phase-contrast tomography, coherent-diffraction imaging and protein crystallography. The growing popularity of *phase-contrast* methods stems from the much enhanced hard-X-ray contrast for biomaterial compared with *absorption*-based techniques, e.g., a factor 500 at a photon energy of 10 keV. Coherent diffraction imaging makes use of transverse coherence, obtained at the synchrotron by spatial filtering, to realize a spatial resolution beyond that available from focusing optics.

Synchrotron-based protein crystallography is responsible for more than 80% of the structures in the Protein Data Bank, but this represents a mere 6% of all the proteins which have been sequenced to date. A major bottleneck in structural biology today is the necessity of isolating, purifying and crystallizing sufficiently large (>10 μm^3) samples for a synchrotron-based experiment. Bio-imaging techniques based on electron microscopy and electron diffraction (see Infobox) are also growing in popularity; a short penetration depth limits their application to samples thinner than 1 μm .

By far the major factor limiting the resolution of current X-ray and electron bio-imaging techniques is radiation damage to the sensitive biological material. An undulator beamline at a 3rd generation synchrotron delivers the maximum allowable dose to a protein crystal (10^{10} photons/ μm^2) in approximately a second – higher statistics

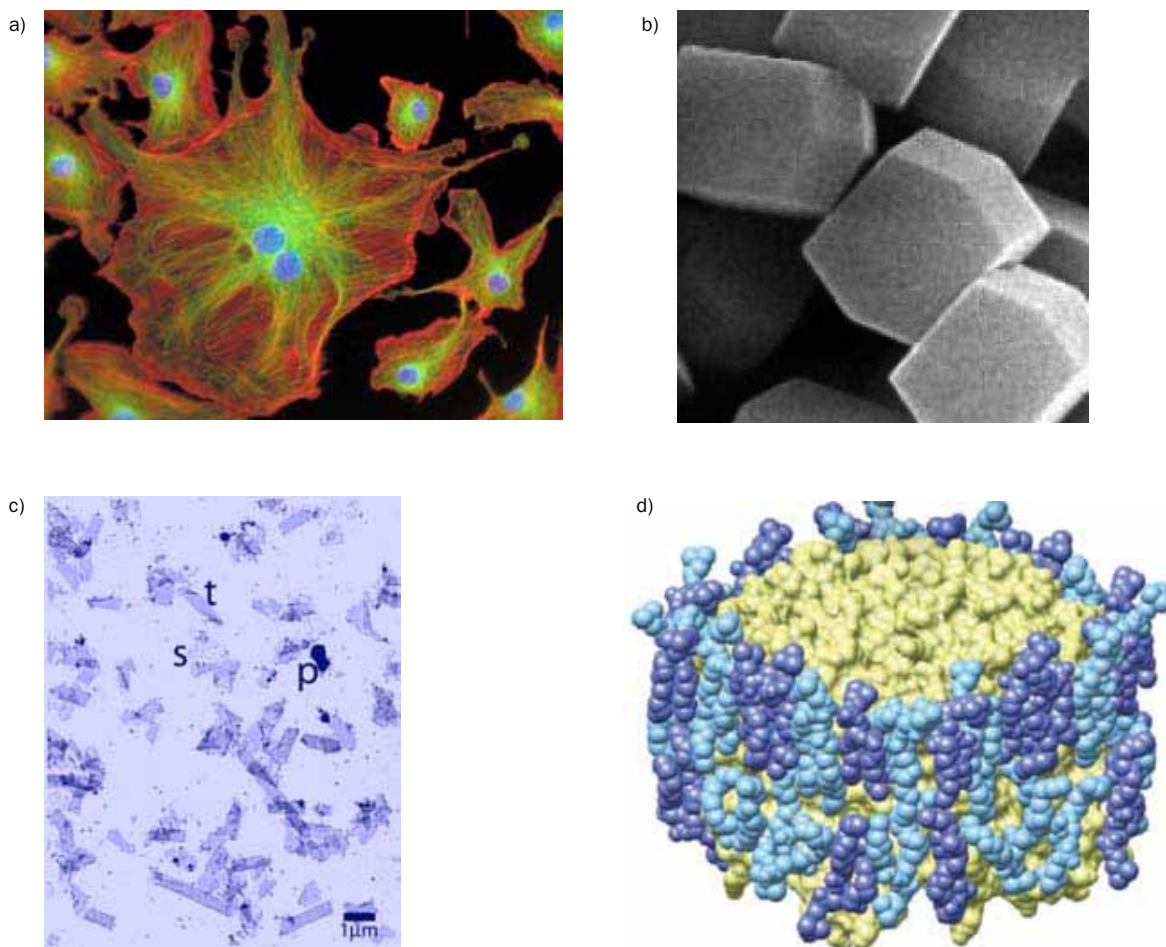


Fig. III.1. Bio-imaging challenges that the SwissFEL will meet: resolving intracellular features at nm resolution, such as the cytoskeleton (a), allowing the use of very small 3d-nanocrystals (b) or of 2d-membrane protein crystals (c) to avoid the crystal growth problem in protein crystallography, and sequentially injecting into the beam individual biomolecules (d), for high-resolution structure determination.

Transverse coherence of the SwissFEL beam

The mutual coherence function of an electromagnetic wave is defined as [14]:

$$\Gamma_{12}(\tau) = \langle \vec{E}(\vec{r}_1, t) \cdot \vec{E}(\vec{r}_2, t + \tau) \rangle$$

where it is assumed that the electric field is a stationary random function and that \vec{r}_1 and \vec{r}_2 lie in the same plane, transverse to the propagation direction. The “degree of coherence”, or the “first-order correlation function”, is then:

$$\gamma_{12}(\tau) = \frac{\Gamma_{12}(\tau)}{\sqrt{\Gamma_{11}(0)\Gamma_{22}(0)}}$$

To assess the spatial (or transverse) coherence, we assume sufficient monochromaticity that the time-delay from the path difference $\vec{r}_1 - \vec{r}_2$ is less than the longitudinal coherence time $\tau_{long} = \lambda^2/2c\Delta\lambda$, and we set $\vec{r}_1 \equiv \vec{r}_0$, on the beam axis. A quality indicator is then the transverse coherence factor $\gamma_{02}(0)$. Of particular interest to the experimenter is the coherence area, which is a measure of the usable beam area for coherent experiments:

$$A_{coh} = \int \gamma_{02}(0) dA_2$$

Numerical simulations for the SwissFEL [15] have shown that at the undulator exit, $A_{coh} \approx 5 \times \pi r_0^2$, where r_0 is the electron-beam radius. This implies a high degree of transverse coherence over the entire focus spot.

The transverse SwissFEL beam shape is approximately Gaussian $I(r) \propto \exp(-r^2/2r_0^2)$, with a transverse phase-space product $r_0\theta = \lambda\pi/4\pi$, where simulations [15, 16] yield an effective Hermite mode number $n \approx 1.5$. Propagation of a Gaussian mode proceeds as shown in Figure III.i1, with

$$r(z) = r_0 \sqrt{1 + \left(\frac{z}{z_{Ray}}\right)^2}$$

where the “Rayleigh length” is $z_{Ray} = 4\pi n r_0^2 / \lambda$. For the (rms) SwissFEL electron beam radius of 22 μm ; at a wavelength of 0.1 nm, this yields a $\theta = 0.9 \mu\text{rad}$ divergence angle.

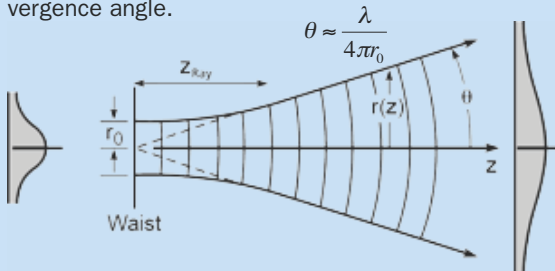


Fig. III.i1. The propagation of a Gaussian beam.

Longitudinal coherence and XFEL seeding

In contrast to the excellent transverse coherence, the longitudinal coherence of an XFEL operating in a SASE (self-amplifying spontaneous emission) mode is quite poor. Referring to the first-order correlation function, defined at left, the longitudinal coherence time is given by [1, 16]:

$$\tau_{long} = \int |\gamma_{00}(\tau)|^2 d\tau = \frac{\lambda^2}{2c\Delta\lambda}$$

A wish of many experimenters is to have Fourier-transform-limited pulses, with a minimum longitudinal phase-space product relating the pulse duration, $\Delta\tau = \tau_{long}$, and the frequency bandwidth:

$$\Delta\tau \Delta\nu = \tau_{long} \Delta\nu = \frac{1}{2}$$

The SASE process typically yields a relative bandwidth $\Delta\lambda_{SASE}/\lambda = 10^{-3}$, implying coherence times of 0.17 and 1.7 fs, at 0.1 nm and 1 nm wavelengths, respectively. The bandwidth can be reduced by the use of a monochromator, typically yielding $\Delta\lambda_{mono}/\lambda = 10^{-4}$. More attractive from the point of view of pulse-to-pulse stability is the option to “seed” the XFEL beam (see, for example, [17]). This is done by introducing narrowband radiation along the path of the electrons, causing them to micro-bunch and radiate at a pre-determined wavelength. A simulation comparing SASE pulses with those from seeding is shown in Figure III.i2 [15].

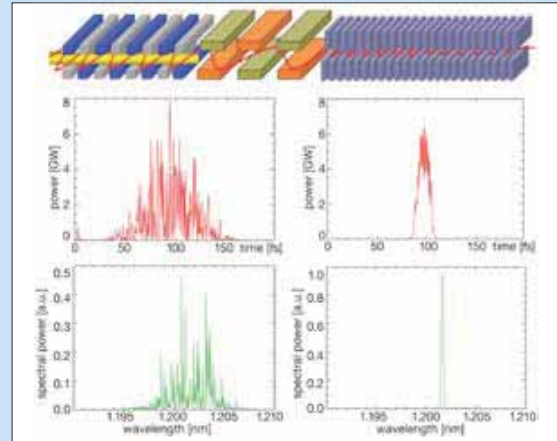


Fig. III.i2. A schematic seeding arrangement, and numerical simulations [17] of SASE (left) and seeded (right) SwissFEL pulses and spectra, at a center wavelength of approximately 1.2 nm. This seeding arrangement is based on the introduction of a 5 nJ pulse of 6 nm radiation (yellow bar in the schematic at the top), generated, e.g., by an IR-laser scattering on a gas target, in the “high-harmonic generation” (HHG) process. Using multiple undulators, the pre-bunched electron beam is then made to emit coherently at the 5th harmonic. This multi-stage process is called high-gain harmonic generation (HG) [18].

requires introducing fresh crystals. For imaging non-reproducible objects, the difficulty is more fundamental: at a resolution of better than 1 nm, the required imaging dose exceeds the maximum allowable dose by more than 5 orders of magnitude!

The SwissFEL provides solutions to all of these problems: The fine focus ($100 \times 100 \text{ nm}^2$) and enormous peak brilliance will allow the use of tiny samples: nano-crystals, 2d-crystals and perhaps even single biomolecules (see Fig. III.1). The inherent 100% transverse coherence eliminates the filtering requirement in diffractive imaging. And, in the low-charge / high electron-bunch-compression operation mode, the extremely short duration of the SwissFEL X-ray pulses will eliminate the problem of radiation damage by allowing data collection to be performed before the sample undergoes destructive Coulomb explosion. Finally, the 100–400 Hz repetition rate of the SwissFEL is ideally suited to the frame rate of modern 2d-pixel detectors (see Infobox).

Lensless imaging

XFEL coherence and coherent scattering

Due to its nearly monomode operation, the SwissFEL will produce radiation with a high degree of transverse coherence (see Infobox). To a good approximation, the radiation propagates as a Gaussian beam, with a divergence angle given by $\theta \sim \lambda/4\pi r_0 \sim 1 \text{ } \mu\text{rad}$, for a wavelength $\lambda = 1 \text{ } \text{Å}$ and an rms source (electron beam) radius $r_0 \approx 20 \text{ } \mu\text{m}$. The longitudinal coherence is poor, however, in particular for the unfiltered SASE radiation; the corresponding longitudinal coherence length $\xi_{\text{long}} = \lambda^2/2\Delta\lambda$ is of the order of 50 nm, corresponding to a bandwidth $\Delta\lambda/\lambda = 10^{-3}$. The longitudinal coherence can be increased by seeding of the SwissFEL electron beam or by filtering the photon beam with a monochromator. As discussed in [1], for thin samples and reasonably small scattering angles, good transverse coherence is sufficient to produce speckle, and hence to permit lensless imaging. A comparison of the scattering of incoherent and coherent radiation by a collection of small objects is shown in Figure III.2. The Debye-Scherrer rings of the incoherent scattering pattern contain little information – basically

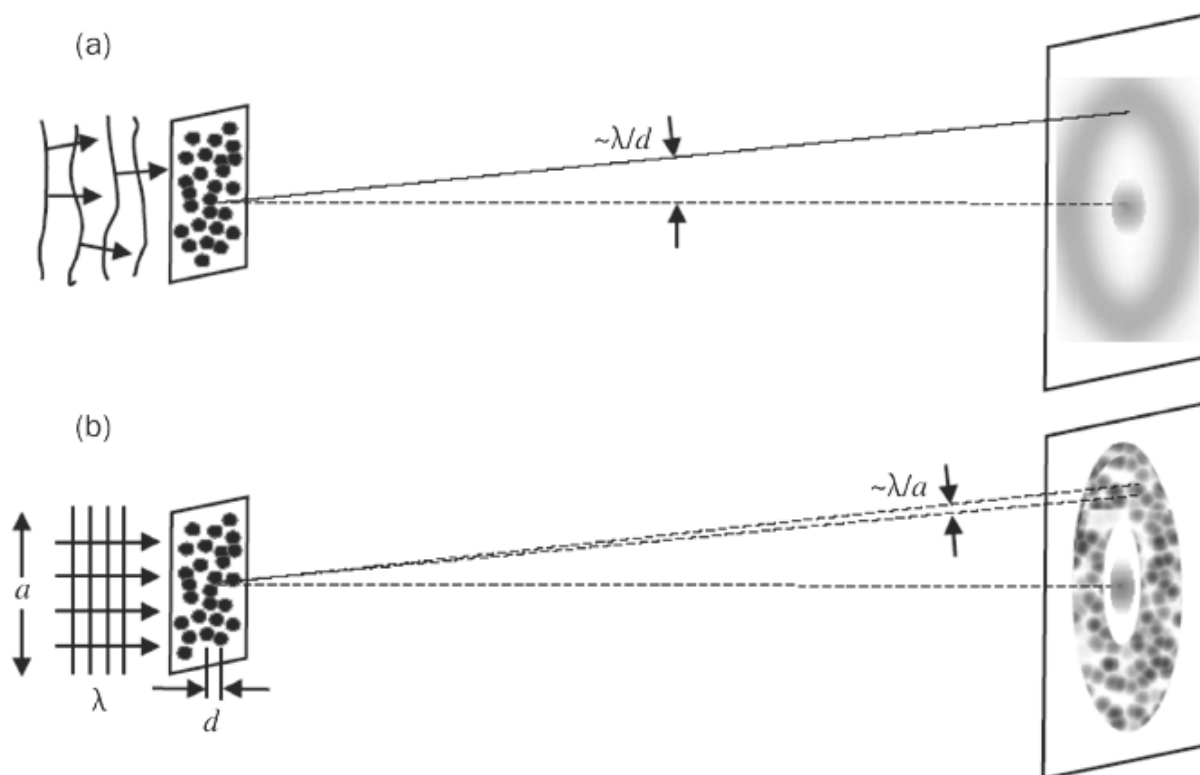


Fig. III.2. Whereas the scattering of incoherent radiation, e.g. from a synchrotron, yields only the average spacing d of a collection of scatterers (a), the scattering of coherent radiation (with beam diameter a) from the SwissFEL produces a rich speckle pattern (b), which can be inverted to obtain the exact distribution of scatterers (from [1]).

the average separation d of the scattering objects. In contrast, coherent radiation incident in a beam spot with diameter a yields a rich pattern of interference speckles, each with an angular extent which is inversely proportional to a . Only the intensity of the radiation in the speckles is measured in a detector; the phase of the scattered radiation is lost. In order to obtain from the scattering pattern the distribution of scatterers in real space (projected onto a plane perpendicular to the incoming beam direction), one needs to perform an inverse Fourier transform, but first one needs to recover the lost phase information. This is the famous phase problem in scattering and crystallography, and its solution provides the form of the object without the requirement of diffraction-limited X-ray lenses.

Several approaches to phase retrieval have been developed. One is to allow the scattered radiation to interfere with an unscattered reference beam, thus performing holography, as described for magnetic scattering in Chapter I. Other methods involve performing oversampling and the iterative application of constraints [1]. The coherent scattering pattern from an infinite array of identical objects with period d consists of a series of isolated (Bragg) peaks (representing terms in a Fourier series describing the array) at scattering angles satisfying $\sin \theta = q\lambda/4\pi$, where the scattering vector q can take the values $q_n = 2\pi n/d$ ($n = 0, \pm 1, \pm 2, \pm 3, \dots$). The scattering thus samples the array at the scattering vector interval $\Delta q = 2\pi/d$, and only a single measured quantity, the scattered peak intensity, is available for each Fourier component. A finer sampling of the scattering pattern of the periodic array is not possible, since the scattering between Bragg peaks is zero. A single object of spatial extent a will, on the other hand, produce a continuous coherent scattering (speckle) pattern, which can in principle be sampled at an arbitrarily large number of scattering vectors. This oversampling can yield the additional information required to recover the scattering phase.

The phase-retrieval process is generally performed in an iterative manner, by making an initial assumption for the phases and repeatedly Fourier and inverse-Fourier transforming between the real and scattering (reciprocal) space representations. Constraints are applied in each iteration cycle. In reciprocal space, it is required that the calculated scattering intensity agree with the measurements. In addition, one or more real-space constraints are applied: such as that scattering from the sample is zero outside a delimiting boundary, that the sample's electron density is non-negative, or that the scattering is concentrated in isolated "atoms". A further method

of performing phase-retrieval, the ptychographic method, is described later.

The 1-dimensional case discussed above can easily be extended to a 2-dimensional projection, and if a series of scattering measurements can be recorded for different orientations of the sample, to a 3-d diffraction pattern.

Resolution limits in bio-imaging

Of particular interest in nanoscale imaging are biological objects, down to the level of the atomic structure of macromolecules. The principal limit to the resolution achievable with X-ray or electron scattering by bio-materials is imposed by radiation damage. (The investigation of biological samples with electron microscopy and diffraction is treated in an Infobox.) Howells et al. [2] have investigated both theoretically and experimentally the resolution limits for imaging non-periodic (i.e., non-crystalline) bio-materials (see Fig. III.3). Making use of the classical electron radius

$$r_e = \frac{1}{4\pi\epsilon_0} \frac{e^2}{m_e c^2} = 2.818 \times 10^{-15} \text{ m}$$

and the complex electron density

$$\rho_e = \frac{2\pi(\delta + i\beta)}{\lambda^2 r_e},$$

(related to the complex index of refraction of the scatterer, $n = 1 - \delta - i\beta$), the number of incident X-rays per unit area required to scatter P photons into a detector from a 3-dimensional voxel of the sample with dimensions ($d \times d \times d$) is given by

$$N_0 = \frac{P}{r_e^2 \lambda^2 |\rho_e|^2 d^4}$$

This corresponds to a dose, measured in Grays (with 1 Gy = 1 J/kg of deposited energy) of

$$D = \frac{\mu h\nu}{\rho_m} N_0,$$

where ρ_m is the mass density and μ is the inverse absorption length. The Rose criterion for the detection of features in the presence of background noise requires that the signal exceed the rms noise level by a factor of 5. Assuming Poisson shot noise, this criterion requires $P = 25$. The solid and dashed lines in the plot show the dose required to achieve a particular resolution d for a bio-material with composition $\text{H}_{50}\text{C}_{30}\text{N}_9\text{O}_{10}\text{S}_1$ and density $\rho_m = 1.35 \text{ g/cm}^3$, against a water background, for X-ray energies $h\nu$ of 1 and 10 keV, respectively. Note that the required dose depends on the resolution as d^{-4} .

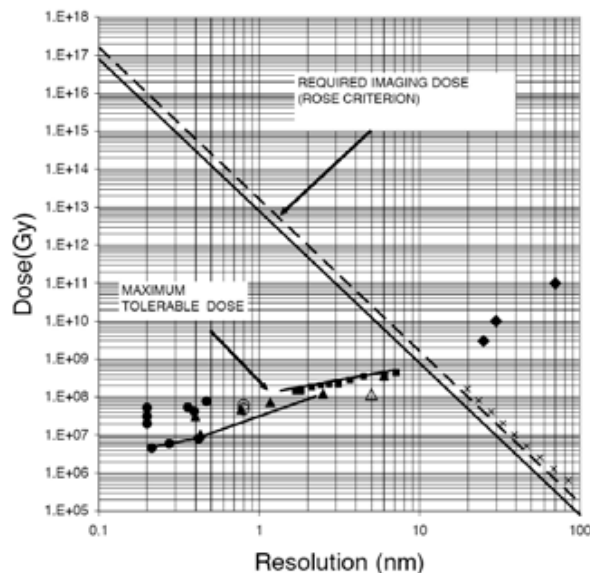


Fig. III.3. The required and maximum tolerable doses for imaging a bio-material sample ($\text{H}_{50}\text{C}_{30}\text{N}_9\text{O}_{10}\text{S}_1$) against a background of water [2]. The water background is accounted for by setting $\rho_e = \rho_e(\text{sample}) - \rho_e(\text{water})$ and using $\mu(\text{water})$ and $\rho_m(\text{water})$. The required dose is calculated according to the Rose criterion, as described in the text, for 1 (solid line) and 10 keV (dashed line) X-rays. Measurements of the maximum tolerable dose have been compiled from experiment for various X-ray and electron scattering techniques.

Also shown in the plot are the empirical results of analyses of electron and X-ray scattering experiments, giving the maximum allowable dose at resolution d . When translated to integrated X-ray flux, these points lie close to the 10^{10} photons/ μm^2 damage limit often quoted for bio-materials studied at atomic resolution. (It should be noted that small samples, such as nano- and 2d-crystals or single molecules, may show a significantly higher damage limit, due to the immediate escape from the sample of primary photoelectrons.) Of particular interest is the point of intersection of required and tolerable dose, corresponding to 10^9 Gy and a resolution of $d = 10$ nm. This is the approximate limit for imaging a single non-periodic sample at a synchrotron. Better resolution requires exposing many equivalent copies of the sample or taking advantage of coherent scattering from the large number of identical unit cells in a crystalline sample. Consider the following cases: a) imaging a bio-material in a water background with 1 keV X-rays to a resolution of 2 nm, and b) imaging a pure bio-material sample with 10 keV X-rays to 0.2 nm. Simple application of the Rose criterion above predicts the required integrated X-ray flux into a 100×100 nm² spot for a) and b) to be 10^{11} and 7×10^{15} photons, respectively. The former corresponds

Electron microscopy and diffraction

Alternatives to the SwissFEL for performing structural determinations on individual biomolecules and 2d-bio-crystals are the techniques of electron tomography and electron diffraction. Electrons (100-500 keV) are scattered by matter more strongly than are hard X-rays, hence requiring the use of thin samples ($< 1 \mu\text{m}$). In a large sample, the amount of energy deposited by inelastic scattering events per useful elastic scattering event is 1000 times less for electrons than for X-rays [19]. In sub- μm samples, this factor is less, due to the escape of photoelectrons. In order to preserve samples for long enough in the electron beam to collect useful statistics, it is necessary to flash cool the sample, generally by plunging it into liquid ethane.

Electron tomography [20] uses electron microscope images of many identical, individually-measured molecules, in their natural environment, taken at various tilt angles, to reconstruct the 3d-structure. The problems involved in data analysis are similar to those that will be encountered with single-molecule lensless imaging at the SwissFEL. The 3d-resolution presently achievable with electron tomography is 1–2 nm, limited by radiation damage and the change of the beam focus with sample tilt for regions slightly displaced from the tilt axis.

Electron diffraction [21] can be performed on cryo-cooled crystalline samples which are sufficiently thin. An attractive application is to 2d-membrane crystals, for which structural determinations have been performed down to 0.2 nm resolution [22]. Time-resolved electron diffraction measurements of bio-molecular structure will require improvements in transverse coherence and successfully dealing with space-charge effects [23].

Besides the elimination of radiation damage by using short SwissFEL pulses, principal advantages of X-ray imaging over electron techniques are the relaxed demands on sample thickness and accurate sample tilting. A further point is related to the much stronger scattering of electrons than X-rays: whereas a simple kinematical approach, which neglects multiple scattering, is justified in interpreting X-ray scattering, much more complicated dynamical theories must be used for the electron techniques.

Particle injection and laser orientation

Coherent diffraction by single biomolecules will require that they be individually introduced, in vacuum, into the SwissFEL beam. Furthermore, the analysis of low-statistics scattering images will be greatly simplified if a preferred molecular orientation can be achieved. Several groups are working on these problems.

Figure III.i3 a shows a closeup of the aerojet droplet source, developed by Shapiro et al. [24]. An inner capillary, with 50 μm inside diameter, carries the pressurized (10 bar) particle solution, and the outer capillary contains CO_2 at 1 bar, which tends to focus the particle stream. The jet velocity is 10 m/s, and the Rayleigh instability causes breakup of the stream, which can be triggered using a piezoelectric actuator (Fig. III.i3 b). By choosing the distance from the nozzle, one can control the amount of unevaporated mother liquid surrounding the particles.

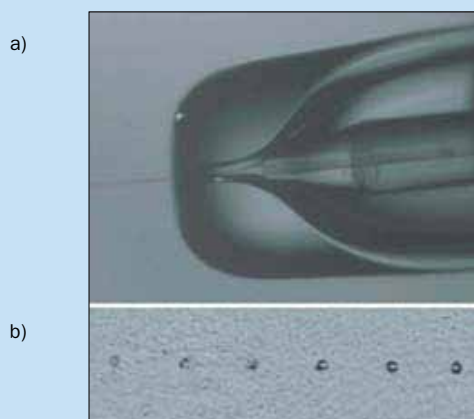


Fig. III.i3 The double-capillary aerosol droplet source (a) of Shapiro et al. [24] produces evenly-timed droplets, when piezoelectrically triggered (b).

Figure III.i4 shows a scenario for using polarized laser light to perform two-axis orientation of anisotropic protein molecules, such as the tobacco mosaic virus (TMV) [25].

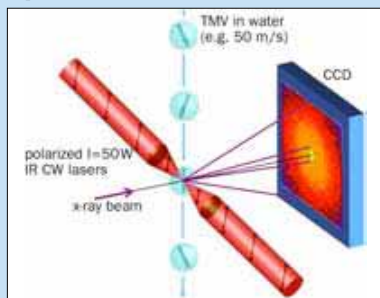


Fig. III.i4. The proposed orientation of strongly anisotropic protein molecules by polarized laser beams [26].

to a single SwissFEL shot, indicating the real possibility of single-shot (projection) imaging of sub-cellular organelles at nm-scale resolution. The latter integrated flux, corresponding to 70'000 shots, suggests that individual biomolecules could be lensless-imaged to 0.2 nm resolution within several minutes of measuring time. But this is under the assumption that radiation damage can somehow be avoided, and, for the individual molecules, that the scattering statistics can be accumulated (see below).

Protein nanocrystals and 2d-crystals

With its extremely high peak flux and small focus spot, the SwissFEL will allow coherent diffraction measurements on 3d-nanocrystals of protein, which are individually injected into the X-ray beam (see Infobox). The growth of protein crystals is a complex and poorly understood process, and different molecular systems show different behaviors. In general, however, as a crystal grows, it tends to accumulate defects such as stacking faults. These defects often limit the maximum size of good-quality crystals. It is believed that many interesting protein species may only form good crystals with sub- μm dimensions (see Fig. III.4).

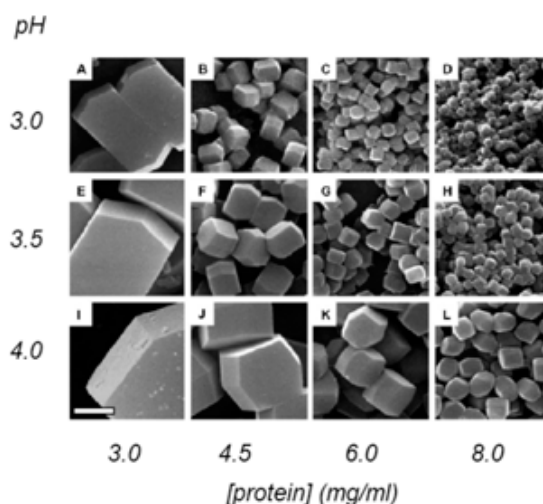


Fig. III.4. Examples of micrometer and sub-micrometer crystals of the protein lysozyme [3]. The scale bar at bottom left is 2 μm .

Scattering from a crystal has the great advantage over a single-molecule experiment that a large number of identically-oriented unit cells contribute coherently to the scattering signal. In a perfect infinite crystal, this leads to sharp Bragg reflections corresponding to particular

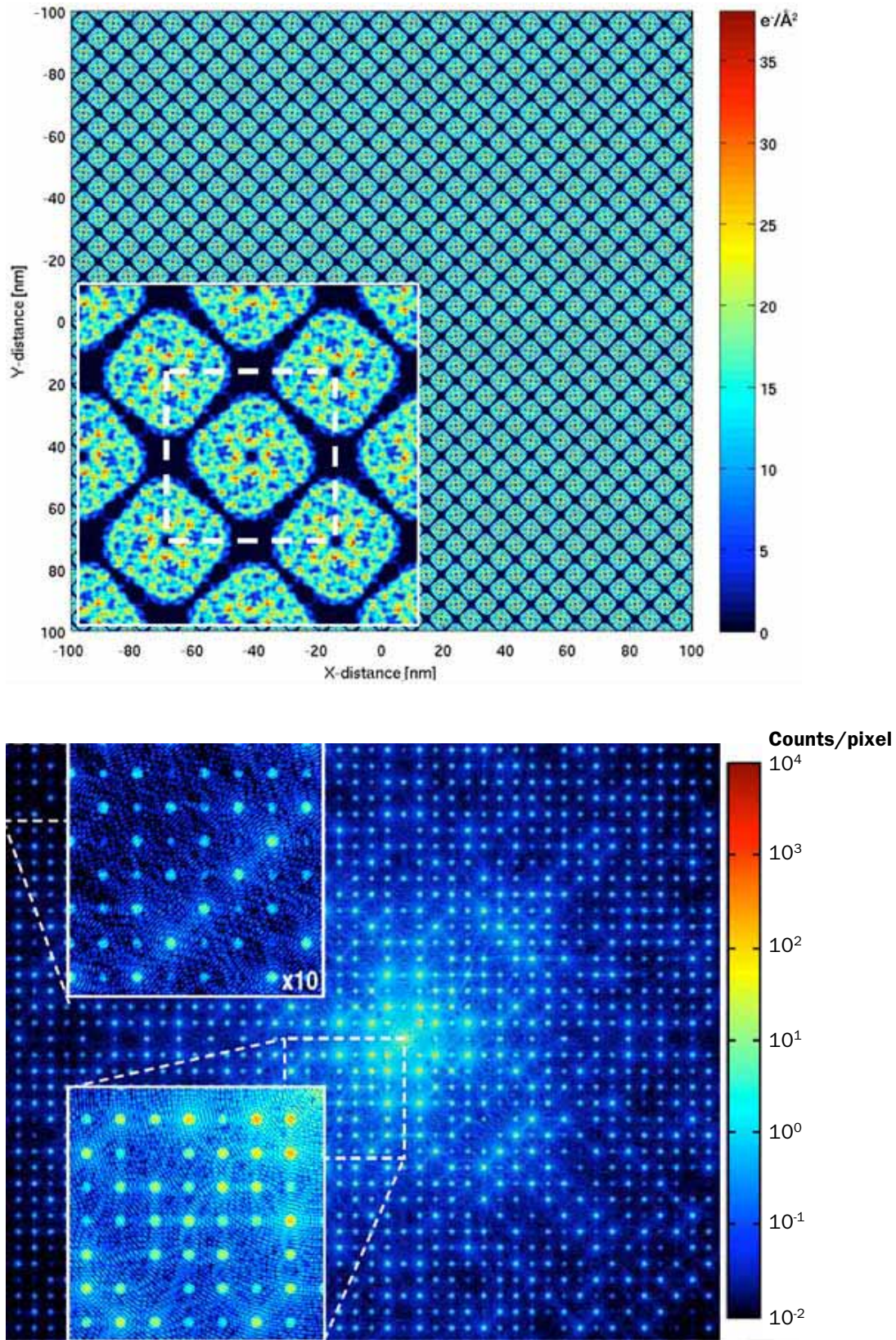


Fig. III.5. Simulated ptychographic diffraction [4] of a 2d-crystal of the membrane protein aquaporin-1. The projected electron density (above) is sampled with an XFEL pulse (10^{12} photons at 12 keV, focused to a spot 100 nm in diameter), producing the simulated scattering pattern shown below. Note the coherent diffraction features between the Bragg peaks (insets).

The biological importance of membrane proteins

In the living cell, membrane proteins are situated within the cell membrane, a double lipid layer which separates the cytoplasm from the cell exterior (see Fig. III.i5). In the course of the Human Genome Project, it was discovered that genes encoding membrane proteins make up approximately 30% of the genome. These proteins regulate the cellular homeostasis, act as receptors, transporters and channels, and are responsible for cell development, intercell interactions, nerve transmission, muscle contraction, signaling and programmed cell death. Mutations in membrane proteins cause a vast variety of inherited or acquired diseases, including cystic fibrosis, drug resistance, diabetes, Alzheimer's, kidney and digestive diseases, hypertension and heart failure [27]. It has been predicted [28] that up to 70% of all future drugs will target membrane proteins.

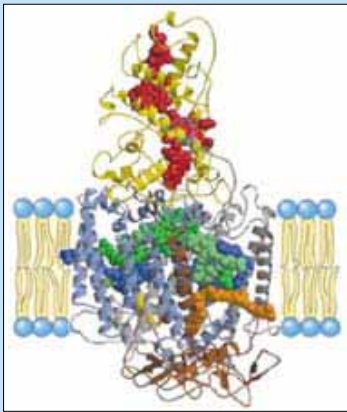


Fig. III.i5. A schematic view of the photosynthetic reaction center, one of the relatively few membrane proteins whose high-resolution structure could to date be determined using X-ray crystallography [29].

Intelligent drug design requires detailed knowledge of the relevant biochemical system, preferably in the form of a 3d-molecular structure at atomic resolution. Conventional synchrotron-based protein crystallography can provide such information, but only if sufficiently large ($>10 \mu\text{m}^3$) 3d-crystals can be grown, and in sufficient number. Because of their 2d-habitat in the cell, membrane proteins are notoriously difficult to crystallize in three dimensions. Therefore, the two novel possibilities for protein structure determination presented by the SwissFEL, namely 2d X-ray crystallography in the ptychography mode, and single-molecule diffraction, are of enormous importance for pharmaceutical development.

scattering vectors, with the peak intensity in each Bragg peak proportional to the square of the number of unit cells in the crystal. As mentioned earlier, since there is no scattering intensity between the peaks, oversampling for an infinite crystal is not possible, thus complicating the phase-retrieval process. The use of nanocrystals, for which (weak) continuous coherent scattering features connect the Bragg peaks, provides additional information useful for phasing.

An innovative method, developed at PSI, of using coherent diffraction features to solve the phase problem is ptychographic diffraction (from the Greek for “folding”) [4]. In ptychography, a small-spot coherent X-ray beam is scanned across a large, non-periodic sample, and a series of coherent scattering patterns is collected. The speckle size is determined by the inverse of the spot size rather than by the sample dimensions. Overlapping the scanned spots allows one to incorporate the speckles into the phase-retrieval process, in spite of the large sample size. By this method, the complex transmission function of a region of interest within an extended sample can be uniquely reconstructed, along with the detailed illumination function [5]. In an extension of ptychography to 2d-crystal diffraction with the SwissFEL, a large (i.e., several μm) 2d-crystal is illuminated at randomly chosen positions with the tightly-focused (100 nm) coherent XFEL beam. The resulting scattering is a convolution of crystalline Bragg peaks and finite-aperture coherent scattering features (see Fig. III.5). Each exposure represents a different alignment between the periodic lattice and the illumination function describing the spot, and although it locally destroys the sample, successive exposures from undamaged regions of the sample provide partially-redundant information. Kewish et al. have demonstrated that this multiple exposure method aids in solving the phase problem and hence facilitates the recovery of the projected high-resolution structure of a membrane protein. By repeated scans at different tilt angles of the 2d-crystal, it will be possible to obtain the 3d-protein structure.

Imaging of single biomolecules

A single shot from the SwissFEL, with 10^{11} photons focused to $100 \times 100 \text{ nm}^2$ ($= 10^{13}$ photons/ μm^2), corresponds to a bio-material dose of 8×10^9 Gray, i.e., approximately 3 orders of magnitude above the damage threshold. Each shot will therefore require a fresh biomolecule, and since these will have random orientations, the scattering patterns cannot be simply accumulated (see Fig. III.6).

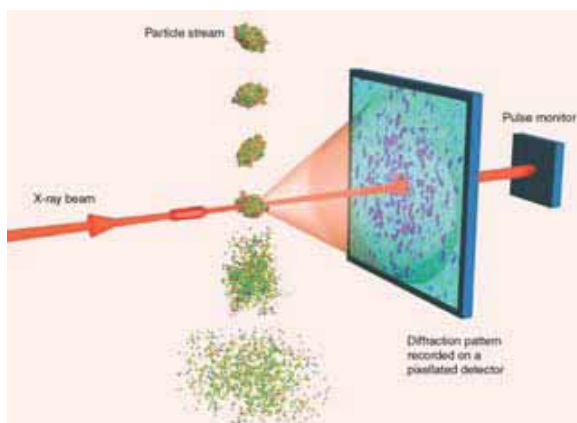


Fig. III.6. A schematic representation of a lensless imaging experiment on a single biomolecule [6]. The intention is to collect sufficient scattered photons before Coulomb explosion destroys the molecule.

How severe is the damage to a biomolecule from a single SwissFEL shot? The irradiation process has been simulated [7] for a lysozyme protein molecule exposed to an XFEL pulse of 3×10^{12} photons with 12 keV energy and focused to a 100 nm diameter spot, with various pulse durations (e.g., see Fig. III.7). The explosion of the molecule begins with primary photoionization (photoelectric and Compton effects), followed by secondary (Auger) ionization. Approximately one in five of these electrons will undergo inelastic scattering, removing an additional outer shell electron; the XFEL pulse causes more than one ionization event per non-hydrogen atom. The resulting positive ions react to the large net positive charge of the molecule and move outward, led by light hydrogen ions and highly-ionized sulphur. If the XFEL pulse is shorter than approximately 20 fs, the analysis of Neutze et al., supports the view that the ionization and ionic movement incurred during the pulse represent a tolerable perturbation for a structural determination. With innovations in low-charge operation and high electron bunch compression, the SwissFEL will be able to produce such pulses.

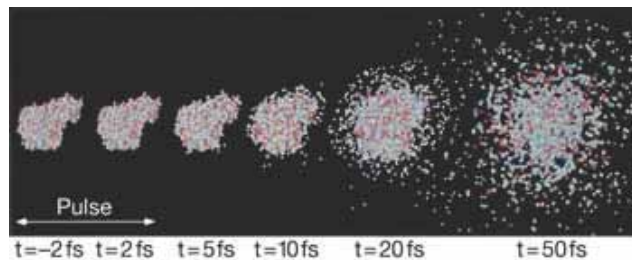


Fig. III.7. The simulated Coulomb explosion [7] of a lysozyme protein molecule exposed to a 12 keV XFEL pulse with 3×10^{12} photons focused to a 100 nm diameter spot, and with a FWHM duration of 2 fs.

Individual biomolecules are to be successively introduced into the XFEL beam by a spraying technique, presumably each with a different orientation (see Infobox). Will a sufficient number of scattered photons be detected in a single shot to determine the orientation, such that the data can be accumulated in a 3-d reciprocal space representation? This question has been investigated by simulating the scattering of a single XFEL pulse by small, medium and large biomolecules [8] (see Fig. III.8).

For the ferritin complex, no more than 0.01 photons per pixel can be expected in the interesting region of intermediate scattering vector. Can useful structural information be extracted from such sparse data? The answer to this question by Fung et al. [9] is a qualified “yes”. Instead of attempting to determine the molecular orientation from a single exposure, these authors propose a method based on the correlations of a large ensemble of scattering patterns. They define p -space, with a dimension p equal to the number of detector pixels, perhaps 10^6 . Each measured scattering pattern corresponds to a p -dimensional vector in this space – with coordinates given by the photon count in each pixel (see Fig. III.9). The authors then ask the question: as the scattering molecule is rotated in 3d-space, how does the corresponding p -vector move? Their answer: it will move on a subset of p -space defined by a 3d-manifold, corresponding to the three (Eulerian) orientation angles in 3d-space. Such an embedded-manifold can be described mathematically by a set of coefficients. Using simulated scattering data from a small protein, the authors demonstrate that these coefficients can be reliably determined with statistics corresponding to 0.01 photons/pixel, effectively solving the classification problem for molecular orientations and hence allowing for data from successive XFEL shots to be accumulated. Although it should be noted that important effects due to back-

ground scattering and unknown illumination functions have yet to be considered, this approach may potentially even treat the cases of multiple molecular configurations (for which several 3d-manifolds will exist in p -space) and perhaps even *continuous* variation between configurations (for which manifolds must be determined with more than 3 dimensions).

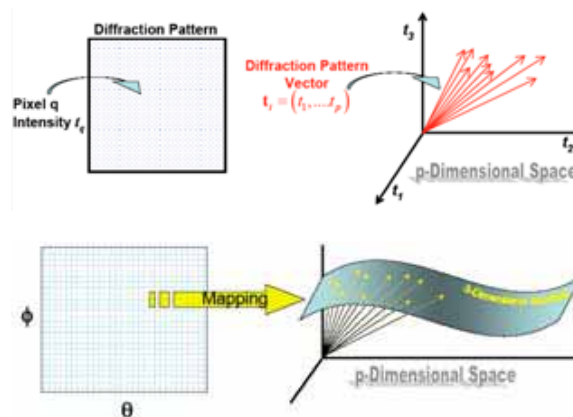
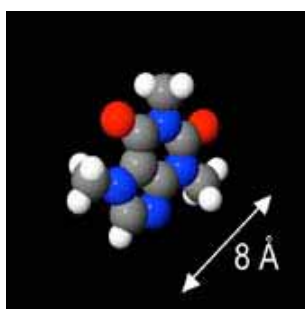
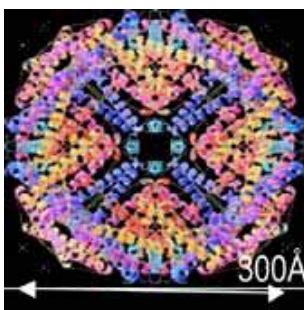
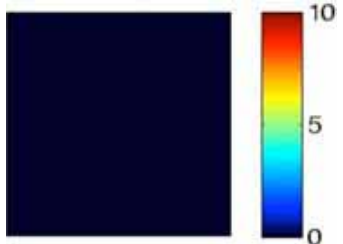
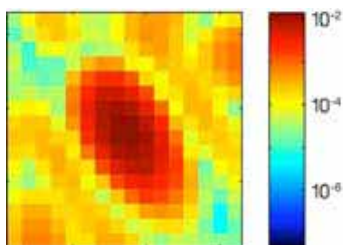


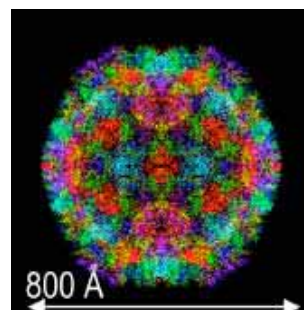
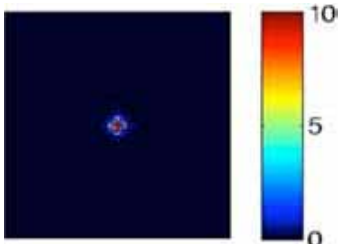
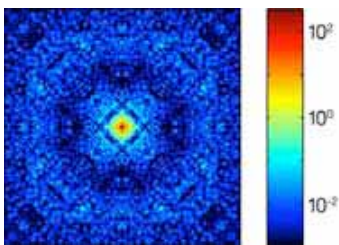
Fig. III.9. A method for classifying molecular orientations from an ensemble of sparse scattering patterns [9], in which the possible patterns lie on a 3d-manifold, corresponding to the 3 orientation angles, in a p -dimensional space, where $p \approx 10^6$ is the number of detector pixels.



Caffeine
24 atoms,
102 electrons



Ferritin 1R03,
1'683 atoms,
16'789 electrons



Rice Dwarf Virus 1Uf02,
58'130 atoms,
383'176 electrons

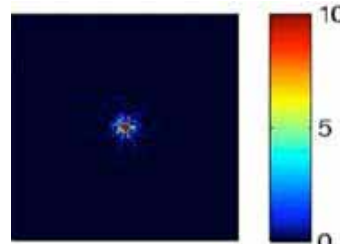
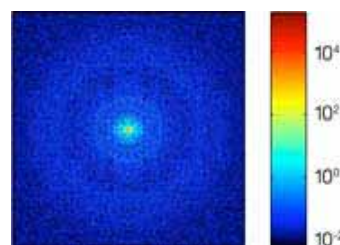


Fig. III.8. The predicted scattering, by small, medium and large biomolecules, of an XFEL pulse with 10^{12} photons of energy 12 keV and focused to a $100 \times 100 \text{ nm}^2$ spot [8]. The color scale of the scattering patterns (logarithmic above and linear below) gives the predicted number of scattered photons per optimized detector pixel. This pixel size has been scaled with the inverse molecule size to correspond to a single coherent speckle.

Space- and time-correlations in coherent scattering

The pulsed time-structure of the SwissFEL beam will permit the elegant realization of an alternative scattering method which uses space- and time-correlations to determine the anisotropic structure of one or more objects undergoing tumbling motion in solution. Kam has computed [10] the X-ray scattering from a prolate ellipsoid undergoing random rotations (see Fig. III.10). Whereas the time-averaged scattering $\langle S(\kappa) \rangle$ shows an isotropic pattern as a function of the D_1 detector position ($|\kappa| = |\kappa_1|$, φ), the correlated time-averaged instantaneous product $\langle S(\kappa_1)S(\kappa_2) \rangle$ of the counting rates into D_1 and D_2 , reveals the object's anisotropy, as a function of, for example, $|\kappa| = |\kappa_1| = |\kappa_2|$ and $\psi = \text{angle}(\kappa_1, \kappa_2)$. In his paper, Kam explains how the method can be applied to increasing numbers of identical but randomly rotating objects and how a refinement can be performed of more complex shapes, in terms of an expansion in spherical harmonics.

The pulsed time structure of the SwissFEL radiation brings an obvious advantage to the Kam method: since the pulse length is much shorter than a tumbling period, a 2d-scattering pattern represents an instantaneous measurement. It is thus possible to correlate, at the same time, the counts in any detector pixel with those in any other pixel. In this way, far more correlated information is available for the structure analysis.

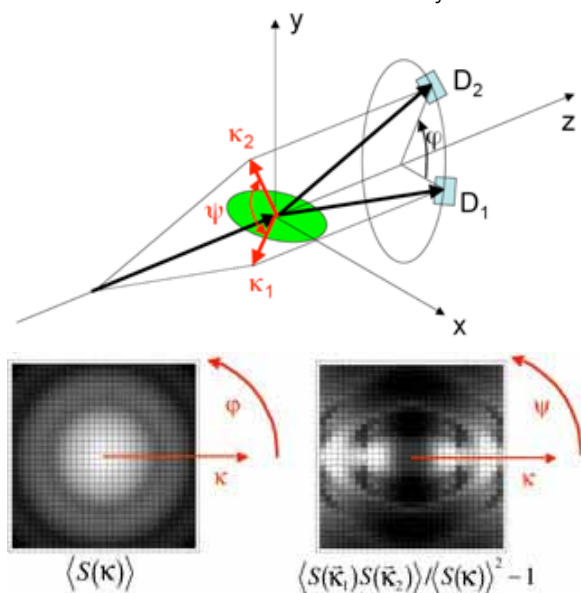


Fig. III.10. An example of the (proposed) Kam experiment [10]: One or more tumbling ellipsoids scatter X-rays into the point detectors D_1 and D_2 . Due to the isotropic rotation, the time-averaged scattering $\langle S(\kappa) \rangle$ shows an isotropic pattern in D_1 . The correlated time-averaged instantaneous product of D_1 and D_2 , however, reveals the object's anisotropy.

The PILATUS detector

A spin-off company from the Paul Scherrer Institut produces what is currently the best 2d-imaging X-ray detector in the world [30, 31]. Due to its modular design, PILATUS is available in various sizes, from 10^5 to 6×10^6 pixels (see Fig. III.i6). The modules consist of a silicon sensor, with $170 \times 170 \mu\text{m}^2$ pixels, bump-bonded to a custom-made readout chip. The detector offers noise-free, single-photon detection, a dynamic range of 20 bits, and a readout rate of 12 Hz. Advanced versions of PILATUS, with different analog gains for different detector regions and the ability to pipeline on-chip up to 500 frames, are being developed for XFEL applications [32].



Fig. III.i6. The PILATUS 6M, with 6 million pixels, has been developed at PSI and commercialized by Dectris [31], a spin-off company from PSI, for applications in synchrotron-based protein crystallography.

Lensless imaging of inorganic nanostructures

The high coherence of the SwissFEL radiation is also in high demand for the lensless imaging of inorganic nanostructures. Furthermore, the short, bright SwissFEL pulses allow ultrafast dynamic processes to be followed at the atomic level – in the form of ensemble-averaged time-dependent correlation functions. Figure III.11a shows the measured coherent X-ray diffraction pattern of a single misfit dislocation, at the interface between a Si (001) substrate and a 280 nm film of $\text{Ge}_{0.3}\text{Si}_{0.7}$, i.e., slightly above the critical film thickness for dislocation-free pseudomorphic growth [11]. The pattern is a reciprocal space map near the (202) Bragg reflection from the substrate. To collect these data, the incoming synchrotron X-ray beam was focused to a $1 \times 1 \mu\text{m}^2$ spot and scanned along the interface until an isolated dislocation was found. Numerical simulations of the diffraction pattern permitted the construction of a physical model for the local bonding arrangement at the dislocation core (see Figs. III.11b and c).

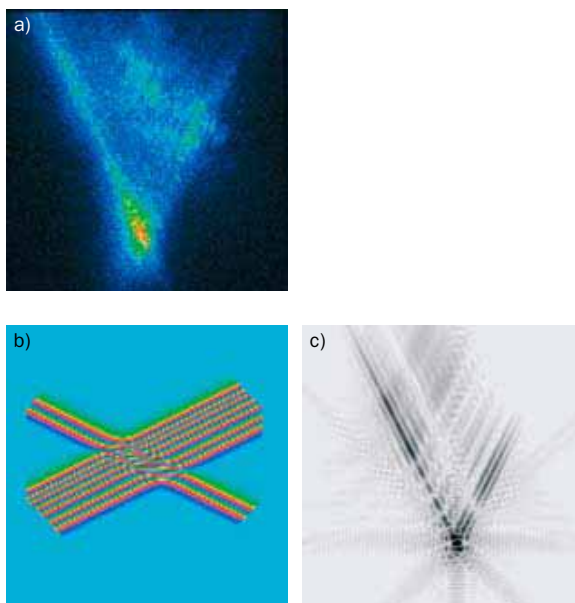


Fig. III.11. a) Coherent diffraction imaging of a single misfit dislocation at the interface between a $\text{Ge}_{0.3}\text{Si}_{0.7}$ film and the Si (001) substrate. b) A proposed physical model of the dislocation core, which yields a simulated diffraction pattern (c) in good agreement with observation [11].

An important branch of material science, which is currently inaccessible to real-time, microscopic investigation, is the generation and evolution of defect structures upon irradiation. Such defects are responsible for the production and segregation of vacancies and self-interstitials, which ultimately limit the strength of, for example, the structural components of nuclear reactors. Numerical simulations of radiation defects can be performed for limited regions of space and over limited time periods using state-of-the-art molecular dynamics (MD) calculations. An example of such a simulation, of the aftermath of a 5 keV primary knock-on event in a 12 nm grain in nanocrystalline Ni, is shown in Figure III.12 [12]. The simulation cell encompasses 15 grains, containing a total of approximately 10^6 atoms. Already 0.3 ps after the knock-on, a locally melted region has formed, from which two replacement collision sequences (RCS) emerge. As time progresses, self-interstitial atoms (SIA) move to the periphery of the cascade, either individually or as SIA clusters, away from the central vacancies, eventually becoming permanently segregated from them at the grain boundary.

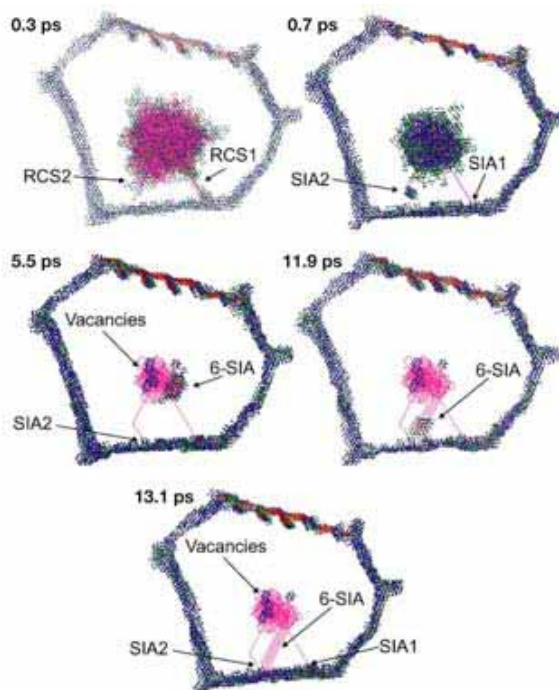


Fig. III.12. A molecular dynamics simulation [12] of a 5 keV displacement cascade in a 12 nm grain in nanocrystalline Ni, showing replacement collision sequences (RCS) and the motion of self-interstitial atoms (SIA) and a SIA cluster, away from the central melted region toward a grain boundary, which prevents any further interstitial-vacancy recombination. Only non-*fcc* atoms are shown, and the pink lines depict atomic trajectories occurring during the irradiation.

To investigate such displacement cascades at the SwissFEL, many individual irradiation events will be generated – each one with a different local geometry, and each one followed, after a particular time delay, by an X-ray probe pulse. The SwissFEL will thus deliver important physical correlations, such as the average size and density of the central vacancy cluster or the diffusion rate of multi-atom interstitial clusters.

The ability to measure spatial and temporal correlations at the atomic scale, using coherent scattering from the SwissFEL, represents a powerful tool for calibrating the accuracy of atomistic simulations in materials. The length and time scales currently accessible to MD calculations (~ 100 nm, ~ 1 ns) fit very well to the spatial and temporal scales made accessible with the SwissFEL (see Fig. III.13). An important result of the comparison of theory and measurement will be the validation of the approximations and parameter values used in MD. Of particular interest is the relation, at the shortest time and length scales, between parameterized MD calculations and *ab initio* methods, which explicitly treat the quantum-mechanical behavior of the electrons. Correct formulation at this fundamental level is of utmost importance to provide accurate input parameters for larger-scale modelling.

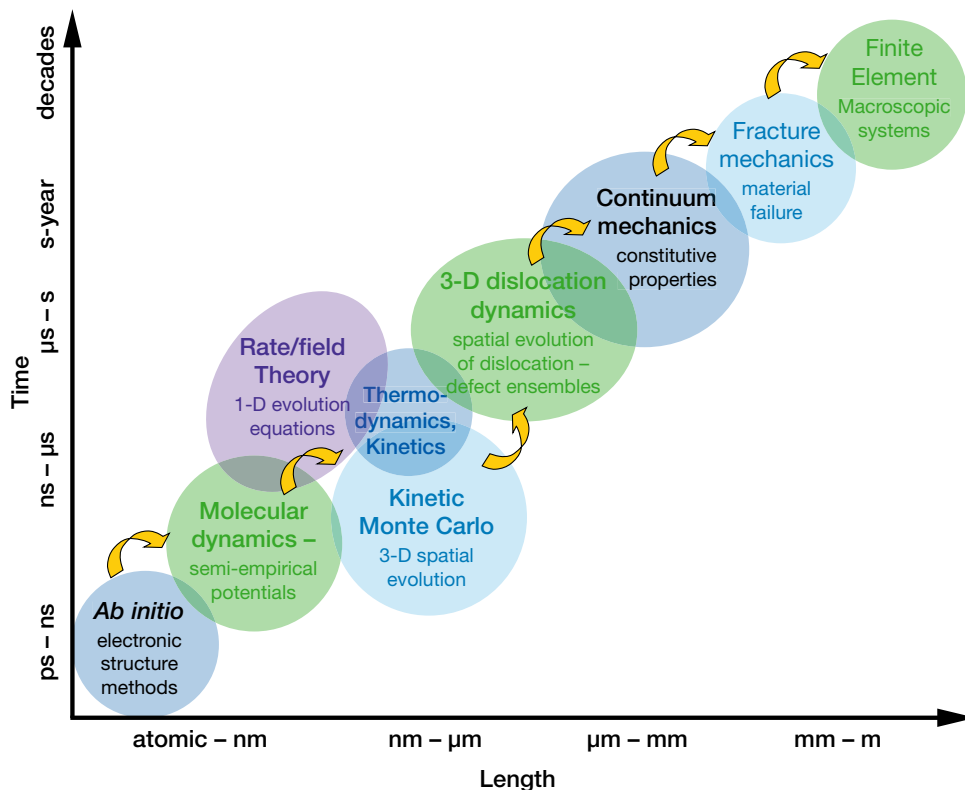


Fig. III.13. The time and length scales of materials modelling [13]. The SwissFEL will provide unique information to validate models at short time and length scales.

Summary

- *Radiation damage is currently the principal limitation to the resolution in bio-imaging experiments with X-rays and electrons. With its ultrashort pulses, the SwissFEL will avoid this limitation. The short pulse duration (20 fs) of the SwissFEL will allow scattering data to be collected before the degradation of the sample by Coulomb explosion becomes noticeable.*
- *The SwissFEL beam will have a high transverse coherence. Scattering of coherent X-rays by an object consisting of a distribution of scattering centers produces a speckle pattern, whose angular features are inversely proportional to the size of the illuminated object.*
- *An oversampled speckle pattern, in conjunction with constraints in real and/or reciprocal space, allows the recovery of the phases of the scattered rays, and hence, by Fourier transformation, of the real space distribution of scattering centers. This technique is called lensless imaging.*
- *The investigation of 3d-nanocrystals or 2d-membrane crystals should be quite straightforward, giving access to high-resolution structural information of proteins without the need of large crystals, and making optimal use of coherent scattering features.*
- *Even with the high peak intensity of the SwissFEL, a single-shot scattering image from an individual biomolecule will not provide sufficient statistics to determine the unknown molecular orientation. But by considering a large ensemble of such scattering images, sophisticated algorithms should be able to classify the orientations, such that the patterns can be coherently accumulated.*
- *The spatial and temporal correlations of SwissFEL speckle patterns will provide structural information of tumbling molecules in solution.*
- *Lensless imaging can also be performed on inorganic nanostructures, such as crystal defects. In a pump-probe arrangement, the SwissFEL will provide important statistical properties of the time development of a radiation damage cascade. Such information is necessary to improve numerical simulation methods in materials science.*

References

- [1] Van der Veen, J. F. and Pfeiffer, F., "Coherent x-ray scattering," *J. Phys.: Condens. Matter* **16**, 5003-5030 (2004).
- [2] Howells, M. R., et al., "An assessment of the resolution limitation due to radiation-damage in X-ray diffraction microscopy," *J. Electron Spectrosc. Rel. Phenom.* **170**, 4-12 (2009).
- [3] Falkner, J. C., et al., "Generation of size-controlled, submicrometer protein crystals," *Chem. Mater.* **17**, 2679-2686 (2005).
- [4] Kewish, C. M., Thibault, P., Bunk, O., and Pfeiffer, F., "Potential for two-dimensional crystallography of membrane proteins at future X-ray free electron laser sources," *Proc. Natl. Acad. Sci. USA*, (2009) in press.
- [5] Thibault, P., et al., "High-resolution scanning X-ray diffraction microscopy," *Science* **321**, 379-382 (2008).
- [6] Gaffney, K. J., and Chapman, H. N., "Imaging atomic structure and dynamics with ultrafast X-ray scattering," *Science* **316**, 1444-1448 (2007).
- [7] Neutze, R., Wouts, R., Van der Spoel, D., Weckert, E., and Hajdu, J., "Potential for biomolecular imaging with femtosecond X-ray pulses," *Nature* **406**, 752-757 (2000).
- [8] Pfeiffer, F., and Bunk, O., (private communication).
- [9] Fung, R., Shneerson, V., Saldin, D. K., and Ourmazd, A., "Structure from fleeting illumination of faint spinning objects in flight," *Nature Phys.* **5**, 64-67 (2009).
- [10] Kam, Z., "Determination of macromolecular structure in solution by spatial correlation of scattering fluctuations," *Macromolecules* **10**, 927-934 (1977).
- [11] Robinson, I. K., Da, Y., Spila, T., and Greene, J. E., "Coherent diffraction patterns of individual dislocation strain fields," *J. Phys. D* **38**, A7-A10 (2005).
- [12] Samaras, M., Derlet, P. M., Van Swygenhoven, H., and Victoria, M., "SIA activity during irradiation of nanocrystalline Ni," *J. Nucl. Mater.* **323**, 213-219 (2003).
- [13] Wirth, B. D., et al., "Multiscale modelling of radiation damage in Fe-based alloys in the fusion environment," *J. Nucl. Mater.* **329-333**, 103-111 (2004).
- [14] Goodman, J. W., *Statistical Optics* (John Wiley & Sons, New York, 1985).
- [15] Reiche, S., (private communication).
- [16] Saldin, E. L., Schneidmiller, E. A., and Yurkov, M. V., "Coherence properties of the radiation from X-ray free electron laser," *Opt. Commun.* **281**, 1179-1188 (2008).
- [17] Xiang, D. and Stupakov, G., "Echo-enabled harmonic generation free electron laser," *Phys. Rev. ST Accel. Beams* **12**, 030702 (2009).
- [18] Wu, J. H., Bolton, P. R., Murphy, J. B., and Zhong, X. M., "Free electron laser seeded by IR laser driven high-order harmonic generation," *Appl. Phys. Lett.* **90** 021109 (2007).
- [19] Henderson, R., "The potential and limitations of neutrons, electrons and X-rays for atomic-resolution microscopy of unstained biological molecules," *Quart. Rev. Biophys.* **28**, 171-193 (1995).
- [20] Lucic, V., Forster, F., and Baumeister, W., "Structural studies by electron tomography: From cells to molecules," *Annu. Rev. Biochem.* **74**, 833-865 (2005).
- [21] Taylor, K. A. and Glaeser, R. M., "Retrospective on the early development of cryoelectron microscopy of macromolecules and a prospective on opportunities for the future," *J. Struct. Biol.* **163**, 214-223 (2008).
- [22] Gonen, T., et al., "Lipid-protein interactions in double-layered two-dimensional AQP0 crystals," *Nature* **438**, 633-638 (2005).
- [23] King, W. E., et al., "Ultrafast electron microscopy in materials science, biology, and chemistry," *J. Appl. Phys.* **97**, 111101 (2005).
- [24] Shapiro, D. A., et al., "Powder diffraction from a continuous microjet of submicrometer protein crystals," *J. Synchr. Radiat.* **15**, 593-599 (2008).
- [25] Spence, J. C. H., et al., "Diffraction and imaging from a beam of laser-aligned proteins: resolution limits," *Acta Crystallogr. A* **61**, 237-245 (2005).
- [26] Hau-Riege, S., (private communication).
- [27] CIHR Strategic Training Program in the Structural Biology of Membrane Proteins, http://www.biochemistry.utoronto.ca/CIHR_membrane/program1.html.
- [28] Overington, J. P., Al-Lazikani, B., and Hopkins, A. L., "How many drug targets are there?" *Nature Rev. Drug Discov.* **5**, 993-996 (2006).
- [29] Lehninger, A.L., Nelson, D. L., and Cox, M. M., *Principles of Biochemistry*, 5th ed. (W. H. Freeman, New York, 2008).
- [30] Bech, M., et al., "X-ray imaging with the PILATUS 100k detector," *Appl. Radiat. Isot.* **66**, 474-478 (2008).
- [31] DECTRIS, <http://www.dectris.com/index.html>.
- [32] Schmitt, B., HPAD detector development, (private communication).

IV. Ultrafast Biochemistry

Initial events and fluctuations in biochemical processes at the atomic scale

- Time and length scales of biochemical reactions
- Photo-initiation of biochemical processes
- Time-resolved measurement techniques
- The photocycle of bacteriorhodopsin
- Dynamics of protein folding and catalytic action
- Mesoscopic non-equilibrium thermodynamics

Sub-nanosecond processes are fundamental to biochemistry and will be accessible to the ultrashort pulses of the SwissFEL. Important categories of ultrafast natural and artificial photoexcited bio-reactions exist, and the phenomenon of molecular caging offers the possibility of rapidly photo-triggering wide classes of biochemical phenomena. Although a typical bio-reaction, involving the coordinated motion of large protein subunits, may require a millisecond to complete, the reaction occurs on a complex energy landscape, passing through a continuum of biologically-relevant intermediate states. The temporal and spatial resolution provided by the SwissFEL will allow the exploration of molecular biochemical trajectories on these energy landscapes, both as irreversible pump-probe events or as equilibrium fluctuations. Fresh insights into the biochemical processes at short time and length scales, compatible with the SwissFEL can be won by applying the developing formalism of meso-scale non-equilibrium thermodynamics.

Time and length scales of biochemical reactions

The biological length scales pertinent to SwissFEL applications span the spectrum from individual atomic bonds and small molecules, such as glucose, in the sub-nanometer range, over individual protein molecules (e.g., hemoglobin) and molecular complexes (e.g., ribosomes) in the 1–10 nm range, over virus particles and cell organelles (10–100 nm), to entire cells (1 μm) (see Fig. IV.1). As discussed in Chapter III, with hard radiation from the SwissFEL ($\lambda = 0.1$ nm), lensless imaging of nanostructures is feasible at sub-nm resolution. As the sampled objects grow larger and more complex, the realistically achievable resolution degrades, to perhaps several tens of nm for micrometer-sized cells.

The vibration period of the two carbon atoms in the ethene molecule against their mutual double bond is 20 fs, and such molecular vibrations also set the time scale for photo-dissociation processes, for example for the photo-detachment of CO from a heme group (i.e., an iron atom surrounded by a porphyrin ring). As biomolecular units increase in size, from methyl groups (0.3 nm) to side-chains (1 nm) to loops (4 nm), to large protein domains (8 nm), collective motions with long periods populate the crowded vibrational density of states. Although electron transfer processes can in principle be very fast, their speed is generally limited by that of molecular reformation. The same is true for decaging processes – the activation of a biomolecule by the photo-removal of a deactivating cage group.

Photo-initiation of biochemical processes

The present Chapter concerns itself with the investigation of ultrafast biochemical processes with the SwissFEL. Since most such studies will be performed in the optical pump – X-ray probe scheme, one needs to ask: which photo-initiated effects can be used as optical pump triggers? Well-known photo-excited biochemical processes in proteins can be classified as “natural” or “artificial” [1]. *Natural* photo-activated protein-components are: the photosynthetic reaction center of chlorophyll (causing light-harvesting and electron transfer), the retinal group in rhodopsin vision complexes (causing isomerization, proton pumping and membrane polarization), the flavin group in DNA photolyase (performing DNA repair in plants by photocatalytically removing pyrimidine dimers) the cryptochrome and phototropin photoreceptors (causing electron transfer and covalent reactions), and the linear tetrapyrroles in phytochrome photoreceptors of plants and bacteria (causing photoisomerization). *Artificial* photo-activated components are: the flavin group in flavodoxin (causing electron transfer), and the heme group in hemoproteins (e.g., myoglobin) (causing redox chemistry and a so-called “protein quake” – see Fig. IV.2).

A major theme in fast and ultrafast biochemistry, discussed below, is the folding of a protein to its native state. Several methods of photo-initiating the folding process have been developed, including: a) rapid temperature jumps, down to 50 ns, which cause, e.g., helix solvation [4], b) ns laser photolysis of folding-inhibiting

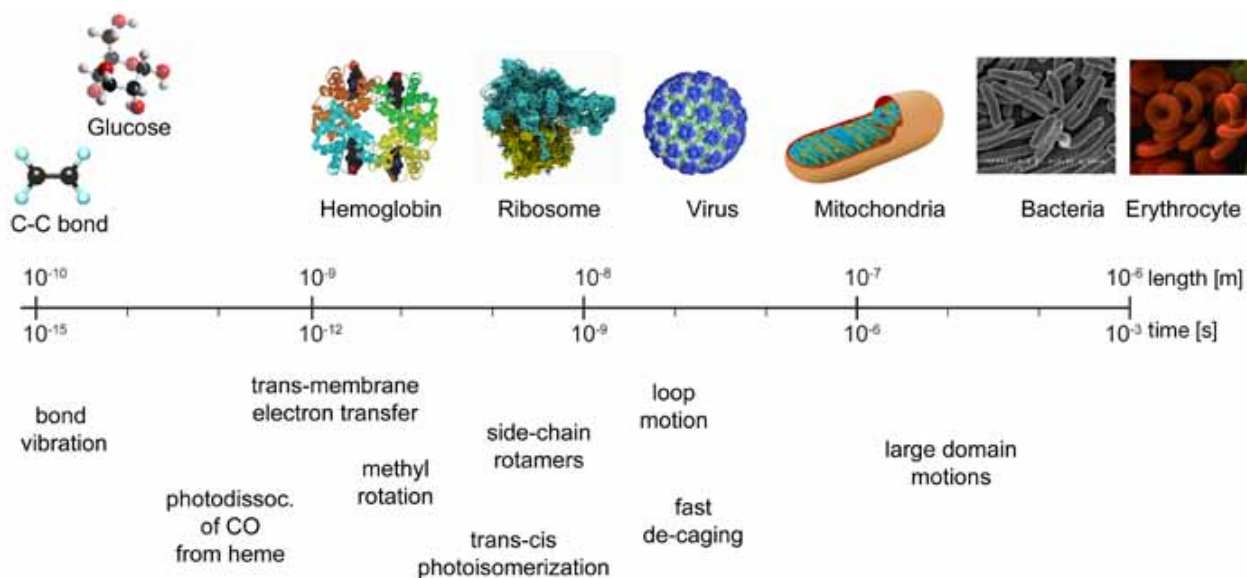


Fig. IV.1. The time and length scales for biochemical processes match well to the capabilities of the SwissFEL.

ligands [5], c) photo-cleavable protein cross-linking reagents [6], and d) folding induced by electron transfer [7]. A further possible fast perturbation of biomolecules in solution is via a ps terahertz pulse. It is known that THz absorption disrupts the H₂O network by breaking hydrogen bonds and that the function of a protein molecule is influenced by its surrounding solvation shell of up to 1000 water molecules [8].

Finally, it is possible to reversibly deactivate a biomolecule by the addition of a caging group [9, 10]. When this group is photocleaved away, by a visible or UV light pulse, the biomolecule becomes activated, via a rapid series of decaging reactions (see Fig. IV.3). A particularly attractive possibility is to rapidly decage the biological energy-carrier ATP [11], a feat which has been accomplished, using a Coumarin derivative, yielding a decaging time of 600 ps [12].

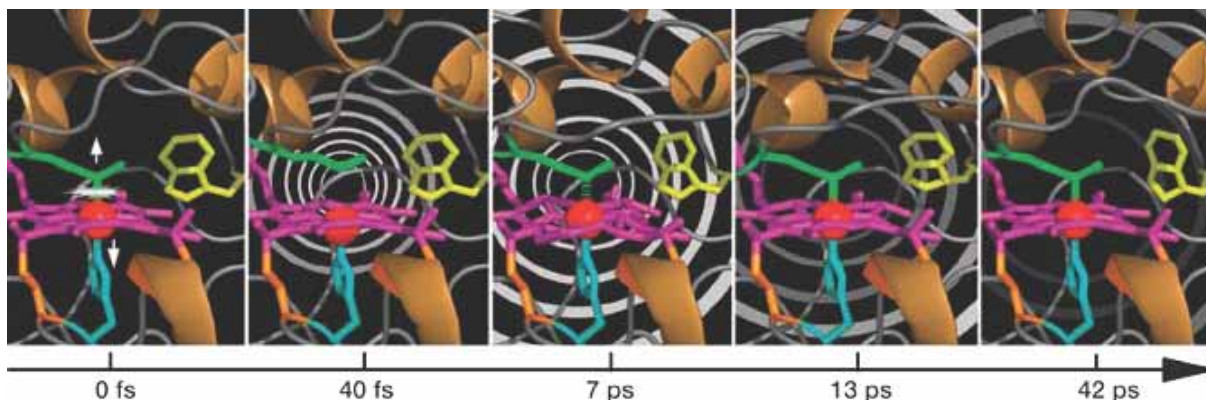


Fig. IV.2. Schematic view of a “protein quake” [2] of propagating distortions, initiated by breaking a heme-ligand bond in the photo-sensitive protein cytochrome c [3].

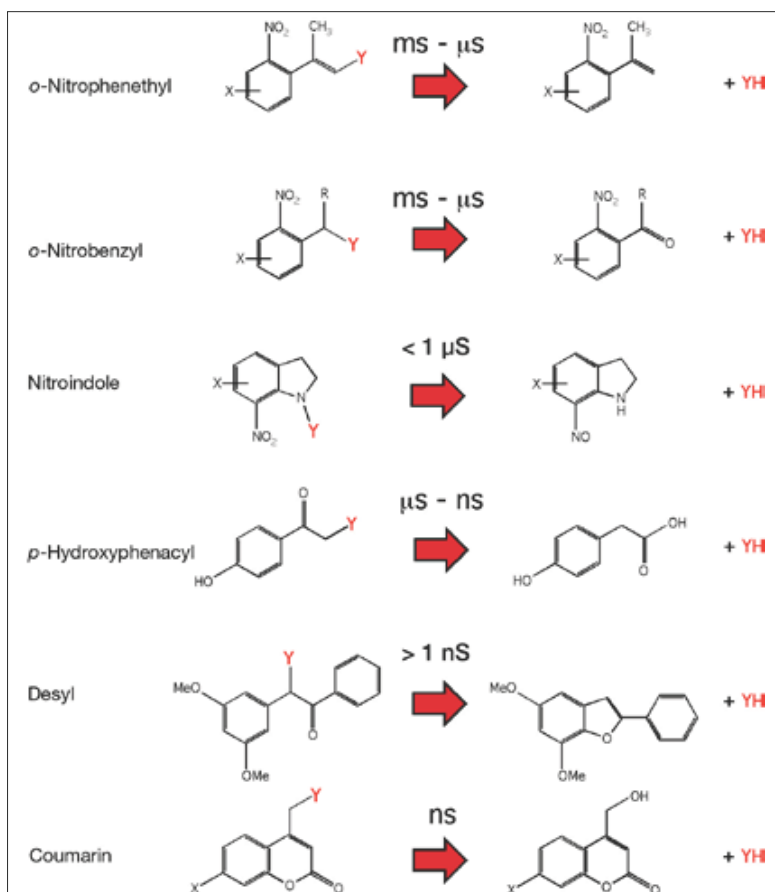


Fig. IV.3. A caged-molecule is one which has been de-activated by the addition of a cage-group. Exposure to UV-light removes the group, initiating a particular bio-reaction. Typical decaging rates for various cage groups bound to an active biomolecule “Y” lie in the range ns-ms [9].

Time-resolved measurement techniques

Several methods of studying biochemical dynamics have been developed. Among the low-resolution methods are: optical absorption spectroscopy in the visible and IR regions, circular dichroism and Raman scattering. The hydrogen-deuterium exchange method, based on the different exchange rates of hydrogen isotopes for exposed and hidden amino acids in a protein immersed in D_2O , detects folding or unfolding on the time scale of milliseconds or longer. The Fluorescence Resonant Energy Transfer (FRET) method allows a determination of

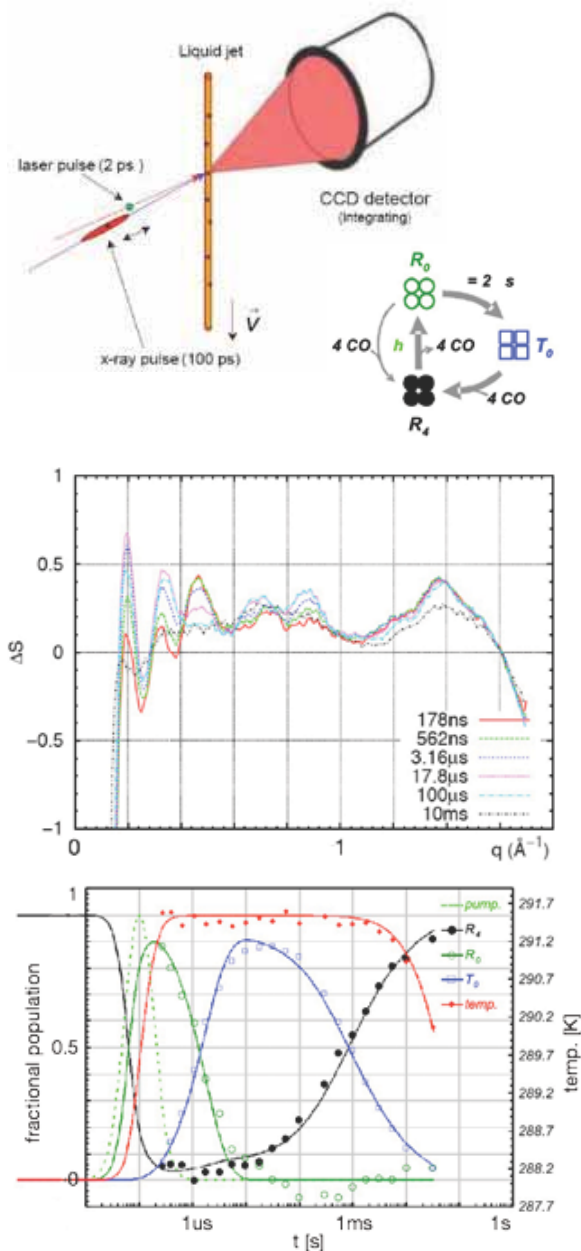


Fig. IV.4. A pump-probe SAXS instrument, with time-resolved data on the hemoglobin photocycle [15]. The time resolution is determined by the 100 ps X-ray pulse.

Fluorescence Resonant Energy Transfer (FRET)

FRET is an optical spectroscopic technique with which the dynamics of a single biomolecule can be followed (Fig. IV.i1). Incident optical light is absorbed by chromophore 1 at position 1 in the biomolecule. If sufficiently close by, i.e., if the protein is folded, the excitation energy can be transferred to a different chromophore 2, at position 2 in the molecule, resulting in the characteristic fluorescence signal of chromophore 2. If the inter-chromophore distance is too great, fluorescence will occur characteristic of chromophore 1. For single molecule FRET, the achievable time resolution is of the order of 10 ns [14]. Although a powerful technique for following the dynamic behavior of a single biomolecule, FRET cannot provide the detailed structural information available with the SwissFEL.

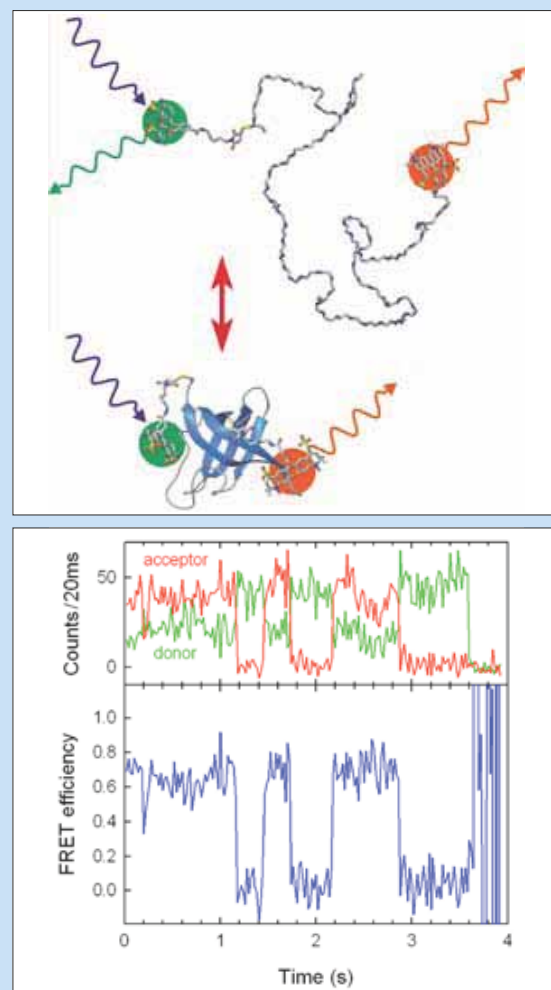


Fig. IV.i1. The FRET method, using red and green chromophores to demonstrate rapid, reversible transitions between the unfolded and folded states of a single molecule of the cold-shock protein from *Thermotoga maritima* (CspTm) [13].

the state of folding of a single protein molecule with a time resolution of the order of 10 ns [13, 14] (see Infobox). Atomic scale information can be obtained by Nuclear Magnetic Resonance on the time scale of 10–0.1 seconds, by the observation of peak splitting, and of ms – μ s, by line broadening.

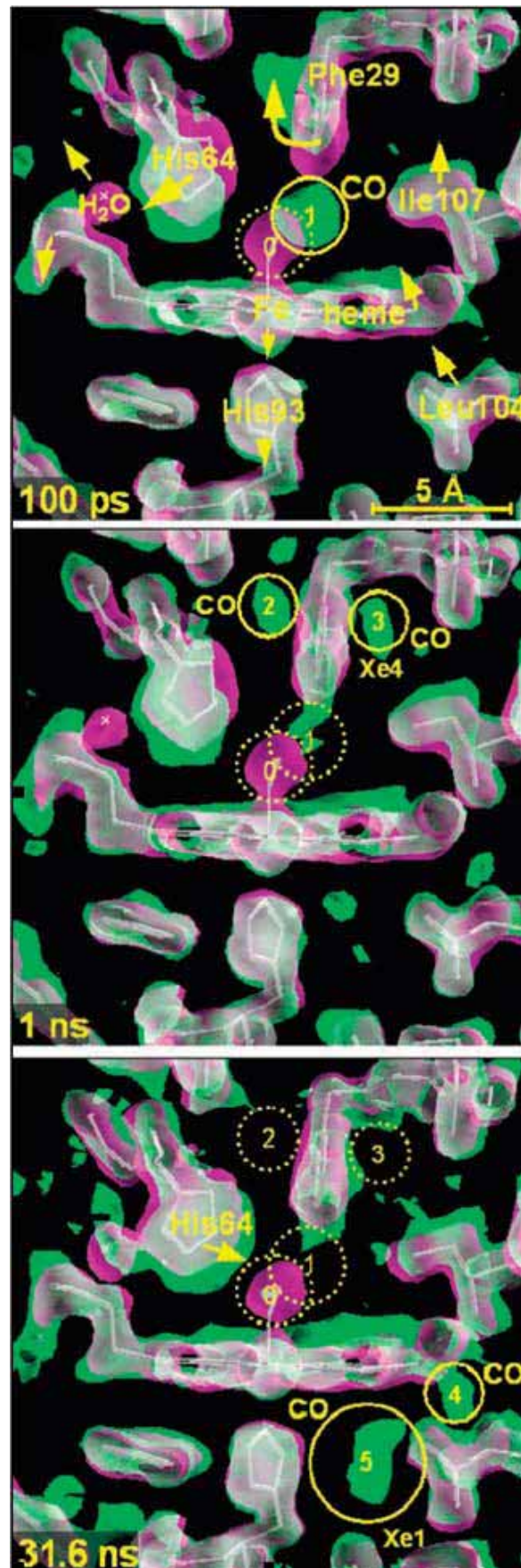
Synchrotron-based, time-resolved Small and Wide Angle X-ray Scattering (TR-SAXS/WAXS) from photo-triggered biomolecules in solution is capable of providing nm spatial resolution and 100 ps time-resolution, limited by the X-ray pulse length (see Fig. IV.4) [15]. Biomolecules are carried by a liquid jet – at the SwissFEL this must be in vacuum – using the technology presented in Chapter II. An optical laser pulse excites the molecules, which are then probed, after a preset time delay, by the 100 ps X-ray pulse.

The same experimental station as used for time-resolved SAXS is also employed to perform pump-probe Laue crystallography. For the CO-photo-detachment in crystalline myoglobin, shown in Figure IV.5, broadband X-ray pulses (3% bandwidth, centered at 15 keV photon energy) were used. Each X-ray pulse had 10^{10} photons, 32 pulses were acquired for each crystal orientation, and 31 different orientations were measured, without laser pump and with various pump-probe delays.

With stable, ultra-short pulses from the SwissFEL, such time-resolved pump-probe SAXS and Laue experiments will be possible with a much improved 20 fs time resolution. Optimally configured broad-band radiation for time-resolved Laue diffraction will be provided by detuning the individual undulator sections of the SwissFEL, at some cost in intensity.



Fig. IV.5. Left: A Laue exposure of a myoglobin crystal, taken with 32 100 ps X-ray pulses. Right: Time-resolved structure of the heme region of myoglobin: CO, showing the photo-detachment of CO, its migration to sites “2” and “3”, and the relaxation response of the neighboring protein structures (from [16]).



The photocycle of bacteriorhodopsin

As an example of a classic photo-induced biochemical process, we discuss the photocycle of bacteriorhodopsin, a model system for the biological basis of vision. The information presented was obtained using pump-probe optical spectroscopy and X-ray diffraction from flash-frozen samples. Pump-probe SAXS or Laue experiments at the SwissFEL offer the exciting possibility of directly determining the detailed molecular structure of even the shortest-lived intermediate states.

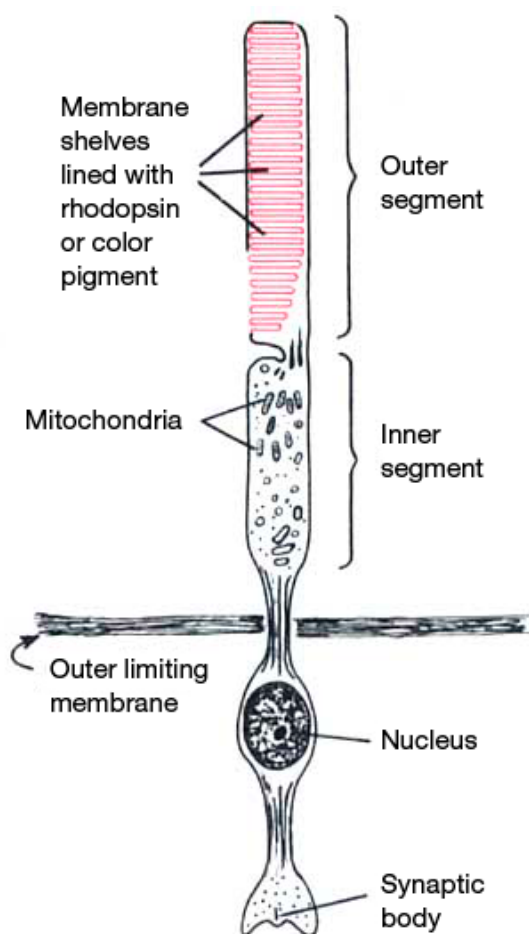


Fig. IV.6. The light-sensitive rod cells of the vertebrate eye. The rhodopsin photocycle converts an absorbed photon into a transfer of protons across a neural membrane and hence leads to the generation of a nerve impulse.

In higher organisms, including invertebrates and humans, it is the membrane protein rhodopsin, found in the rod cells of the retina (see Fig. IV.6), which delivers the photon energy to a complex series of biochemical processes, leading ultimately to an electrical polarization of the membrane and hence to a nerve impulse. In 1967, Wald, Granit and Hartline received the Nobel prize for

medicine for the discovery of the initial event in vision: a photon-induced trans \rightarrow cis structural transformation in retinal, the photoreceptor located at the center of the rhodopsin molecule. This transformation is the fastest biological photoreaction known (see Fig. IV.7).

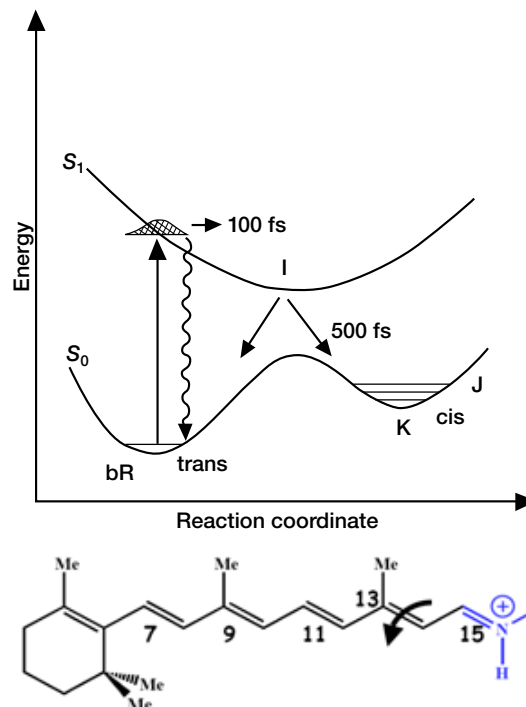


Fig. IV.7. The ultrafast photo-induced trans \rightarrow cis transition in retinal is the initial event in vision and the fastest known biological photo-reaction.

Due to a highly complex photocycle and problems of photo-instability, rhodopsin is difficult to handle in the laboratory. Bacteriorhodopsin (bR), extracted from the “purple membrane” of *Halobacterium salinarum*, is easier to study and has a simpler photocycle (see Fig. IV.8) [17]. However, in spite of the fact that no membrane protein has been studied as extensively as bR, details of its photocycle are still controversial.

Recent fs optical spectroscopy experiments have identified two additional short-lived intermediate states, not shown in Figure IV.8, which form just after the photo-excitation (see Fig. IV.7, above): The “I-state”, which forms within 200 fs, is believed to incorporate an incomplete (90°) bond rotation, and the “J-state”, with a rise time of 500 fs, may be a vibrationally-excited version of the K state. Finally, high-resolution flash-frozen X-ray diffraction investigations of bR indicate distortions in the helices of the entire bR molecule [18] (see Fig. IV.9). For bacteriorhodopsin and other photo-sensitive biomolecules, a wealth of information is awaiting the greatly improved spatial and temporal resolutions of the SwissFEL.

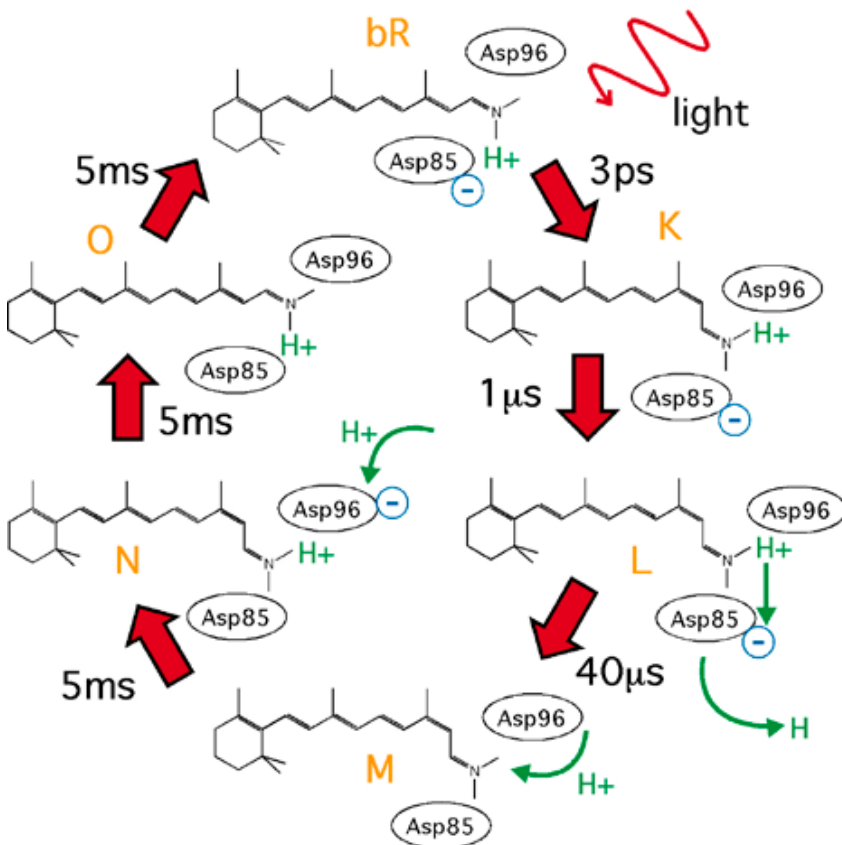


Fig. IV.8. The bacteriorhodopsin photocycle. Note the transfer of H⁺ from the cytoplasmic side to the extra-cellular side of the membrane, which is responsible for the membrane polarization (only the central retinal group of the protein is shown). Ultrafast photocycles such as this are prime targets for investigation with TR-SAXS at the SwissFEL.

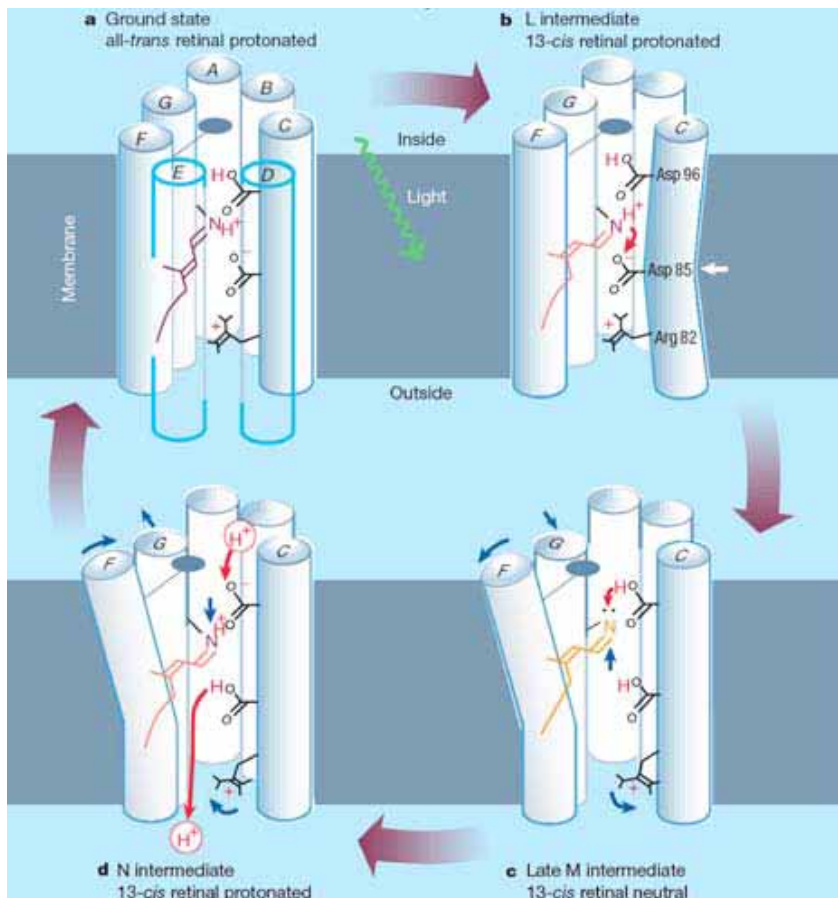


Fig. IV.9. Distortions in the bR helices for the L, M and N intermediate states, as determined in flash-frozen samples using X-ray diffraction [18]. Time-resolved scattering experiments at the SwissFEL will follow such detailed structural changes in real time.

Dynamics of protein folding and catalytic action

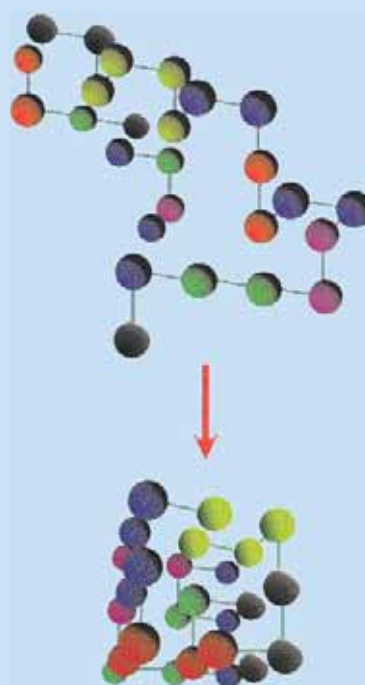
Synchrotron-based X-ray protein crystallography is the ideal technique for determining the static atomic-scale structure of protein molecules and their complexes, provided sufficient material can be purified and crystallized. But it is the *dynamic* structure of a protein molecule which determines its function. One can see from Figure IV.1 that major reconformations of proteins are slow processes on the scale of the 20 fs XFEL pulse duration, requiring μ s to ms to complete. What are the important questions regarding the folding process [19, 20] to which the SwissFEL can contribute?

Since the work of Anfinsen et al, in the early 1960's [21], it is known that the folding of a protein is a reversible process; the native structure is a thermodynamically stable configuration, corresponding to a global minimum of the accessible free energy. But according to the "Levinthal paradox" (see Infobox), it is virtually impossible for a protein molecule to sample all of the available structures. Dill and Chan [19] ask the question: "Among a multitude of possibilities, how does a protein find its equilibrium structure?"

In its search for the minimum energy state, the protein can be thought to move on an energy surface in (higher-dimensional) conformational space, the shape of which is determined by the amino-acid sequence of the protein and by external factors such as pH, temperature, degree of solvation, and the presence of neighboring "chaperone" proteins (see Infobox). What is the nature of this energy surface? Several schematic possibilities are shown in Figure IV.10 [19]. The Levinthal paradox is portrayed in Figure IV.10a – the "Levinthal golf course": the unrealistic absence of an energy gradient presents the protein with an insurmountable entropic barrier to finding the minimum-energy state. The alternative of a narrow "folding pathway" (Fig. IV.10b) is also deemed unrealistic, since it fails to describe proteins which happen to land off the beaten road. Current thinking prefers the picture that the protein performs a diffusional motion on the "trickle funnel" landscape shown in Figure IV.10c: all the protein molecules are guided to the native state, albeit with possible detours around local energy maxima and entropic delays in regions of low gradient. It has been proposed that part of the folding trajectory consists of "hydrophobic zipping" [22, 23]. This is "an opportunistic process in which local contacts (nearby in the sequence) form first, drawing in new contacts, which create still other and increasingly nonlocal contacts and opportunities of other intrachain interactions. Helices, turns and other local structures would be the first to zip" [19].

Levinthal's paradox

In the late 1960's, Cyrus Levinthal formulated the "Levinthal paradox" [27], which can be expressed as a statistical problem [28]: Consider a protein molecule composed of 100 residues, each of which can assume 3 different conformations. For the number of possible structures, this yields $3^{100} = 5 \times 10^{47}$. Now assume that it takes (only) 100 fs to convert from one structure to another. It would thus require 5×10^{34} s = 1.6×10^{27} years to (systematically) explore all possibilities.



The disagreement between this long time and the actual folding time (μ s – ms) represents Levinthal's paradox.

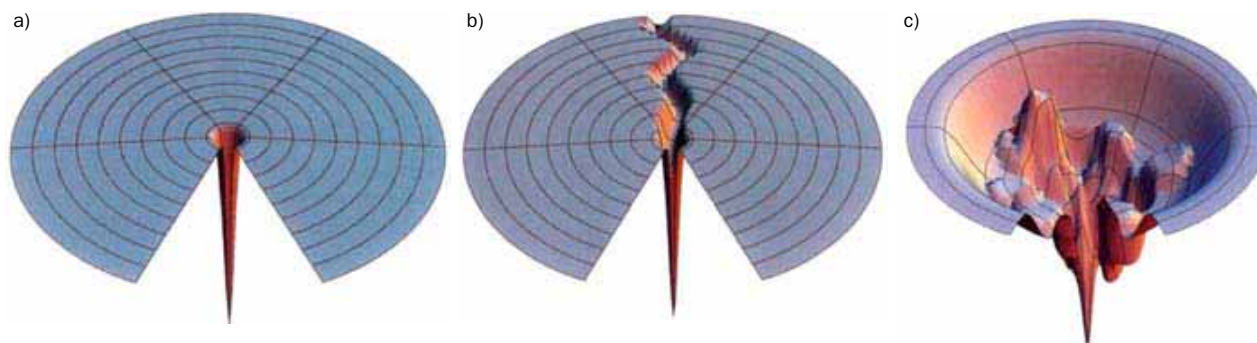


Fig. IV.10. Three conceptual possibilities for the energy landscape for protein folding, with the energetically-favored native state at the lowest point [19]. a) The flatness of the “Levinthal golf course” presents an insurmountable entropic barrier to folding. b) A “folding pathway” can guide only a chosen few of the molecules to the energy minimum. c) A “trickle funnel” is currently the preferred picture, where local detours and entropic barriers cause the folding rate to fluctuate. Time-resolved measurements at the SwissFEL offer promising possibilities for characterizing such energy landscapes.

Dill and Chan [19] stress that it would be particularly valuable to have an experimental method capable of quantifying the time-dependent structural correlations occurring in an ensemble of identical fluctuating proteins (see Fig. IV.11). This, they argue, would provide important information on the nature of the energy landscape and on the diffusional trajectories followed by the folding and unfolding proteins. The time-space correlation method proposed by Kam (see Chapter III) for studying the static structure of biomolecules in solution could conceivably be extended, using the SwissFEL, to the investigation of such dynamic structural correlations.

Examining the protein-folding energy landscape in detail, Henzler-Wildman and Kern [20] classify the energy barriers according to their heights into “tiers” 0, 1 and 2 (see Fig. IV.12). Tier 0 refers to barriers of several $k_B T$, corresponding to “larger-amplitude collective motions between relatively small numbers of states.” Transitions between these states occur on the μs time-scale or slower and form the basis of many important biological processes, including “enzyme catalysis, signal transduction and protein-protein interactions”. On the finer scales of tiers 1 and 2, a “large ensemble of structurally similar states that are separated by energy barriers of less than one $k_B T$ result in more local, small-amplitude ps to ns fluctuations at physiological temperature”. It has been determined that these fluctuations, involving, e.g., loop motions (ns) and side-chain rotations (ps), in effect “pre-sample” the characteristic motions of catalytic action. Still finer than tier 2 are the fs-scale fluctuations related to bond vibrations and interactions with the solvent. Henzler-Wildman and Kern differentiate between the large tier 0 “enthalpic barriers”, relevant to confor-

mational change and the “entropic barriers” on the scale of tiers 1 and 2, which are related to minor rearrangements among neighboring peptides and in their interactions with the solvent.



Fig. IV.11. Measuring correlations, for example between the fluctuations of two bond angles θ_i and θ_j , will help determine whether degrees of freedom are synchronized, as in the pathway model, or asynchronous at first and becoming more synchronized later [19].

Thus, whereas the coherence and high peak flux of the SwissFEL make it a powerful tool for quantifying large conformational changes of proteins, its real power lies in the ability to follow the pre-sampling of biologically important pathways occurring via delicate fs-ps-ns fluctuations. Fundamental questions regarding protein dynamics, which the SwissFEL may help resolve, include [19, 20, 24]:

- What are the predominant structures and the distance distributions in the unfolded state?

- What is the “speed limit” for elementary dynamics along the energy surface?
- How rugged is the energy landscape? A rugged landscape implies fluctuations among very different conformations.
- Is it possible to measure not only averages of structural observables, but also correlations among their fluctuations (Fig. IV.11)?
- Can minor conformational substates be predicted from known structures?
- How can this knowledge and a dynamic view of proteins be used to help discover and develop novel therapeutic agents?

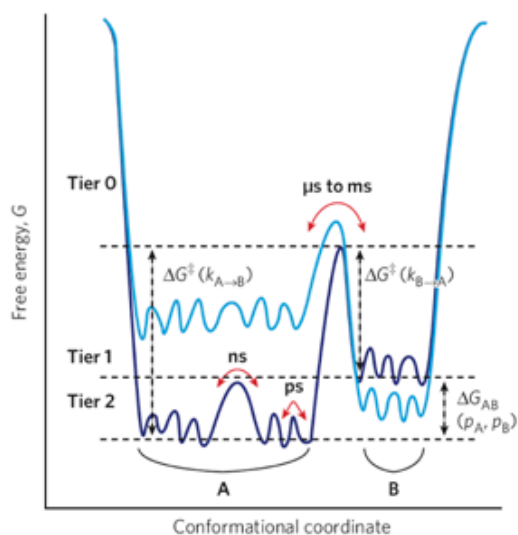
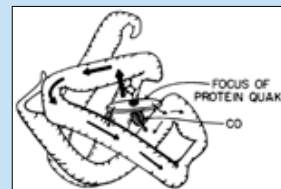
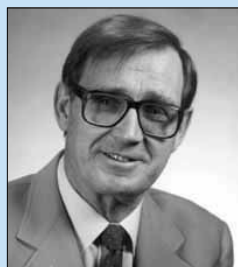


Fig. IV.12. The hierarchy of energy barriers in protein dynamics [20]: Tier 0, with $\Delta G > k_B T$, dictates large conformational changes on the μ s and slower time scale. Tiers 1 and 2 represent finer motions of loops and side-chains. Not shown are still finer fs fluctuations involving bond vibration and the motion of solvent molecules. While it is the occasional slow structural changes that embody biological function, a constant pre-sampling of important pathways is always taking place at smaller spatial and faster temporal scales.

HANS FRAUENFELDER

born 1922 in Schaffhausen, Switzerland,
PhD from ETHZ



A protein-quake[2].

Quote from Ref. [29]:

To carry out their functions, most proteins must perform motions. These motions can either be thermal equilibrium fluctuations or non-equilibrium relaxations, caused for instance by reactions. In terms of the energy landscape, motions can be described as jumps of the system from substates to substates. A task of biological physics is the experimental study of these motions, their connections to structure, and to the energy landscape. Since **the rate coefficients of fluctuations range from fs^{-1} to s^{-1}** or possibly even less, it is clear that **many different tools are needed**.

It has been known for some time that proteins share properties with glasses. Recent studies show that this similarity has unexpected aspects, related to the interaction of the protein proper with the bulk solvent and with its hydration shell. Consider first the large-scale fluctuations. A comparison of the rate coefficients, $k_p(T)$, for large-scale motions in proteins, for instance entry and exit of ligands, with the rate coefficient $k_\alpha(T)$ of the bulk solvent shows that they have the same temperature dependence over many orders of magnitude. In other words, large-scale fluctuations of the protein are slaved to the fluctuations in the bulk solvent. These protein processes are controlled by enthalpy barriers in the solvent, not by protein-internal enthalpy barriers. But a puzzle appears: while $k_p(T)$ and $k_\alpha(T)$ have the same temperature dependence, for some processes $k_p(T)$ is 10^5 times slower than $k_\alpha(T)$! **What causes this slowing? It obviously must be entropy or, in other words, the large number of states in the protein.** Here is where the energy landscape comes in. A process like the exit of a ligand is not like opening a rigid door. Many side chains must be in the right position, helices may have to move. Opening thus corresponds to a random walk in conformation space. Indeed, theory supports such a picture. Significant properties of proteins follow from these experimental results: proteins work in close interaction with their environment, the environment controls the enthalpy barriers for large-scale motions; the protein proper contributes to the entropy as characterized through the energy landscape.

A complete understanding of the energy landscape and of the related fluctuation and relaxation processes is still a dream, but it is a grand challenge for biological physics.

Non-Equilibrium Thermodynamics (NET)

To derive the diffusion equation in the NET formalism [25] (where, for example, the chemical potential μ and the particle density ρ may depend on the position x), one begins with the Gibbs equation for entropy change, assuming constant temperature, energy and volume:

$$T \frac{\partial S}{\partial t} = - \int \mu[x, \rho(x)] \frac{\partial \rho(x)}{\partial t} dx$$

Introducing the mass flux J via the conservation law $\frac{\partial \rho}{\partial t} = - \frac{\partial J}{\partial x}$ and performing integration by parts (with J vanishing at the system boundary), one obtains:

$$T \frac{dS}{dt} = - \int J \frac{\partial \mu}{\partial x} dx.$$

This expression establishes that J and $\frac{\partial \mu}{\partial x}$ are “conjugate” quantities, which, according to Onsager, are related by a linear flux-force relation:

$$J = - L \frac{\partial \mu}{\partial x}$$

where L is the Onsager coefficient. Inserting this expression into the conservation law yields the diffusion equation for the density:

$$\frac{\partial \rho}{\partial t} = \frac{\partial}{\partial x} D \frac{\partial \rho}{\partial x},$$

where $D = L \frac{\partial \mu}{\partial \rho}$ is the diffusion constant.

Mesoscopic non-equilibrium thermodynamics

It is clear from the discussion of the previous Section that issues of fluctuations and entropy, on short time and length scales, play an important role in ultrafast biochemistry. Furthermore, a biological system is of necessity in a state of non-equilibrium; “equilibrium” is a synonym for “death”. The question arises, is there a general formalism, on a level of sophistication above that of statistical mechanics, for treating a non-equilibrium state on the scale of macro-molecular fluctuations? Such a formalism, Mesoscale Non-Equilibrium Thermodynamics (MNET), is being developed for just this purpose [25].

Classical thermodynamics provides general rules for continuum, macroscopic systems in thermal equilibrium, in terms of a few parameters, such as the extensive variables internal energy, volume and mass, and intensive variables such as temperature, pressure and chemical potential. The dependence of the entropy on these variables is given by the Gibbs equation:

$$TdS = dE + pdV - \mu dM \quad (\text{equilibrium thermodynamics})$$

In a non-equilibrium situation, gradients in the intensive variables act as forces, causing extensive fluxes. Such cases are treated in the framework of non-equilibrium thermodynamics (NET), in which the system is considered to consist of many subsystems, each of which is described, still in a continuum approximation, by equilibrium thermodynamic variables and each of which experiences a non-negative change in entropy. Consider the simple case of one-dimensional mass diffusion at constant energy and volume ($dE = 0$, $dV = 0$). In NET, the Gibbs equation for non-equilibrium thermodynamics may now incorporate a chemical potential with explicit and implicit spatial dependences, and hence the expression for the entropy production should read (see Infobox):

$$T \frac{\partial S}{\partial t} = - \int \mu[x, \rho(x)] \frac{\partial \rho(x)}{\partial t} dx \quad (\text{NET})$$

Under certain assumptions (see Infobox), one obtains the well-known diffusion equation for the density:

$$\frac{\partial \rho}{\partial t} = \frac{\partial}{\partial x} D \frac{\partial \rho}{\partial x},$$

where $D = L \frac{\partial \mu}{\partial \rho}$ is the diffusion constant, and L is the Onsager coefficient.

Although NET allows the description of irreversible processes, the fact that it still is based on a continuum

picture makes it inappropriate to treat systems at the molecular level, where strong fluctuations are important. Furthermore, the defining relationships, such as the dependence of the fluxes on the forces, are linear. This makes it impossible for NET to describe, for example, activated processes in biochemistry. To extend NET to very short time and length scales (accessible with the SwissFEL), the statistical approach of Mesoscopic Non-Equilibrium Thermodynamics (MNET) is called for.

The starting point is again the dynamics of the entropy of a system, this time based on the Gibbs entropy postulate:

$$S = S_{eq} - k_B \int P(\gamma, t) \ln \frac{P(\gamma, t)}{P_{eq}(\gamma)} d\gamma \quad (\text{MNET})$$

which relates the deviation of entropy from its equilibrium value with the probability density P of finding the system in a state with particular values for its non-equilibrated degrees of freedom γ . These degrees of freedom could include, e.g., a particle velocity, a spin orientation or the conformation of a biomolecule.

The chemical potential is now $\mu(\gamma, t) = \Phi(\gamma, t) + kT \ln P(\gamma, t)$, where Φ is the activation energy barrier in an internal space coordinate at equilibrium, and the flux is again a linear function of the driving force

$$J(\gamma) = -L \left(\frac{kT}{P} \frac{\partial P}{\partial \gamma} + \frac{\partial \Phi}{\partial \gamma} \right) \quad (\text{MNET})$$

The NET expression for entropy production then leads to the Fokker-Planck equation

$$\frac{\partial P(\gamma)}{\partial t} = \frac{\partial}{\partial \gamma} \left(D \frac{\partial P}{\partial \gamma} + \frac{D}{kT} \frac{\partial \Phi}{\partial \gamma} \right) \quad (\text{MNET})$$

where the diffusion constant is now $D \equiv \frac{k_B L(\gamma, P)}{P}$, and $L(\gamma, P)$ is again an Onsager coefficient, this time dependent on the thermodynamic state P and the mesoscopic coordinates γ . Here one has an explicit formalism to treat on equal footing an enthalpic and an entropic barrier. In a manner similar to the dissipation-fluctuation theorem (see Chapter I), MNET provides a method to “determine the dynamics of a system from its equilibrium properties”.

Mesoscopic Non-Equilibrium Thermodynamics has application in the study of transport processes in confined systems, such as those in the biochemistry of the cell [26]. “Transport at the mesoscale is usually affected by the presence of forces of different nature: direct interactions between particles, hydrodynamic interactions mediated by the solvent and excluded volume effects. The presence of such diversity of forces has a direct implication in the form of the energy landscape, which may exhibit a great multiplicity of local minima sepa-

rated by barriers. Transport at those scales presents two main characteristics: it is intrinsically non-linear, and it is influenced by the presence of fluctuations, external driving forces, and gradients. MNET can be used to infer the general kinetic equations of a system in the presence of potential barriers, which in turn can be used to obtain the expressions for the current of particles and the diffusion coefficient” [25]. The fields of application of MNET, namely molecular systems undergoing rapid fluctuations, match well those of the SwissFEL, and it is anticipated that the two could form a tight symbiotic relationship of theory and experiment.

Protein folding and human health

The protein-folding problem has a direct relationship to human health (see Fig. IV.i2). “Misfolded and aggregated proteins may be involved in pathological conditions such as Alzheimer’s disease, cystic fibrosis and cataracts. The infectious agent (or prion) in the neurodegenerative diseases scrapie (in sheep), bovine spongiform encephalopathy (BSE, or “mad cow” disease), and Creutzfeldt-Jakob disease (in humans) is also thought to be a misfolded protein” [30].

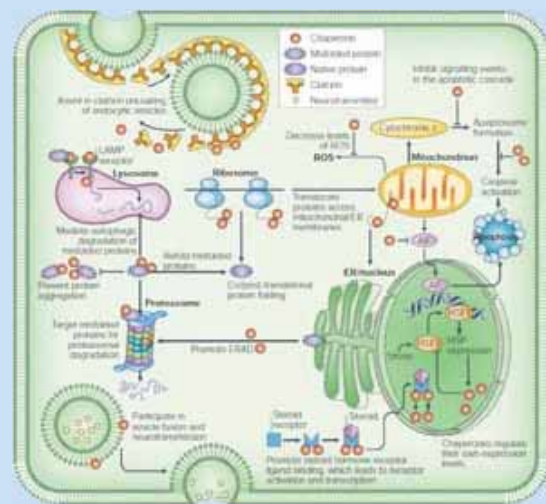


Fig. IV.i2. “Molecular chaperones” are proteins which assist the proper folding of other proteins in the confines of a cell. Their function is particularly important in preventing neurodegenerative disorders such as Alzheimer’s, Parkinson’s and Huntington’s diseases [31].

Summary

- *Important biochemical reactions that require μs to ms to run to completion are composed of more elementary steps on the sub-ns scale.*
- *Ultrafast events, on the time scale of fs to ps, occur in photo-initiated reactions, such as photosynthesis, vision and DNA repair, and as fluctuations during slower reactions, which effectively “pre-sample” the relevant energy landscape.*
- *The structurally-sensitive X-ray techniques of small-angle scattering and Laue diffraction, when performed in a pump-probe manner, provide atomic-level detail not available with optical spectroscopy.*
- *The textbook example of an ultrafast photo-triggered bioreaction, the photocycle of bacteriorhodopsin, contains many unanswered questions regarding ultrafast structural changes, and it points to similar questions in other important photo-reactions.*
- *Proteins manage to efficiently find their preferred native state, in spite of an astronomic number of possible conformations. Explaining in detail how this occurs requires experimental methods which are sensitive to local dynamic structural correlations.*
- *A rigorous theoretical foundation which accounts for the statistical nature of mesoscale chemical systems on short time scales, “mesoscopic non-equilibrium thermodynamics”, is currently being developed and offers a promising framework for interpreting future SwissFEL experiments in biochemistry.*

References

- [1] Vos, M. and Van Thor, J., (private communication).
- [2] Ansari, A., et al., "Protein states and protein quakes," *Proc. Nat. Acad. Sci. USA* **82**, 5000-5004 (1985).
- [3] Zang, C., et al., "Ultrafast protein quake dynamics in Cytochrome C," *J. Am. Chem. Soc.* **131**, 2846-2852 (2009).
- [4] Gilmanshin, R., Williams, S., Callender, R. H., Woodruff, W. H., and Dyer, R. B., "Fast events in protein folding: Relaxation dynamics and structure of the I form of apomyoglobin," *Biochem.* **36**, 15006-15012 (1997).
- [5] Jones, C. M., et al., "Fast events in protein folding initiated by nanosecond laser photolysis," *Biophys. J.* **66**, A397-A397 (1994).
- [6] Milanese, L., Reid, G. D., Beddard, G. S., Hunter, C. A., and Waltho, J. P., "Synthesis and photochemistry of a new class of photocleavable protein cross-linking reagents," *Chem. Eur. J.* **10**, 1705-1710 (2004).
- [7] Pascher, T., Chesick, J. P., Winkler, J. R., and Gray, H. B., "Protein folding triggered by electron transfer," *Science* **271**, 1558-1560 (1996).
- [8] Ebbinghaus, S., et al., "An extended dynamical hydration shell around proteins," *Proc. Nat. Acad. Sci. USA* **104**, 20749-20752 (2007).
- [9] Goeldner, M., (private communication).
- [10] Specht, A., (private communication).
- [11] Wu, D., Tucker, R., and Hess, H., "Caged ATP - Fuel for bionanodevices," *IEEE Trans. Adv. Pack.* **28**, 594-599 (2005).
- [12] Geissler, D., et al., "DMACM-caged adenosine nucleotides: Ultrafast photo-triggers for ATP, ADR and AMP activated by long-wavelength irradiation," *Chem. Bio. Chem.* **4**, 162-170 (2003).
- [13] Rhoades, E., Cohen, M., Schuler, B., and Haran, G., "Two-state folding observed in individual protein molecules," *J. Am. Chem. Soc.* **126**, 14686-14687 (2004).
- [14] Nettels, D., Gopich, I. V., Hoffmann, A., and Schuler, B., "Ultrafast dynamics of protein collapse from single-molecule photon statistics," *Proc. Nat. Acad. Sci. USA* **104**, 2655-2660 (2007).
- [15] Cammarata, M., et al., "Tracking the structural dynamics of proteins in solution using time-resolved wide-angle X-ray scattering," *Nature Meth.* **5**, 881-886 (2008).
- [16] Schotte, F., et al., "Watching a protein as it functions with 150-ps time-resolved X-ray crystallography," *Science* **300**, 1944-1947 (2003).
- [17] Lanyi, J. K., "Bacteriorhodopsin," *Annu. Rev. Physiol.* **66**, 665-688 (2004).
- [18] Kuhlbrandt, W., "Bacteriorhodopsin – the movie," *Nature* **406**, 569-570 (2000).
- [19] Dill, K. A. and Chan, H. S., "From Levinthal to pathways to funnels," *Nature Struct. Biol.* **4**, 10-19 (1997).
- [20] Henzler-Wildman, K. and Kern, D., "Dynamic personalities of proteins," *Nature* **450**, 964-972 (2007).
- [21] Anfinsen, C. B., Haber, E., Sela, M., and White, F. H., "Kinetics of formation of native ribonuclease during oxidation of reduced polypeptide chain," *Proc. Nat. Acad. Sci. USA* **47**, 1309-1314 (1961).
- [22] Dill, K. A., et al., "Principles of protein-folding - A perspective from simple exact models," *Protein Sci.* **4**, 561-602 (1995).
- [23] Dill, K. A., Fiebig, K. M., and Chan, H. S., "Cooperativity in protein-folding kinetics," *Proc. Nat. Acad. Sci. USA* **90**, 1942-1946 (1993).
- [24] Schuler, B., (private communication).
- [25] Reguera, D., Rubi, J. M., and Vilar, J. M. G., "The mesoscopic dynamics of thermodynamic systems," *J. Phys. Chem. B* **109**, 21502-21515 (2005).
- [26] Kjelstrup, S., Rubi, J. M., and Bedeaux, D., "Active transport: A kinetic description based on thermodynamic grounds," *J. Theor. Biol.* **234**, 7-12 (2005).
- [27] Levinthal, C., "Are there pathways for protein folding," *J. Chem. Phys.* **65**, 44-45 (1968).
- [28] Stryer, L., Tymoczko, J. L., and Berg, J. M., *Biochemistry* 5th ed. (W. H. Freeman, New York, 2002).
- [29] Frauenfelder, H., in *5th International Conference on Biological Physics*, 413-416 (Gothenburg, Sweden, 2004).
- [30] Jones, C. M., "An Introduction to Research in Protein Folding for Undergraduates", *J. Chemical Education* **74**, 1306-1310 (1997).
- [31] Muchowski, P. J. and Wacker, J. L., "Modulation of neurodegeneration by molecular chaperones," *Nature Rev. Neurosci.* **6**, 11-22 (2005).

V. Time-Resolved Spectroscopy of Correlated Electron Materials

Mapping the flow of energy among strongly-coupled degrees of freedom

- Correlated electron phases
- X-ray methods in correlated electron science
- The origin of the metal-insulator transition in TaS₂
- Ultrafast investigations of the electron-phonon interaction
- Complexity in correlated electron materials

“Electron correlation” is a dominant theme in condensed matter science, manifesting itself in, e.g., “metal-insulator transitions” (MIT), “high-temperature superconductivity” (HTS) and “colossal magneto-resistance” (CMR). On the microscopic scale, one speaks of the charge (C), spin (S) and orbital (O) degrees of freedom, each of which may show short- or long-range order, and each of which may exchange energy with the others and with the crystal lattice (L) (see Fig. V.1). Important correlation effects can occur in systems with partially-filled electron shells, such as those of 3d-transition metal ions, with anisotropic, quasi-localized character. Vast amounts of experimental and theoretical work have been published on electron correlation, triggered largely by the discovery of HTS in 1986 [2]. Phase diagrams of many interesting materials have been investigated in detail, and numerous theories of the microscopic charge-spin-orbital-lattice interactions have been proposed. Much has been achieved, but much is still unclear. There is increasing evidence of the importance of nanoscale inhomogeneities and fast fluctuations in correlated electron materials – indicating the important role that the SwissFEL will play. Furthermore, it has been suggested that the chicken-or-egg problem, of determining the cause and effect relationships among the C, S, O and L subsystems, may best be approached with pump-probe time-resolved spectroscopy: one pumps energy into a particular degree of freedom and measures the time required for a response to appear in the others.

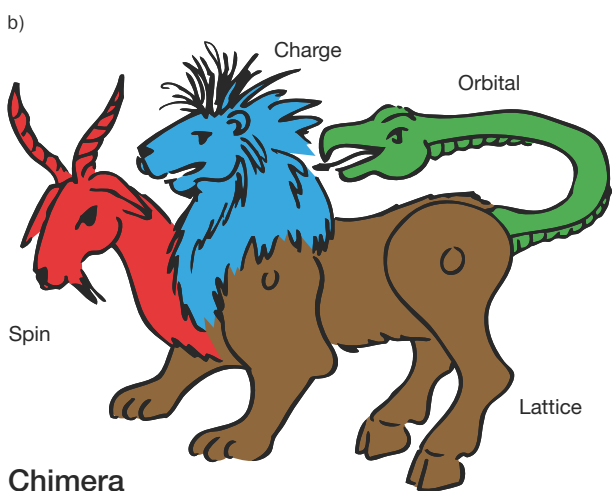
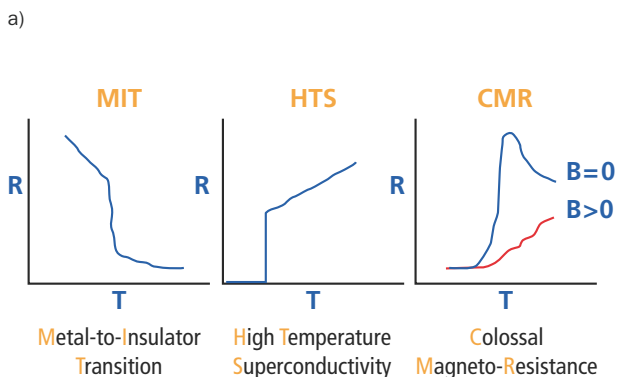


Fig. V.1. a) Three macroscopic manifestations of correlated electrons, with strong potential for important applications. b) The Charge-Spin-Orbital-Lattice “Chimera” of correlated electron science [1], which emphasizes the interrelated degrees of freedom. The Chimera is a beast from Greek mythology.

Multiferroic materials

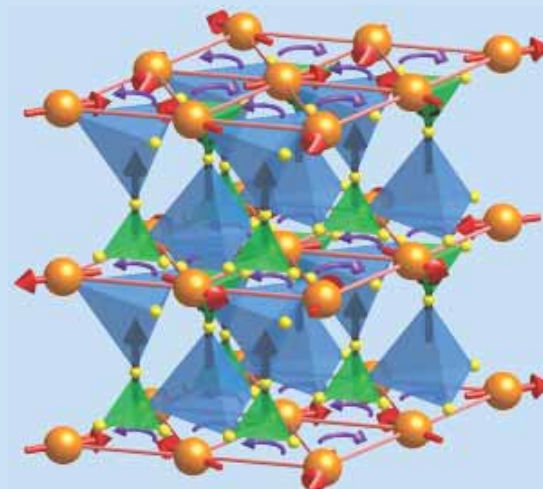


Fig. V.i1. The multiferroic material $\text{RbFe}(\text{MoO}_4)_2$.

Order parameters that can be switched between an “up” and “down” states are called ferroic. If a material has simultaneously two ferroic order parameters, then it is called multiferroic. This definition has been somewhat relaxed in the past few years, and it is now customary to call any material multiferroic that shows spontaneous magnetic order and ferroelectricity [24]. An example is when a material has a spontaneous dipole moment and antiferromagnetic order. Because multiple order parameters are almost always coupled, multiferroic materials hold the promise that the electric dipole moment can be manipulated magnetically, or that ferromagnetic magnetization can be manipulated electrically, with exciting possibilities for novel device applications involving ultrafast switching.

There are different mechanisms that can lead to the simultaneous presence of ferroelectricity and magnetic order. One of the simplest is when ferroelectricity emerges directly from magnetic order. This can happen when magnetic order breaks the symmetry in such a way that a switchable electric polarization occurs. There are other mechanisms, such as geometric ferroelectrics and lone-pair ferroelectrics, which are as yet not fully understood. The most interesting and promising cases are materials in which ferroelectricity arises from charge frustration which is coupled with magnetism (see Fig. V.i1). This can lead to a large electric polarization and strong coupling effects at high temperature. There are only few such electronic ferroelectrics known to date, and their physics is presently under intense investigation.

Correlated electron phases

A prominent class of correlated electron materials are transition-metal oxides (TMO), based on the perovskite crystal structure, with transition-metal ions in octahedral environments. Figure V.2 indicates, using the example of Mn^{3+} and Mn^{4+} , the splitting of the 3d-electron energy levels caused by the octahedral crystal-field and the Jahn-Teller distortion (see also Chapters I and II). Note that a large correlation energy causes both ions to be in the Hund's rule "high-spin" state.

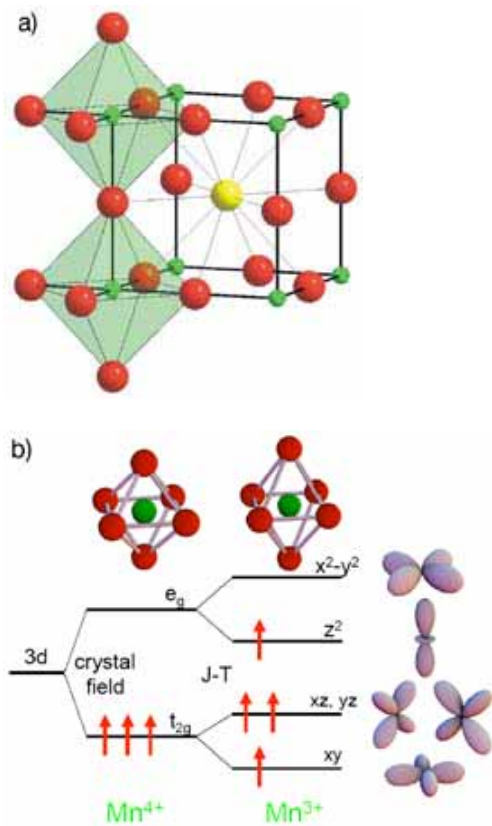


Fig. V.2. a) The undistorted ABO_3 perovskite structure, showing the green transition-metal ions (B) at the center of O^{2-} octahedra. b) Energy splitting of the 3d-electron states in an octahedral crystal field (Mn^{4+}) and due to the Jahn-Teller effect (Mn^{3+}).

TMO materials show ordered phases of the charge, spin and orbital degrees of freedom; Figure V.3 indicates the different unit cells which occur in the MnO_2 planes of the manganite $\text{La}_{0.5}\text{Sr}_{1.5}\text{MnO}_4$ [3].

An example of the variety of phases which arise in TMOs is that of the manganite $\text{La}_{1-x}\text{Ca}_x\text{MnO}_3$ (LCMO) (see Fig. V.4 a) [4]. As the electron concentration is increased by Ca doping, the stable low-temperature phase changes from antiferromagnetic insulator (AFI), to ferromagnetic insulator (FMI), to ferromagnetic metal (FMM) and finally

to a charge-orbitally ordered state (CE). In the FMM phase of LCMO, colossal magnetoresistivity is associated with the formation of nanoscale polarons that develop at elevated temperature, which, around $x \approx 0.3$, show correlations with a wave-vector $\approx (\frac{1}{4}, \frac{1}{4}, 0)$ [3]. These correlations develop into long-range order at $x \approx 0.5$, where equal numbers of Mn^{3+} and Mn^{4+} form a charge- and orbitally-ordered structure known as "CE". Above the magnetic ordering temperature, a correlated polaron glass phase is formed, with a weakly temperature-dependent correlation length in the nanometer range. At still higher temperature, these static polarons become purely dynamic in character, as evidenced by inelastic neutron scattering (see Fig. V.4 b).

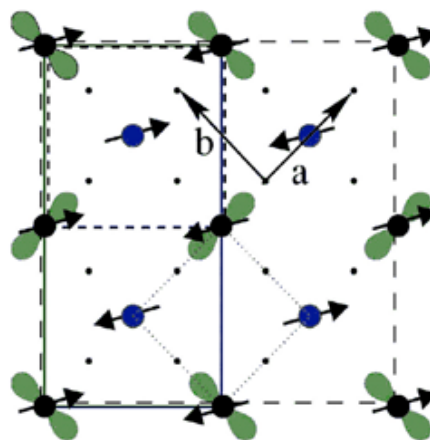


Fig. V.3. The unit cells in the MnO_2 planes of the layered material $\text{La}_{0.5}\text{Sr}_{1.5}\text{MnO}_4$ [3]. The small dots are O^{2-} , and the large black and blue dots represent Mn^{3+} and Mn^{4+} ions, respectively. One distinguishes the $I4/mmm$ crystallographic (dots), the charge (small dashes), the orbital (solid) and the magnetic (large dashes) unit cells.

Another famous example of correlated-electron TMOs are the cuprates showing high-temperature superconductivity. The crystal structure and (schematic) phase diagram for $\text{YBa}_2\text{Cu}_3\text{O}_{7-x}$, a hole-doped superconductor, are shown in Figure V.5. CuO_2 planes in the layered, oxygen-deficient perovskite structure are responsible for superconductivity. Besides the superconducting phase (SC), of particular interest in the "underdoped" regime, are the spin-glass (SG) and pseudo-gap regions. Here there is evidence that static and dynamic "stripes" occur, with characteristic arrangements of Cu-ion charge and spin on the nanometer scale [5].

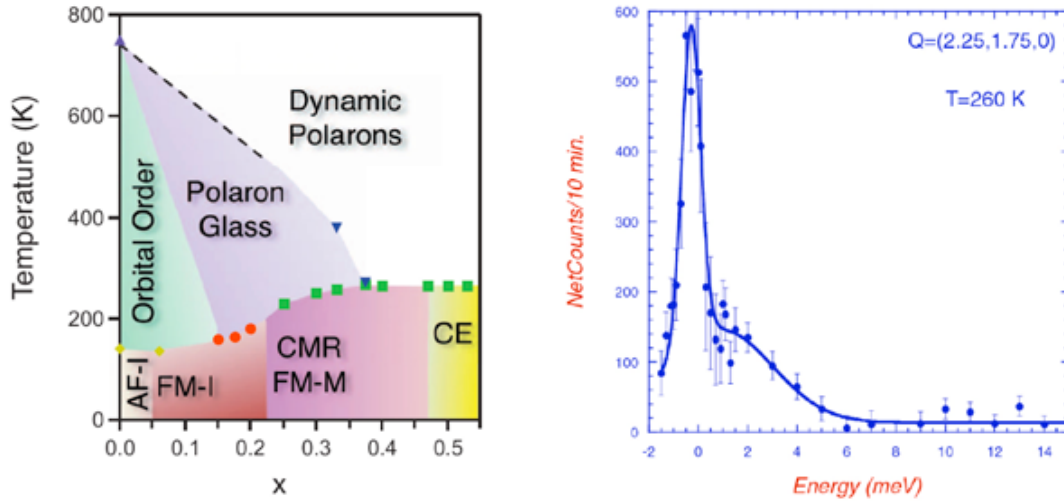


Fig. V.4. a) The phase diagram of $\text{La}_{1-x}\text{Ca}_x\text{MnO}_3$, as a function of the electron doping x [4]. The antiferromagnetic insulator (AFI) and the ferromagnetic insulator (FMI) and metal (FMM) phases show magnetic order. Charge and orbital order occur in the FMI and CE phases, while orbital order is also found near $x=0$ above 140 K. Disordered polarons of the CE-type occur above the magnetic ordering temperatures, with spatial correlations on the nanometer scale. b) In the “dynamic” region, inelastic neutron scattering shows the polarons to be fluctuating on the ps time-scale, as evidenced by the inelastic shoulder at the right of the $E=0$ elastic scattering peak.

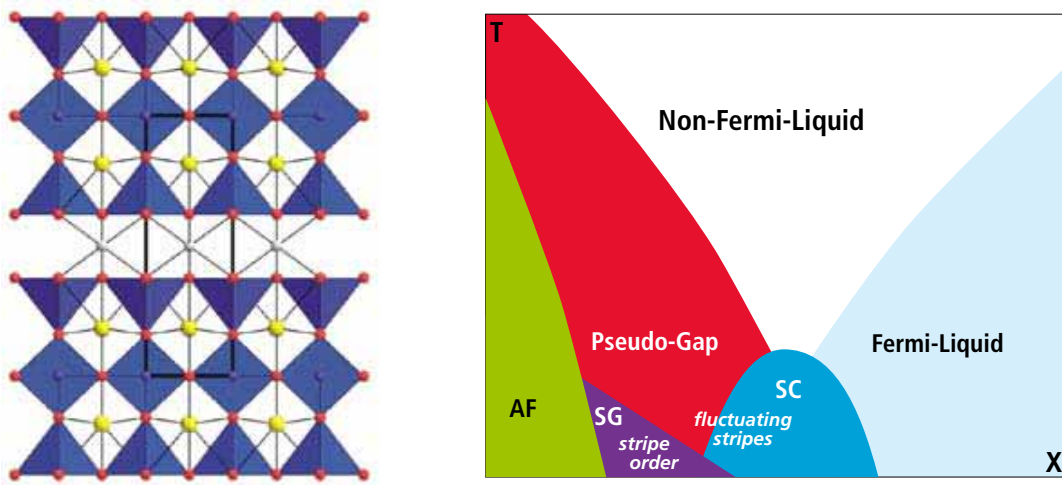


Fig. V.5. a) The layered perovskite structure of $\text{YBa}_2\text{Cu}_3\text{O}_{7-x}$, with the superconducting CuO_2 planes perpendicular to the plane of the figure. b) The schematic phase diagram of hole-doped high-temperature superconductors with, among others, the antiferromagnetic (AF), spin-glass (SG) and superconducting (SC) phases.

X-ray methods in correlated electron science

The relevance for correlated-electron materials of ps dynamics at the nanoscale, together with strong interaction of X-ray photons with all four of the C-S-O-L degrees of freedom, promises important applications of the SwissFEL. To begin the discussion of relevant X-ray techniques, we consider the Hamiltonian describing an X-ray photon field interacting with the electrons in the sample [6, 7]. For the moment, we treat a single free electron, without spin:

$$H = \frac{(\vec{p} - e\vec{A})^2}{2m} + H_{\text{radiation}},$$

where $H_{\text{radiation}} = \sum_{\epsilon, \vec{k}} \hbar \omega_k \left(a_{\epsilon \vec{k}}^\dagger a_{\epsilon \vec{k}} + \frac{1}{2} \right)$ describes photons in the radiation field, with wavevector \vec{k} and polarization ϵ . Expanding the expression for H , we obtain:

$$\begin{aligned} H &= H_{\text{electron}} + H_{\text{interaction}} + H_{\text{radiation}} \\ H_{\text{electron}} &= \frac{p^2}{2m} \\ H_{\text{interaction}} &= \frac{e^2 A^2}{2m} - \frac{e\vec{A} \cdot \vec{p}}{m} \equiv H_1 + H_2 \end{aligned}$$

The interaction Hamiltonian, $H_{\text{interaction}}$, is responsible for producing transitions from an initial state $|i\rangle$ to a final state $|f\rangle$ of the combined system of X-rays and sample. According to Fermi's Golden Rule, the transition rate is given by:

$$w = \frac{2\pi}{\hbar} \left| \langle f | H_1 | i \rangle + \sum_n \frac{\langle f | H_2 | n \rangle \langle n | H_2 | i \rangle}{E_0 - E_n + \hbar \omega_k} \right|^2 \delta(\hbar \omega_k - \hbar \omega_{k'}) - (E_f - E_0)$$

Here we are interested in “photon-in” (k) to “photon-out” (k') transitions – thus we include only those terms which are quadratic in the vector potential A . We disregard the linear terms, which are responsible for photoemission. The transition rate is proportional to the square of the “scattering factor”, $w \propto |S(\vec{Q}, \omega)|^2$, which, in turn, is a function of the momentum and energy transfers $\vec{Q} = \vec{k}' - \vec{k}$ and $\omega = \omega_{k'} - \omega_k$.

Consider now the following cases:

Hard X-ray diffraction

If the photon energy $\hbar \omega_k$ is much larger than the excitation energies $E_n - E_0$ of the system, we need only consider the first matrix element in the expression for w :

$$\langle f | H_1 | i \rangle \propto \sum_j \langle 0 | e^{i\vec{Q} \cdot \vec{r}_j} | 0 \rangle = S(\vec{Q}, 0) = F(\vec{Q})$$

where $|0\rangle$ is the ground-state of the system, and where we now sum over *all* the electrons, with coordinates \vec{r}_j . For a crystalline sample, the scattering factor $F(\vec{Q})$, is written

$$F(\vec{Q}) = \sum_{l,m,n} e^{i\vec{Q} \cdot \vec{R}_{lmn}} \sum_{i=1}^l e^{i\vec{Q} \cdot \vec{r}_i} f_i(\vec{Q}),$$

i.e., as a lattice sum over the unit cells and a “structure-factor” sum over the l atoms per unit cell. The quantity $f_i(\vec{Q})$ is known as the atomic scattering factor. For a perfect crystal, the lattice sum dictates that F is non-zero only if $\vec{Q} = \vec{G}_{hkl}$, a reciprocal lattice vector. This is the condition for Bragg scattering, which, using the relations $Q = \frac{4\pi \sin \theta}{\lambda}$ and $G = \frac{2\pi}{d}$, can be expressed as Bragg's law: $\lambda = 2d \sin \theta$. We thus see that diffraction at the Bragg angle θ is possible when the X-ray wavelength λ is shorter than twice the lattice-plane spacing ($2d$). The scattered intensity at the Bragg condition is proportional to $|F(\vec{Q})|^2$. The sensitivity of the Bragg condition to the lattice parameters implies that the diffraction of short X-ray pulses can be used to directly observe lattice phonons.

Soft X-ray resonant diffraction

If the incoming photon energy lies close to an atomic absorption edge, it is the second-order contribution from H_2 which dominates the scattering rate. The case of elastic scattering, $\omega_{k'} - \omega_k = 0$, is treated via an energy-dependent correction to the atomic scattering factor:

$$f_i(\vec{Q}) \Rightarrow f_i(\vec{Q}, \omega) = f_i(\vec{Q}) + \Delta f_i(\vec{Q}, \omega),$$

where the correction term obeys:

$$\Delta f_i \propto \sum_n \frac{\langle 0 | \vec{\epsilon} \cdot \vec{r} e^{i\vec{k} \cdot \vec{r}} | n \rangle \langle n | \vec{\epsilon}' \cdot \vec{r} e^{i\vec{k}' \cdot \vec{r}} | 0 \rangle}{\hbar \omega_k - (E_n - E_0) - i\Gamma}$$

We see that the scattering is sensitive to the electronic structure of the ground- and intermediate states and to the polarization of the incoming and outgoing photons (see Fig. V.6 a). The existence of a “core-hole” in the intermediate state is responsible for introducing the linewidth parameter Γ , representing the lifetime of the state $|n\rangle$.

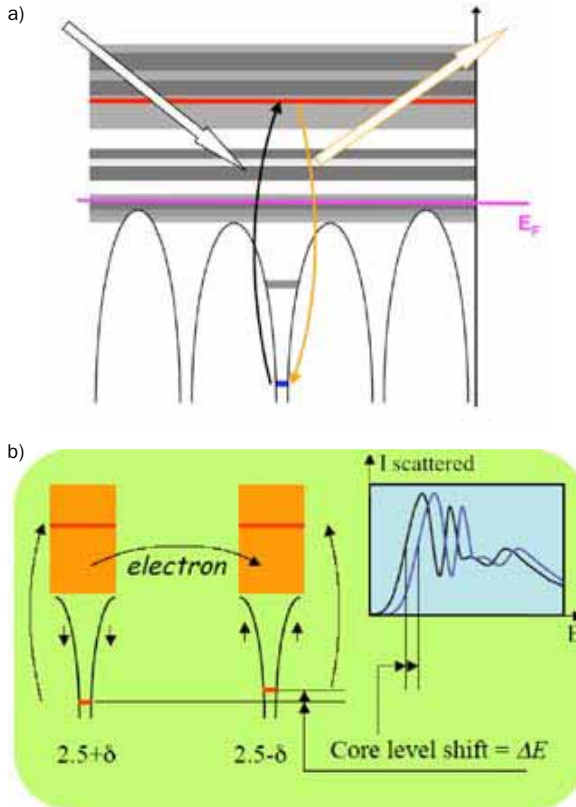


Fig. V.6. a) The resonant elastic scattering process, indicating a virtual transition from an occupied core state (blue) to an unoccupied intermediate valence state (red) [8]. b) A charge-dependent shift in the core-level energy shifts the energy-dependent scattering profile, providing contrast for charge-ordering [9].

For soft X-rays, where the photon wave-vector k is significantly larger than the atomic dimensions, one can expand the exponentials into dipole, quadrupole and octupole terms:

$$\langle 0 | \vec{\epsilon} \cdot \vec{r} e^{i\vec{k} \cdot \vec{r}} | n \rangle \approx \langle 0 | \vec{\epsilon} \cdot \vec{r} | n \rangle + i \langle 0 | (\vec{\epsilon} \cdot \vec{r}) (\vec{k} \cdot \vec{r}) | n \rangle - \langle 0 | (\vec{\epsilon} \cdot \vec{r}) (\vec{k} \cdot \vec{r})^2 | n \rangle.$$

The product of two such matrix elements yields a hierarchy of tensorial terms: dipole-dipole (rank 2), dipole-quadrupole (rank 3), quadrupole-quadrupole (rank 4), etc. These tensorial components can be enhanced by a suitable choice of polarizations and scattering vector. In TMOs, interesting resonances are the L_2 and L_3 transition-metal edges, which connect filled $2p$ and unfilled $3d$ states. The corresponding photon wavelength, approximately one nm, allows the observation of resonant soft-X-ray diffraction, and the dependence of the matrix elements on valence-band electronic structure produces superstructure Bragg reflections, corresponding, for example, to *orbital-ordering* in the correlated electron material. And when circularly-polarized X-rays are used, XMCD-contrast (see Chapter I) makes *mag-*

netic order visible. Finally, a charge-dependent shift of the initial core level shifts the energy-dependent resonant scattering profile (see Fig. V.6 b), providing a *charge-order* contrast.

One should note that soft-X-ray resonant diffraction is not easy: it requires scanning of the incoming photon energy, a multi-axis diffractometer in vacuum, and perhaps polarization-analysis of the scattered beam.

With the SwissFEL, a pump-probe resonant diffraction experiment can follow, for example, the melting of orbital order by a laser pump pulse and its recovery at later times. Its short pulses and flexible energy tuning, particularly near 1 nm wavelength, make the SwissFEL an ideal source for such investigations of TMO correlated electron materials. A particularly interesting application of pump-probe resonant elastic scattering at the SwissFEL would be the time-resolved study, at the nanometer scale, of so-called “orbitons”, wave-like excitations of the orbitally-ordered phase, in manganites (see Fig. V.7).

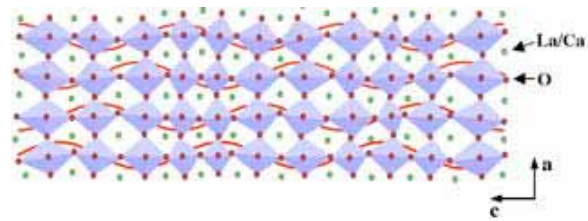


Fig. V.7. The proposed structure of an “orbiton”, a wave-like excitation of the orbitally-ordered state in manganites. Optical pump-probe experiments provide evidence of its existence, with an oscillation period in the range of 10–50 ps [10]; resonant diffraction at the SwissFEL would allow its detailed study at the nanoscale.

Resonant inelastic X-ray scattering (RIXS)

We now lift the restriction to elastic scattering, by allowing $\omega = \omega_{k'} - \omega_k$ to be non-zero, requiring, in general, energy analysis of the scattered photons. A schematic of the RIXS process is shown in Figure V.8.

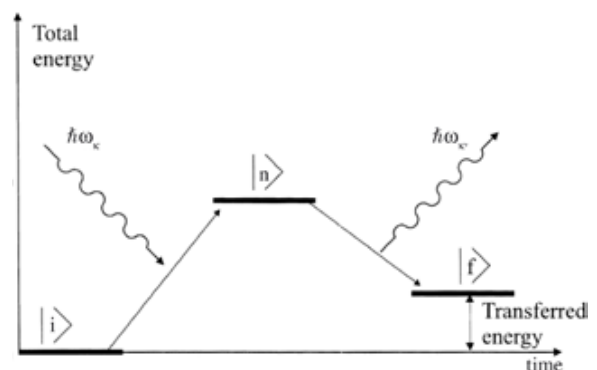


Fig. V.8. A schematic of the resonant inelastic X-ray scattering (RIXS) process.

A single-shot RIXS spectrometer

When performing resonant inelastic X-ray scattering (RIXS), the scattered intensity as a function of outgoing photon energy $E_{\text{out}} = \hbar\omega_k'$ is normally acquired for particular settings of the incoming energy $E_{\text{in}} = \hbar\omega_k$ by the monochromator. This is a procedure which is incompatible with single-shot operation at the SwissFEL. One would like to instantaneously obtain a two-dimensional plot of the scattered intensity as a function of $E_{\text{in}}, E_{\text{out}}$.

A method of performing single-shot RIXS has been proposed by V. Strocov [25] (see Fig. V.i2). The SwissFEL pulse is dispersed vertically by a monochromator (upper right in the figure) and brought to a line focus on the (homogeneous) sample. Scattered light corresponding to the various incoming photon energies is then focused to a vertical line and dispersed in E_{out} horizontally onto a CCD detector. The result is the desired two-dimensional plot.

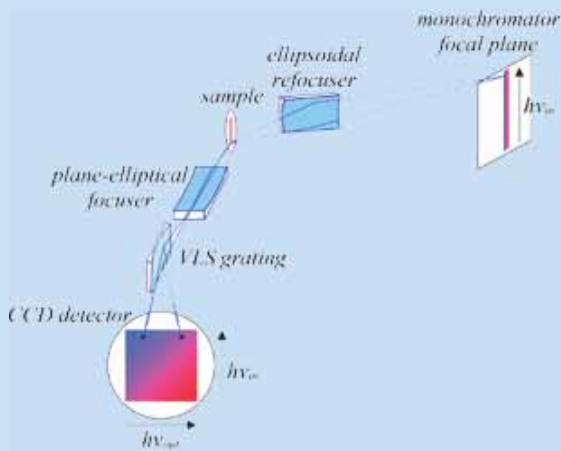


Fig. V.i2. Proposal for a doubly-dispersive RIXS spectrometer, suitable for use at the SwissFEL [25]. Advantages of this design include higher efficiency and compatibility with single-shot operation. The “VLS grating” has variable line spacing.

The scattering rate is now given by:

$$w = \frac{2\pi}{\hbar} \sum_f \left| \sum_n \frac{\langle f | H_2 | n \rangle \langle n | H_2 | i \rangle}{E_0 - E_n + \hbar\omega_k + i\Gamma} \right|^2 \delta((\hbar\omega_k - \hbar\omega_k') - (E_f - E_i)).$$

Note the following features: a) The sensitivity to photon polarization and valence electronic states seen in resonant elastic scattering is also present for RIXS. b) Although there exists a (virtual) core-hole in the intermediate state, evidenced by the Γ -term in the denominator, because there is no hole in the final state, the ω_k' resolution of RIXS can in principle be infinitely good – as evidenced by the energy δ -function. c) Low-energy collective excitations, such as phonons, plasmons, spinwaves, etc., of the sample are accessible with RIXS, since what is measured is the energy *difference* between the incoming and outgoing photons. And since *two* photons are involved, the dipole selection rule $\Delta\ell = \pm 1$ does not apply, such that a $d \rightarrow d$ transition can be observed (see Fig. V.9 a). d) Although performed at resonance, RIXS is a low-efficiency process: In resonant elastic

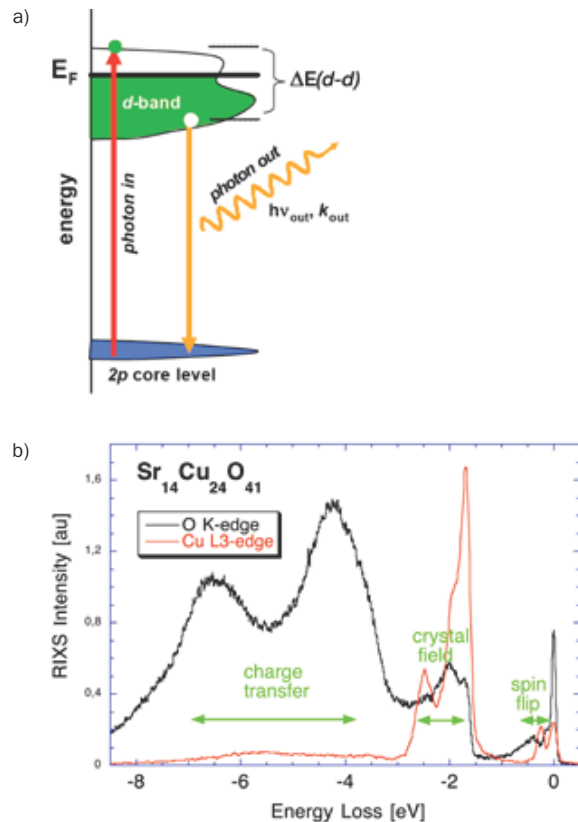


Fig. V.9. a) A $d \rightarrow d$ transition observable with RIXS, without restrictions from dipole selection rules. In this way, for example, the crystal-field or Jahn-Teller splitting of the d -orbitals of a $3d$ -transition-metal ion can be measured. b) Experimental RIXS spectra for $\text{Sr}_{14}\text{Cu}_{24}\text{O}_{41}$, taken at the oxygen K -edge and at the Cu L_3 -edge [11], showing structures due to the transfer of charge between atoms, the Cu crystal-field splitting and collective spin-flip excitations.

scattering, the excitation of each of the N scattering atoms can be coherently added, since there is a unique final state. This results in a scattering intensity proportional to N^2 . For RIXS, because the virtual excitation of different atoms leads to different final states, the contributions add incoherently, resulting in an intensity proportional to N [7].

Performing RIXS is an extremely challenging undertaking, due to the low scattered intensity and because of the necessity of performing an energy (and scattering-angle) analysis of the scattered radiation. For pump-probe RIXS experiments at the SwissFEL, it would therefore be particularly interesting to realize a single-shot mode of measuring, either in the frequency (see Infobox) or in the time (ditto) domains.

The intermediate scattering function

At the beginning of this Section, we saw how the transition rate for X-ray photon scattering, with momentum transfer \vec{Q} and energy transfer $\hbar\omega$, is related to the scattering function $S(\vec{Q}, \omega)$. This function shows peaks as a function of ω corresponding, for example, to long-lived oscillations (quasiparticles), such as phonons, spin-waves, etc. But finite lifetime effects will broaden these quasiparticle peaks, and in the limit of strong damping, it may be advantageous to observe the time-dependent fluctuations of the system directly – i.e., to measure instead the so-called time-domain or intermediate scattering function [12]:

$$S(\vec{Q}, t) = \int_{-\infty}^{\infty} S(\vec{Q}, \omega) e^{i\omega t} d\omega.$$

The intermediate scattering function basically provides the correlation time (over which $S(Q, t)$ decays to the value $1/e$) for the equilibrium fluctuations of a system, as a function of the fluctuation length scale $1/Q$. By monitoring the scattered intensity $I(\theta, t)$ at a particular scattering angle 2θ (related to the momentum-transfer by $Q = 4\pi \sin\theta/\lambda$), one has access to $S(Q, t)$ via the intensity correlation function $g_2(\theta, t)$ and the “Siegert relation” [13]:

$$g_2(\theta, t) \equiv \frac{\langle I(\theta, t) I(\theta, t + \tau) \rangle}{\langle I(\theta, t) \rangle^2} = 1 + |S(\vec{Q}, t)|^2.$$

A measurement of $I(\theta, t)$ on the ultrafast time scale, pertinent to correlated electron materials, would require reading out a detector at an impossible rate of GHz -THz. Two realistic alternatives, however, which are well-suited to the characteristics of the SwissFEL, are provided by the “split-pulse” and “Mössbauer filter foil” techniques and are described in Infoboxes.

RIXS in the time-domain

A principal drawback of conventional RIXS measurements is the necessity of a fine energy-analysis of the scattered radiation, resulting in a significant loss of intensity. It has been suggested [26] that the ultrashort pulses of the SwissFEL could be used to effectively perform RIXS in the time-, instead of the energy domain.

If a suitable non-linear (NL) optical medium for soft X-rays could be developed, one could imagine performing X-ray heterodyne spectroscopy: A SwissFEL pulse is split into two pulses. One of these is scattered by the sample, causing the creation, by inelastic scattering, of multiple frequency components. This multi-frequency pulse is then recombined with the unscattered reference pulse in the NL-medium, where sum and difference frequencies are generated. The difference frequencies appear at the detector as slow oscillations, corresponding to the inelastic energy loss or gain in the sample.

Heterodyne spectroscopy is routinely performed with optical pulses, using the frequency-resolved optical gating (FROG) technique (see Fig. V.i.3). Realization of an X-ray FROG will require the transform-limited pulses which a seeded SwissFEL will provide.

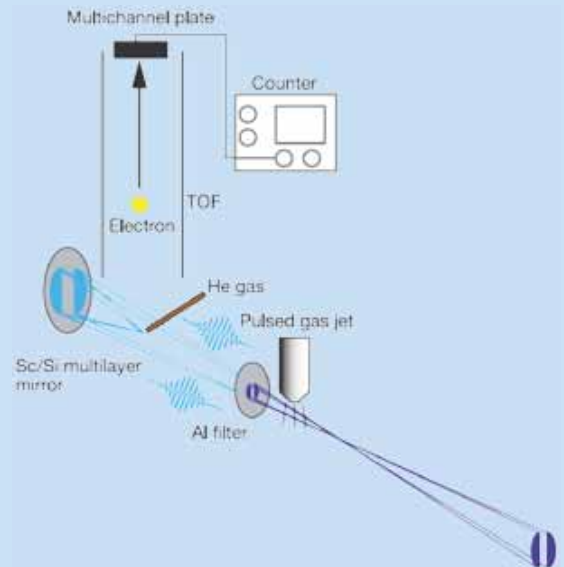


Fig. V.i.3. A FROG device, using two-photon ionization in He gas as a NL mixer, which operates at a photon energy of 28 eV [27].

Split-pulse XPCS

X-ray photon correlation spectroscopy measures the time-correlation function of the coherently-scattered radiation intensity from a fluctuating sample:

$$g_2(\tau) = \frac{\langle I(t)I(t+\tau) \rangle}{\langle I(t) \rangle^2}.$$

Since this requires a detector bandwidth which exceeds that of the fluctuations, one is generally limited to times τ longer than 10 nsec.

The use of the SwissFEL to probe ps-dynamics will require a different approach – “split-pulse XPCS” (see Fig. V.i4) [11]. Here a single SwissFEL pulse is split and delayed, producing a pair of pulses with tunable separation τ . The 2d-detector then registers a double-exposure speckle pattern, and the speckle contrast will decrease when τ exceeds the fluctuation correlation time τ_c .

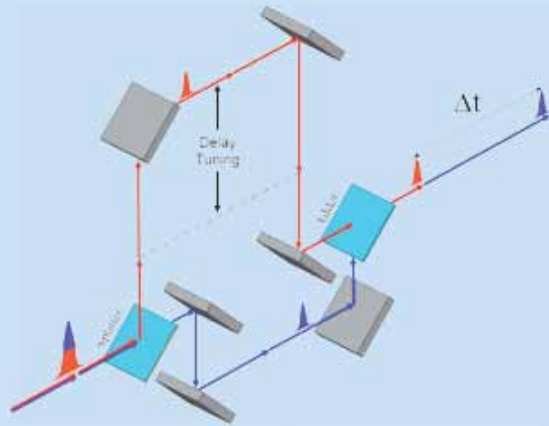


Fig. V.i4. A conceptual “split-and-delay” unit for XPCS at the SwissFEL [28].

That one indeed can measure $g_2(\tau)$ with split-pulse XPCS has been demonstrated by Gutt et al. [29]:

The double exposure delivers the intensity $S(\tau) = I(t) + I(t + \tau)$, and the speckle contrast is given by the variance:

$$c_2(\tau) = \frac{\langle S^2(\tau) \rangle - \langle S(\tau) \rangle^2}{\langle S(\tau) \rangle^2}$$

We note that:

$$\langle S^2(\tau) \rangle = 2\langle I^2 \rangle + 2\langle I(t)I(t+\tau) \rangle$$

$$\langle S(\tau) \rangle^2 = 4\langle I \rangle^2$$

and that, for a fully coherent beam,

$$\langle I^2 \rangle - \langle I \rangle^2 = \langle I \rangle^2.$$

We thus obtain:

$$c_2(\tau) = \frac{\langle I(t)I(t+\tau) \rangle}{2\langle I \rangle^2} = \frac{g_2(\tau)}{2}.$$

The Mössbauer filter-foil technique

The Mössbauer filter-foil technique provides an alternate method for measuring the intermediate scattering function [30]. Foils containing a stable Mössbauer isotope are placed in front of and behind the scattering sample and, at time $t=0$, a resonant SwissFEL pulse excites the isotope. The subsequent decay is then monitored by the total transmitted counting rate, measured in the forward direction (see Fig. V.i5).

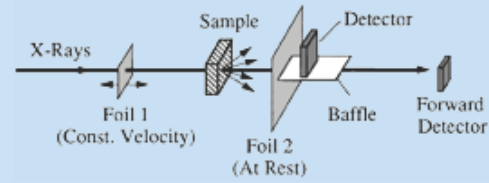


Fig. V.i5. The Mössbauer filter-foil method for measuring the intermediate scattering function $S(Q,t)$ [30].

Denoting by $\rho(Q,t)$ the spatial Fourier transform of the electron density in the sample at the time t , the intermediate scattering function is given by $S(Q,t) = \langle \rho(Q,0)\rho^*(Q,t) \rangle$. Further, we let $|g(t)|^2$ denote the decay probability of the Mössbauer isotope a time t after excitation.

The signal $I(t)$ at the detector is the square of the coherent sum of the probability amplitudes for a) radiation scattered by the sample at time zero and emitted by the nuclei of the second foil at time t and b) emitted by the first foil at time t and directly scattered into the detector:

$$\begin{aligned} I(t) &= \langle |\rho(Q,0)g(t) + g(t)\rho(Q,t)|^2 \rangle \\ &= 2|g(t)|^2 [|\rho(Q,0)|^2 + R_e S(Q,t)] \end{aligned}$$

From this expression, the intermediate scattering function can be extracted.

By far the most popular Mössbauer isotope is ^{57}Fe , with a resonant energy of 14.4 keV and an excited state lifetime of 141 ns. An upgrade option for the SwissFEL will make this photon energy accessible with the fundamental undulator radiation, as well as still higher energies using XFEL harmonics [31].

Advantages of the filter-foil method in combination with the SwissFEL are: a) extremely intense X-ray pulses with zero background during the nuclear decay, and b) measurements of $S(Q,t)$ for times far longer than those accessible with the split-pulse XPCS method. (The maximum feasible split-pulse delay will be ns for hard X-rays and tens of ps for soft X-rays.)

Origin of the metal-insulator transition in TaS₂

A signature feature of correlated electron materials is the occurrence of metallic and insulating phases, and of transitions between them. These metal-insulator transitions (MIT), can be caused by temperature, pressure, doping, or by other external influences. Two possible mechanisms for such an MIT are a) the Peierls instability and b) the Mott-Hubbard transition.

The Peierls instability

The Peierls instability [14] causes a metal to become an insulator by the action of a lattice distortion which doubles the crystal unit cell (see Fig. V.10). The energy cost incurred by the elastic distortion is more than compensated by a lowering of the electronic energy, due to the opening of a Peierls gap at the electronic Fermi level. Note that the situation is similar to that for the *spin* Peierls effect, discussed in Chapter I, where it is the lowered *magnetic* energy for spin dimers which drives the lattice distortion. Both the charge Peierls instability and the spin Peierls effect are intimately connected to the motion of lattice atoms, hence the relevant time scale will be that of lattice vibrations (i.e., 10–100 fs).

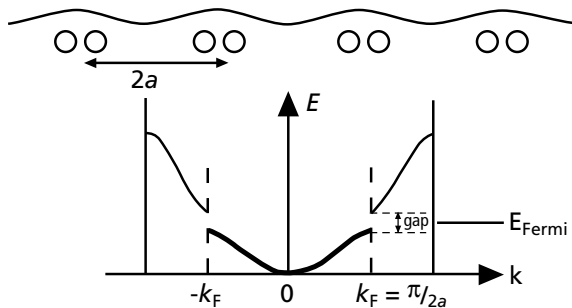


Fig. V.10. The Peierls instability [14]. Under special circumstances, it may become energetically favorable for a metallic crystal to undergo a spontaneous lattice distortion, forming atomic dimers, and doubling the crystal unit cell. In reciprocal space, the Brillouin zone is halved, and a gap opens at the Fermi level, causing a lowering of the electronic energy, which more than compensates for the cost in elastic energy. The presence of the gap causes the material to become insulating.

The Mott-Hubbard transition

A purely electronic mechanism for producing a metal-insulator transition results from the correlation physics described by the Hubbard model (see Infobox). In this model, the motion of electrons among lattice sites is governed by the two parameters U and W . The on-site

Coulomb repulsion U is the energy cost incurred when a lattice site is simultaneously occupied by two electrons. The bandwidth W measures the tendency of electrons to minimize their kinetic energy by delocalizing among the lattice sites. As shown in the Infobox, a large U/W ratio favors electron localization and hence the insulating state, while a small value for this ratio causes the electrons to become itinerant and the material to become a conductor. Therefore, at some intermediate value of U/W , an originally half-filled conduction band will split into two bands, by the creation of a Hubbard correlation gap (of order U) in the electron density of states (see Fig. V.11). Since no atomic motion is involved, the relevant time scale of the Mott-Hubbard transition is that of the electronic motion, i.e., 10 fs and faster.

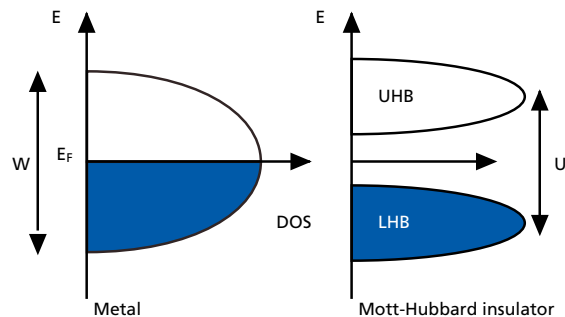


Fig. V.11. The Mott-Hubbard metal-insulator transition, as predicted by the Hubbard model, is a purely electronic effect, which opens a gap at the Fermi level, splitting the half-filled valence band into a filled “lower Hubbard band” (LHB) and an unfilled “upper Hubbard band” (UHB).

The characteristic time scales of the “slow” Peierls instability and the “fast” Mott-Hubbard transition are compared with electronic and lattice motions in Figure V.12.

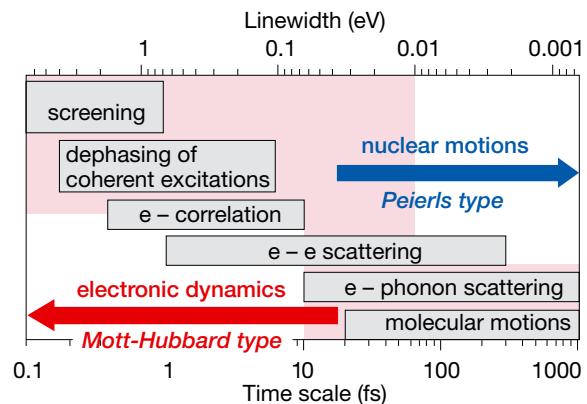


Fig. V.12. Characteristic time scales involved in metal-insulator transitions of the Peierls and Mott-Hubbard types. A Mott-Hubbard transition, being purely electronic in nature, is inherently faster than a Peierls transition, which is tied to the slower motion of the lattice atoms [15].

The Hubbard Model

The Hubbard Model [32] is the simplest model of interacting particles in a lattice and the starting point of many descriptions of correlated electron systems. It is based on the “Hubbard Hamiltonian”:

$$H = -W \sum_{\langle ij \rangle \sigma} c_{j\sigma}^\dagger c_{i\sigma} + U \sum_i n_{i\uparrow} n_{i\downarrow}$$

Where the operators $c_{j\sigma}^\dagger$ and $c_{i\sigma}$ are electron creation and annihilation operators, $n = c^\dagger c$ is the number operator, and the sums run over the spin directions $\sigma = \uparrow$ and \downarrow and the N lattice sites of the model. $\langle ij \rangle$ implies neighboring lattice sites. The principal parameters of the model are U and W , the on-site Coulomb repulsion and the electron bandwidth (or hopping rate), respectively. Let us consider two limiting cases [33]:

a) Static electrons ($W = 0$)

It is now enough to take into account a single site, and the possible states are $\{|0\rangle, |\uparrow\rangle, |\downarrow\rangle, |\uparrow\downarrow\rangle\}$, i.e., empty, a single spin up, a single spin down, or doubly-occupied. We calculate the partition function Z and the thermally-averaged site occupancy $\langle n \rangle$:

$$Z = \sum_{\alpha} \langle \alpha | e^{-\beta(H - \mu n)} | \alpha \rangle = 1 + e^{\beta\mu} + e^{\beta\mu} + e^{-\beta(U + 2\mu)}$$

$$\langle n \rangle = \frac{1}{Z} \sum_{\alpha} \langle \alpha | (n_{\uparrow} + n_{\downarrow}) e^{-\beta(H - \mu n)} | \alpha \rangle = \frac{1}{Z} [0 + e^{\beta\mu} + e^{\beta\mu} + 2e^{-\beta(U + 2\mu)}]$$

$$= \frac{2(e^{\beta\mu} + e^{-\beta(U + 2\mu)})}{1 + 2e^{\beta\mu} + e^{-\beta(U + 2\mu)}}$$

where $\beta = 1/k_B T$, and $\mu \equiv \frac{\partial E}{\partial n}$ is the chemical potential. Plotting $\langle n \rangle$ as a function of μ (Fig. V.i6) we find that at the condition for half-filling, $\langle n \rangle = 1$, the energy required to add an electron to the system changes by U . It is this “Hubbard gap” which implies an *insulating* behavior.

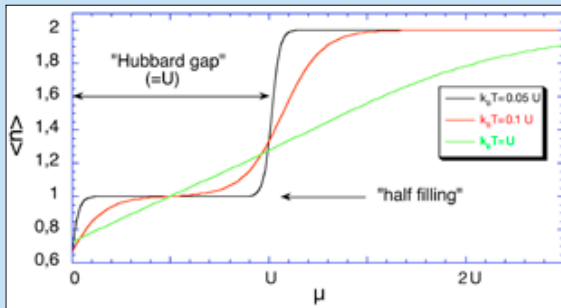


Fig. V.i6. Average site occupancy $\langle n \rangle$ vs. the chemical potential μ , for the Hubbard model without electron hopping ($W = 0$). The jump in μ by the value U at half-filling implies the existence of an energy gap, and hence insulating behavior.

b) Non-interacting electrons ($U = 0$)

In this case, it is convenient to use the reciprocal-space representation of the electron operators:

$$c_{k\sigma}^\dagger = \frac{1}{\sqrt{N}} \sum_l e^{ik \cdot l} c_{l\sigma}^\dagger,$$

where k takes the values $k_n = 2\pi n/N$, assuming periodic boundary conditions in one dimension. The Hubbard Hamiltonian now has the form:

$$H = \frac{-W}{N} \sum_{k, k' \in \text{BZ}} \sum_{\sigma} e^{ik'} e^{-ik} c_{k\sigma}^\dagger c_{k'\sigma} - 2W \sum_{k\sigma} n_{k\sigma} \cos k,$$

where the last expression follows from performing the lattice sums. The energy levels of this Hamiltonian show a “band” behavior (see Fig. V.i7). As N goes to infinity, we obtain a (gapless) continuum of states, with bandwidth $4W$, which, at half-filling, implies *metallic* behavior.

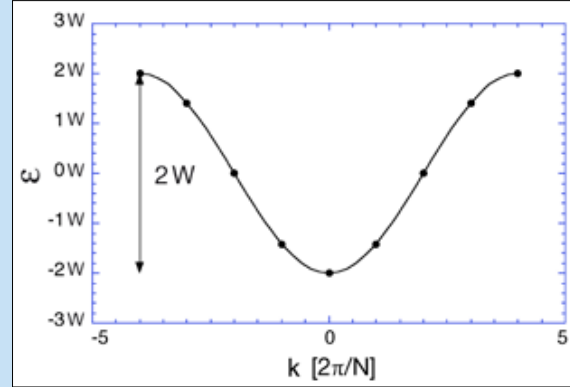


Fig. V.i7. Energy eigenvalues for the Hubbard Hamiltonian for non-interacting electrons ($U = 0$). The points are for a model with $N = 8$ lattice sites. Half-filling of such a continuous band implies conducting behaviour.

We thus find that the Hubbard Hamiltonian describes an insulator, in the case $W = 0$, and a metal, for $U = 0$. Between these two limits, i.e., for intermediate U/W , there must occur a *metal-insulator* transition: the *Mott transition*.

A particularly interesting material in which to investigate the nature of MIT is the 1T phase of the dichalcogenide tantalum disulfide [16]. 1T-TaS₂ consists of S-Ta-S layers which are weakly coupled to one another and which, at room temperature, show an incommensurate charge-density wave (CDW) modulation which serves to split the Ta *d*-electron states into three bands. Since the uppermost of these is half-filled, the material is metallic. Below 180 K, the CDW locks to the lattice, and the resistivity increases by a factor 10. In order to investigate the nature of the MIT in this material, Perfetti et al. performed a pump-probe experiment on an insulating sample at $T = 30$ K. A 1.5 eV laser pump pulse, with a duration of 80 fs, excites hot electrons in the material, and at a variable time later, the time-resolved band structure is probed with angle-resolved photoemission, using 6 eV incoming photons.

Without a pump signal, or with a long (4.5 ps) pump-probe delay, the photoelectron spectra (see Fig. V.13 a), show a pronounced “lower Hubbard band” (LHB), corresponding to the insulating phase. But shortly after the pump, the LHB intensity collapses, and a tail appears, extending far above the Fermi level, demonstrating short-lived metallic behavior. The time-dependent LHB peak height (Fig. V.13 b) shows the ultrafast (fs) nature of the collapse and a continuous recovery of the insulating state. Both these observations argue strongly for a predominantly Mott-Hubbard nature of the MIT in 1T-TaS₂.

Pump-probe photoelectron spectroscopy is not a technique which is particularly well-suited to the SwissFEL, due to the degraded energy resolution from the space-charge felt among the many low-energy photoelectrons which are simultaneously emitted from the sample. But other powerful X-ray methods, in particular photon-in-

photon-out techniques, such as X-ray absorption near-edge spectroscopy (XANES) (see Chapter II) and resonant inelastic X-ray scattering (RIXS), can provide similar information pertinent to electronic band structure effects. These can be performed in a pump-probe arrangement, perhaps even in a single-shot mode (see Infobox), at the SwissFEL.

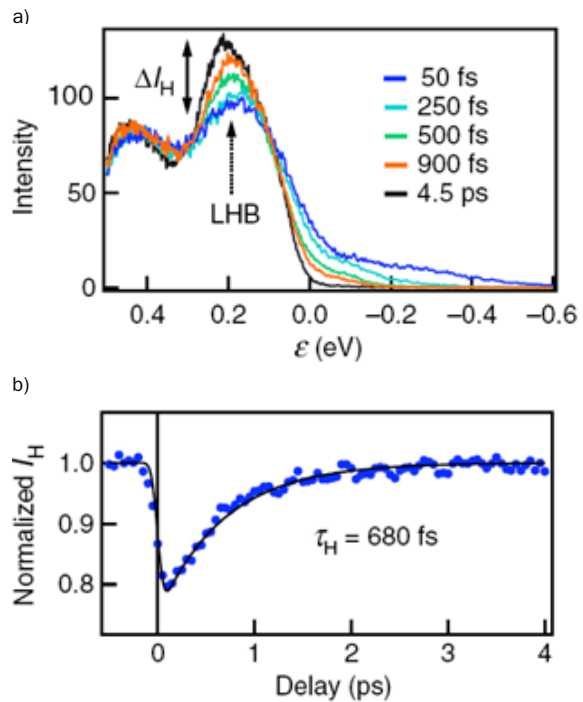


Fig. V.13. Time-resolved pump-probe photoelectron spectroscopy spectra for insulating 1T-TaS₂, showing the ultrafast collapse of the lower Hubbard band and its continuous recovery, with a 680 fs time constant. These observations confirm the Mott-Hubbard nature of the metal-insulator transition in this material [16].

Ultrafast investigations of the electron-phonon interaction

Two of the most important aspects of the correlated electron chimera (Fig. V.1 b) are the electron and lattice degrees of freedom. One example of the electron-lattice interaction is the Peierls instability, discussed in the previous Section. Another is the phonon-mediated mechanism responsible for the creation of Cooper pairs in the BCS theory of (conventional) superconductivity. As evidenced by the following two examples, insight into this important interaction can be won through the use of ultrafast time-resolved measurement techniques.

Electron pump – lattice probe

Let us feed the electron part of the chimera and see how the lattice part reacts. A convenient system for such studies is elemental bismuth, with its interesting crystal structure and lattice dynamics, together with a high atomic number, suitable for hard X-ray scattering. The Bi lattice structure is shown in Figure V.14, where the pair of atoms in each unit cell is indicated, with a separation along the c_3 axis described by the coordinates $x = (0.5 \pm 0.0332) a_0$, where a_0 is the rhombohedral lattice constant. The deviation of these values from $a_0/2$ is due to the Peierls instability discussed earlier. The atoms of a pair vibrate against one another in the A_{1g} optical phonon mode, with a frequency of 2.9 THz.

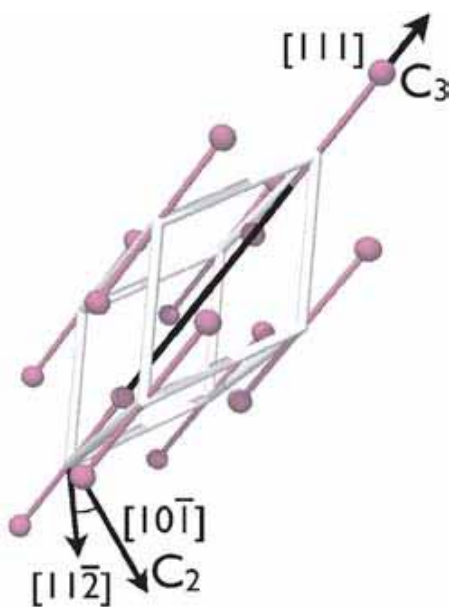


Fig. V.14. The rhombohedral crystal structure of bismuth, showing the positions of the two atoms per unit cell along the three-fold c_3 axis.

An ultrafast laser pulse excites the electronic system in Bi, altering its electronic state and, via the electron-phonon interaction, causes a sudden (i.e., on the electronic time-scale) weakening of the interatomic potential – due to the partial occupation of normally unoccupied anti-bonding orbitals (see Fig. V.15 a). As a result, the (slowly-moving) atoms no longer find themselves at potential minima, and they begin to oscillate coherently in the A_{1g} phonon mode. This displacive excitation oscillation has been *directly* observed with pump-probe hard-X-ray diffraction at the laser-sliced FEMTO beamline at the SLS synchrotron (see Fig. V.15 b) [17]. The dependence of the interatomic potential on the degree of electronic excitation was determined in this experiment by observing a linear drop in the phonon frequency with increasing pulse fluence (inset in Fig. V.15 b), in excellent quantitative agreement with density functional theory calculations (see Fig. V.16 a) [18, 19].

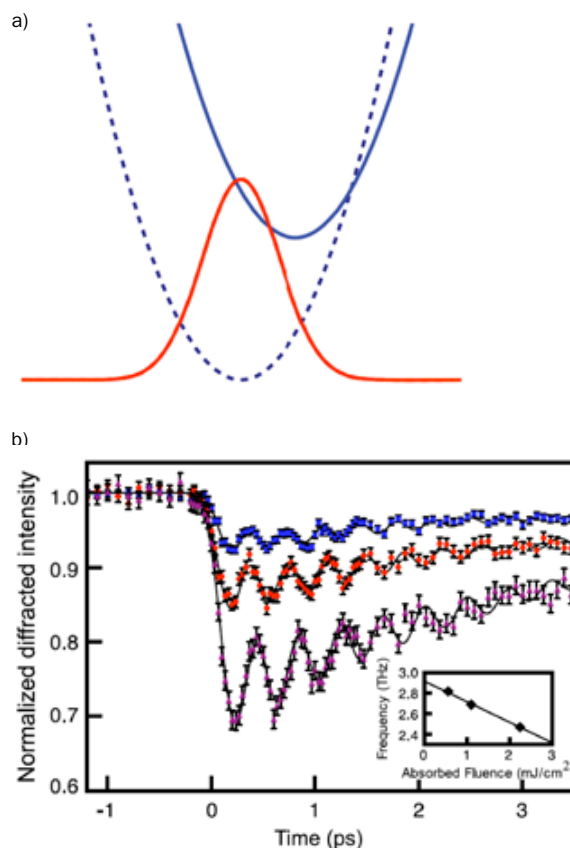


Fig. V.15. a) Displacive excitation of coherent phonons. Upon optical excitation, the interatomic potential becomes shifted and softer (blue dashed \rightarrow blue solid), causing the equilibrium atomic distribution (red) to adapt accordingly. b) The displacive excitation of A_{1g} optical phonons in Bi is performed with a laser pump pulse and probed with hard X-ray diffraction at the FEMTO beamline of the SLS synchrotron [17]. With increasing levels of excitation, a mode softening is observed due to the electron-phonon interaction.

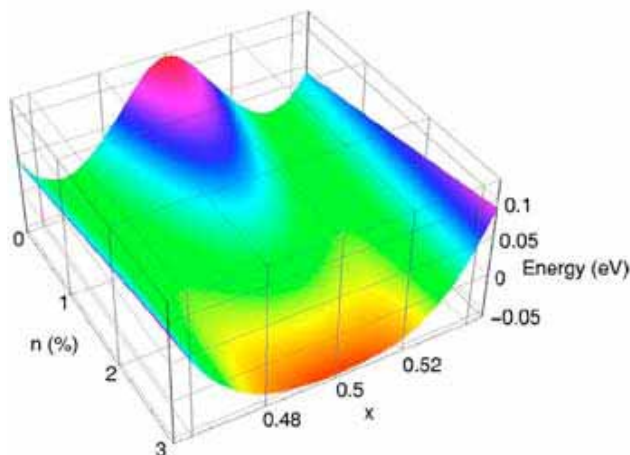


Fig. V.16. The density functional theory prediction of the interatomic potential for the A_{1g} optical phonon mode in Bi, as a function of the atomic coordinates x and the percentage of excited valence electrons n [18]. Note the softening (and symmetrization) which occurs upon increasing excitation.

With the extremely low flux at the laser-sliced FEMTO beamline (see Chapter II), each point in Figure V.15 b requires typically one minute of measurement time; with a more weakly scattering system than bismuth, this time increases by orders of magnitude. The ultra-high peak brightness of the SwissFEL, together with its 100–400 Hz repetition rate and the virtually continuous tuning of the pump-probe delay, will allow detailed investigations of subtle diffraction features from technologically interesting but weakly scattering materials.

Lattice pump – electron probe

We have seen how pumping the electron part of the correlated electron chimera influences the lattice. Can we also perform the inverse? In a purely optical experiment, Rini et al. have excited a particular phonon mode in a perovskite manganite and recorded the effect on the electron system [20].

With the replacement of Pr by the smaller Ca ion, the crystal structure of PrMnO_3 undergoes a local tilt of the MnO_6 octahedra, in the form of an orthorhombic distortion (see Fig. V.17). The electron hopping from Mn to Mn proceeds via an oxygen-mediated super-transfer mechanism, which depends on the orbital overlap between neighboring sites, and this overlap is sensitive to the octahedron tilt. Hence the distortion causes a decrease in the Hubbard model bandwidth parameter W , therefore giving rise to an insulating phase. Indeed, orthorhombic $\text{Pr}_{1-x}\text{Ca}_x\text{MnO}_3$ is insulating over a wide range of compositions and temperatures.

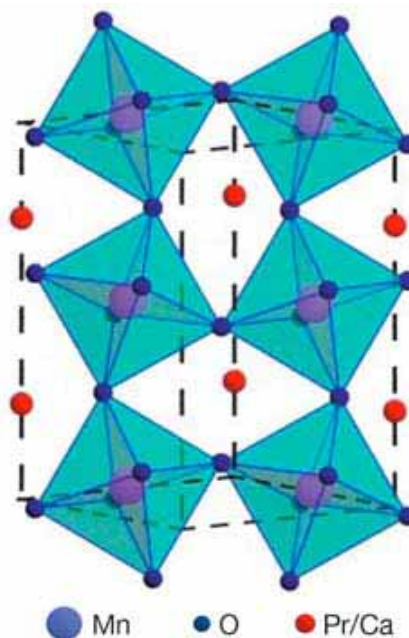


Fig. V.17. Ca-doping causes $\text{Pr}_{1-x}\text{Ca}_x\text{MnO}_3$ to orthorhombically distort, resulting in reduced orbital overlap ($\sim W$) and hence in insulating behavior [20].

At a phonon energy of 71 meV ($\nu = 17.2$ THz, in the mid-IR), the Mn-O distance in $\text{Pr}_{0.7}\text{Ca}_{0.3}\text{MnO}_3$ undergoes a periodic modulation, implying also a modulation in the Hubbard bandwidth W : one can hence envisage a dynamic metal-insulator transition. Rini et al. searched for this effect by performing an IR-pump/visible-probe experiment [20], using the reflectivity of visible light to query the electron system. Their results are shown in Figure V.18. Note that IR-excitation leaves the system in its electronic ground-state.

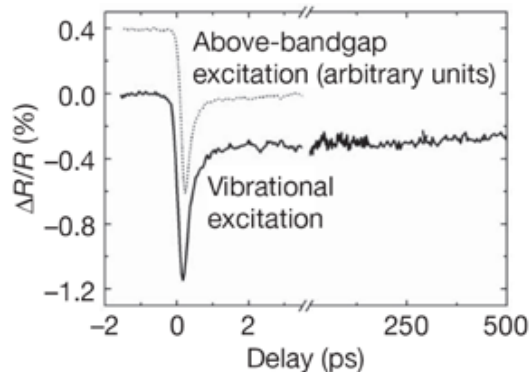


Fig. V.18. The ultrafast change in reflectivity (at 800 nm wavelength) observed after excitation of an IR phonon mode in $\text{Pr}_{0.7}\text{Ca}_{0.3}\text{MnO}_3$ [20]. The effect is very similar to that produced by a visible laser pump (dotted curve), demonstrating that it indeed represents a transient change to a metallic state.

Using the visible reflectivity as a probe of electronic structure implies that one is sensitive only to changes in the immediate vicinity of the Fermi energy. A more complete probe of local and cooperative electronic effects is possible using soft-X-ray spectroscopies such as XANES and RIXS. Hence an IR-pump / soft-X-ray probe experiment at the SwissFEL has great potential for delivering a detailed picture of this type of dynamic MIT. A multitude of further possibilities exist for SwissFEL-based pump-probe investigations of the correlated-electron chimera. We have seen that resonant soft-X-ray diffraction and inelastic scattering are sensitive to charge-, magnetic-, and even orbital-order, and the suggestion has been made that with a suitable pump pulse, one can melt the order and monitor its recovery. One could also excite and detect cooperative excitations of these ordered phases, such as orbitons [10], with resonant frequencies in the THz regime, accessible to the SwissFEL. Another possibility [21] is to use photo-excitation to effectively change the filling number, i.e., “photo-doping” the correlated electron system, and to use the SwissFEL to detect the resulting effects on the lattice and electronic systems.

Complexity in correlated electron materials

In a much cited paper, Dagotto [22] discusses the concept of *complexity* in connection with correlated electron materials. The essential point is that the competition between the charge-spin-orbital-lattice degrees of freedom can lead to the coexistence of different phases which are virtually degenerate in energy, and hence to inhomogeneities and glassy dynamics on a wide range of length and time scales.

A hallmark of such “complex matter”, which exists “at the edge of chaos”, is a non-linear “giant” response to a small perturbation. For example, charge transport in manganite TMOs is different from that in simple metals: an isolated charge may strongly perturb its local environment, inducing the creation of a polaron, which may then attract other polarons to form larger, long-range structures. The manganite phase diagram was shown in Figure V.4 a, with the close juxtaposition of ferromagnetic metal (FM) and antiferromagnetic insulator (AFI) phases. The complexity view of the magnetic-field-induced metal-insulator transition in this material is that a ground state exists with quenched disorder, arising perhaps from lattice distortion accompanying chemical doping (see Fig. V.19 a), with a glassy intermixture of FM and AFI phases (see Fig. V.19 b). A small applied magnetic field is then sufficient to tip the energy balance in favor of the FM phase, causing a giant, percolative change in the bulk conductivity.

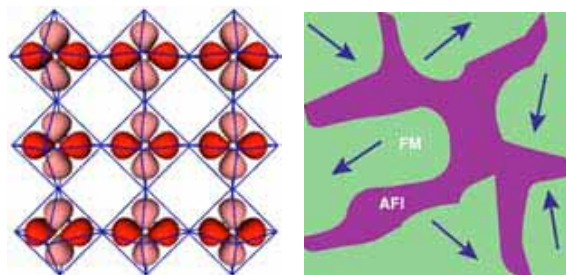


Fig. V.19 a) Lattice strain, e.g., arising from fluctuations in chemical doping, produces a slight local preference for a particular phase [23]. b) On a coarser scale, a small external perturbation, such as an applied magnetic field, can cause a non-linear, “giant” percolative change in the macroscopic conductivity [22].

Also the cuprate superconductors show a variety of nanoscale inhomogeneities (see Fig. V.20), including the charge-spin stripes mentioned at the beginning of this Chapter (see Fig. V.5 b). Although the importance of stripes to the mechanism of high-temperature superconductivity is in question, also these materials appear to exhibit a giant response: A S–N–S (superconductor –

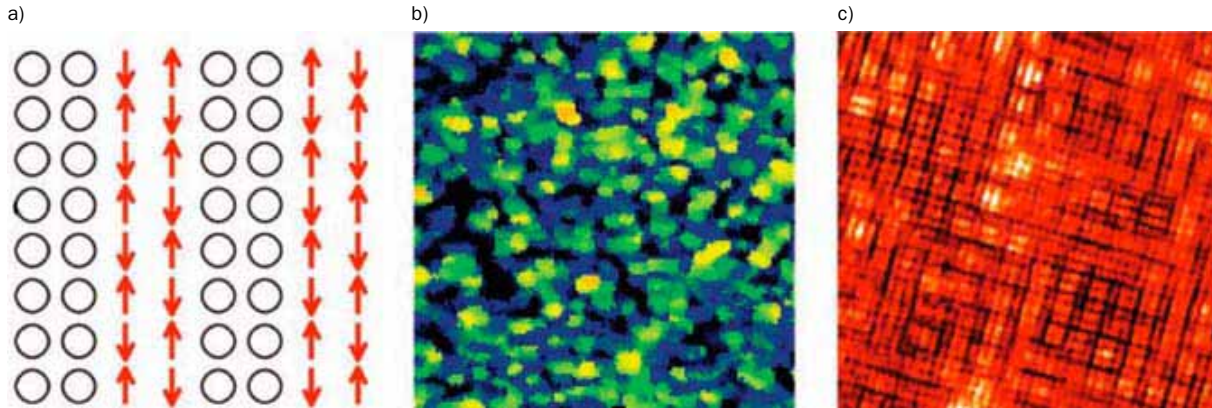


Fig. 20. Examples of nanoscale inhomogeneity in highly-correlated cuprate TMOs [22]. a) Idealized charge/spin stripes in cuprate superconductors, b) variations in the d -wave superconducting gap, detected in $\text{Bi}_2\text{Sr}_2\text{CaCu}_2\text{O}_{8+\delta}$ using scanning tunneling microscopy, c) a checkerboard charge-ordered state in a Na-doped cuprate.

normal conductor – superconductor) junction made of cuprate materials, whose N-layer thickness exceeds 100 coherence lengths, behaves as if it were a S-S Josephson junction, implying that the presence of neighboring superconducting material tips the balance in the thick N-layer to superconducting behavior [22].

In his paper, Dagotto draws parallels between correlated-electron materials and other forms of complex matter, such as polymers, liquid crystals and even bio-material. Just as groups of atoms in these soft materials form local solid patterns (i.e., molecules), which, when considered globally, exhibit complex, fluid behavior, so can, for example, Jahn-Teller-ordered regions in manganites lead to a complex electron liquid-crystal behavior, intermediate between an electron solid and an electron liquid. The analogy with biochemical systems (see Chapter IV) is striking: a large number of nearly degenerate states, with the corresponding entropic barriers, move on a rugged energy landscape. But a peculiarity of the electron-based complexity is that it is inherently quantum-mechanical [22].

The importance of the SwissFEL for investigating the spatial and temporal characteristics of such complex electron matter is twofold. Despite decades of work by a generation of scientists, a theoretical understanding of these materials is lacking. Fundamental approaches, like the Hubbard model (see Infobox), may be close to explaining microscopic features, such as the superconducting pairing mechanism, but they reach their limits when considering long-range interactions such as Coulomb and electron-lattice effects. Time-resolved struc-

tural and spectroscopic information from the SwissFEL may provide the experimental foundation for a new level of description of these materials, connecting microscopic mechanisms with macroscopic phenomenology, in the form of large-scale, numerical simulations. The second major SwissFEL contribution could be the development of practical applications of these fascinating materials: particularly relevant are dynamic effects such as non-linear switching between states of high and low conductivity, the coupling of magnetic and electric effects in the so-called “multiferroics” (see Infobox), dielectric effects in relaxor ferroelectrics and the development of oxide electronics, including TMO field-effect transistors and novel spintronic devices.

Summary

- *The charge, spin, orbital and lattice degrees of freedom of correlated electron materials lead to the inhomogeneous and dynamic coexistence of material phases with novel orderings. Prominent examples, the dynamic polarons in manganites and the charge-spin stripes in cuprates, have characteristic time and length scales (ps and nm) which are well-suited to be studied with the SwissFEL.*
- *Hard X-ray diffraction and the resonant soft-X-ray techniques of elastic diffraction and inelastic scattering provide high sensitivity to charge, spin, orbital and lattice degrees of freedom, in wavelength ranges covered by the SwissFEL. Furthermore, the SwissFEL will provide excellent access to the sub-ps dynamics of these degrees of freedom, either using laser-pump/X-ray probe experiments or by sampling equilibrium fluctuations via the intermediate scattering function $S(Q,t)$.*
- *Photoemission spectroscopy, a preferred technique for static studies of correlated electron materials in the laboratory and at synchrotrons, is poorly suited to time-resolved measurements at the SwissFEL, due to resolution degradation by electron space-charge effects. However, the sensitivity to electronic structure provided by the photon-in/photon-out X-ray absorption and resonant scattering techniques make them highly promising alternatives, particularly in single-shot mode.*
- *The nature of metal-insulator transitions in correlated-electron materials can be elegantly determined by time-resolved pump-probe experiments. In this way, the metal-insulator transition in 1T-TaS₂ is shown, by its ultrafast character (i.e., much faster than typical lattice vibrations), to be due to the electronic Mott-Hubbard transition, and not to the lattice-related Peierls instability.*
- *The electron-phonon interaction can be directly studied in time-resolved pump-probe experiments. Examples are the creation via hot electrons of coherent phonons in bismuth and the triggering of a dynamic metal-insulator transition by the IR-excitation of a particular phonon mode in Pr_{0.7}Ca_{0.3}MnO₃.*
- *In many respects, correlated-electron materials exhibit electronic complexity, characterized by glassy dynamics and giant responses to small external perturbations. This complexity is reminiscent of that of molecular systems, such as liquid crystals and even biological macromolecules. The ability of the SwissFEL to provide novel information over a large range of time and length scales makes it an ideal tool to establish an experimental foundation for a unification in the theory of correlated electrons at the micro- and macro-scales.*

References

- [1] Johnson, S., (private communication)
- [2] Bednorz, J. G. & Muller, K. A., "Possible High-Tc Superconductivity in the Ba-La-Cu-O System," *Zeitschrift Fur Physik B-Condensed Matter* **64**, 189-193 (1986).
- [3] Castleton, C. W. M. & Altarelli, M., "Orbital ordering in the manganites: Resonant x-ray scattering predictions at the manganese L-II and L-III edges," *Physical Review B* **62**, 1033-1038 (2000).
- [4] Lynn, J. W., Argyriou, D. N., Ren, Y., Chen, Y., Mukovskii, Y. M. & Shulyatev, D. A., "Order and dynamics of intrinsic nanoscale inhomogeneities in manganites," *Physical Review B* **76**, 01443-7 (2007).
- [5] Kivelson, S. A., Bindloss, I. P., Fradkin, E., Oganessian, V., Tranquada, J. M., Kapitulnik, A. & Howald, C., "How to detect fluctuating stripes in the high-temperature superconductors," *Reviews of Modern Physics* **75**, 1201-1241 (2003).
- [6] Als-Nielsen, J. & McMorrow, D. *Elements of Modern X-Ray Physics* (ed. Wiley) (2001).
- [7] Altarelli, M., "Resonant x-ray scattering: A theoretical introduction", *Lect. Notes Phys.* **697**, 201-242 (2004).
- [8] Lorenzo, J. E. (private communication)
- [9] Joly, Y. (private communication)
- [10] Ren, Y. H., Hu, Y. F., Li, Q., Hong, C. S., Hur, N. H. & Lupke, G. "Ultrafast collective dynamics of short-range charge/orbital ordering fluctuations in colossal magnetoresistive oxides", *cond-mat/0310360v1* (2003).
- [11] Schmitt, Th. (private communication)
- [12] Grubel, G., Stephenson, G. B., Gutt, C., Sinn, H. & Tschentscher, T., "XPCS at the European X-ray free electron laser facility," *Nuclear Instruments & Methods in Physics Research Section B-Beam Interactions with Materials and Atoms* **262**, 357-367 (2007).
- [13] Goodman, J. W. *Statistical Optics* (Wiley Classics Library, 2000).
- [14] Peierls, R. E. *Quantum Theory of Solids* (Oxford University Press, 2004).
- [15] Wolf, M. (private communication)
- [16] Perfetti, L., Loukakos, P. A., Lisowski, M., Bovensiepen, U., Wolf, M., Berger, H., Biermann, S. & Georges, A., "Femtosecond dynamics of electronic states in the Mott insulator 1T-TaS₂ by time resolved photoelectron spectroscopy," *New Journal of Physics* **10**, 053019 (2008).
- [17] Johnson, S. L., Beaud, P., Milne, C. J., Krasniqi, F. S., Zijlstra, E. S., Garcia, M. E., Kaiser, M., Grolimund, D., Abela, R. & Ingold, G., "Nanoscale depth-resolved coherent femtosecond motion in laser-excited bismuth," *Physical Review Letters* **100**, 155501(2008).
- [18] Murray, E. D., Fritz, D. M., Wahlstrand, J. K., Fahy, S. & Reis, D. A., "Effect of lattice anharmonicity on high-amplitude phonon dynamics in photoexcited bismuth," *Physical Review B* **72**, 060301 (2005).
- [19] Fritz, D. M., et al., "Ultrafast bond softening in bismuth: Mapping a solid's interatomic potential with X-rays," *Science* **315**, 633-636 (2007).
- [20] Rini, M., Tobey, R., Dean, N., Itatani, J., Tomioka, Y., Tokura, Y., Schoenlein, R. W. & Cavalleri, A., "Control of the electronic phase of a manganite by mode-selective vibrational excitation," *Nature* **449**, 72-74 (2007).
- [21] Cavalleri, A., (private communication)
- [22] Dagotto, E., "Complexity in strongly correlated electronic systems," *Science* **309**, 257-262 (2005).
- [23] Milhaly, L. http://solidstate.physics.sunysb.edu/talk/2004_dubrovnik2/.
- [24] Cheong, S-W. & Mostovoy, M., "Multiferroics: a magnetic twist for ferroelectricity", *Nature Materials*, **6**, 13-20 (2007).
- [25] Strocov, V., (private communication)
- [26] Abbamonte, P., (private communication)
- [27] Sekikawa, T., Kosuge, A., Kanai, T. & Watanabe, S., "Nonlinear optics in the extreme ultraviolet," *Nature* **432**, 605-608 (2004).
- [28] Gutt, C., (private communication)
- [29] Gutt, C., Stadler, L. M., Duri, A., Autenrieth, T., Leupold, O., Chushkin, Y. & Grubel, G., "Measuring temporal speckle correlations at ultrafast x-ray sources," *Optics Express* **17**, 55-61 (2009).
- [30] Baron, A. Q. R., Franz, H., Meyer, A., Ruffer, R., Chumakov, A. I., Burkel, E. & Petry, W., "Quasielastic scattering of synchrotron radiation by time domain interferometry," *Physical Review Letters* **79**, 2823-2826 (1997).
- [31] Palffy, A., "A Systematic Study of Nuclear Photoexcitation with X-Ray Laser Fields," *J. Modern Optics* **55**, 2603-2615 (2008).
- [32] Hubbard, J., "Electron Correlations in Narrow Energy Bands," *Proceedings of the Royal Society of London Series a-Mathematical and Physical Sciences* **276**, 238 (1963).
- [33] Scalettar, R. T., "Elementary Introduction to the Hubbard Model," <http://leopard.physics.ucdavis.edu/rts/p210/hubbard7.pdf>.

Machine and Building

SwissFEL Accelerator and Free Electron Laser

The FEL: a short introduction

In the free electron laser, the active laser medium is a beam of relativistic electrons (see Fig. M.1). This beam moves in vacuum through a periodic magnet array, called an undulator, forcing the electrons to follow a sinusoidal “wiggling” orbit. The wiggling orbit introduces a transverse velocity component, allowing the electrons to exchange energy with a light wave which is co-linear with the electron beam. The electrons become accelerated or decelerated, depending on the phase of the transverse electric field of the light wave. For a particular wavelength of the light, this exchange becomes resonant, leading to a continuous transfer of energy from the electrons to the light wave. The resonant wavelength is given by

$$\lambda = \frac{\lambda_U}{2\gamma^2} \left(1 + \frac{K^2}{2} \right)$$

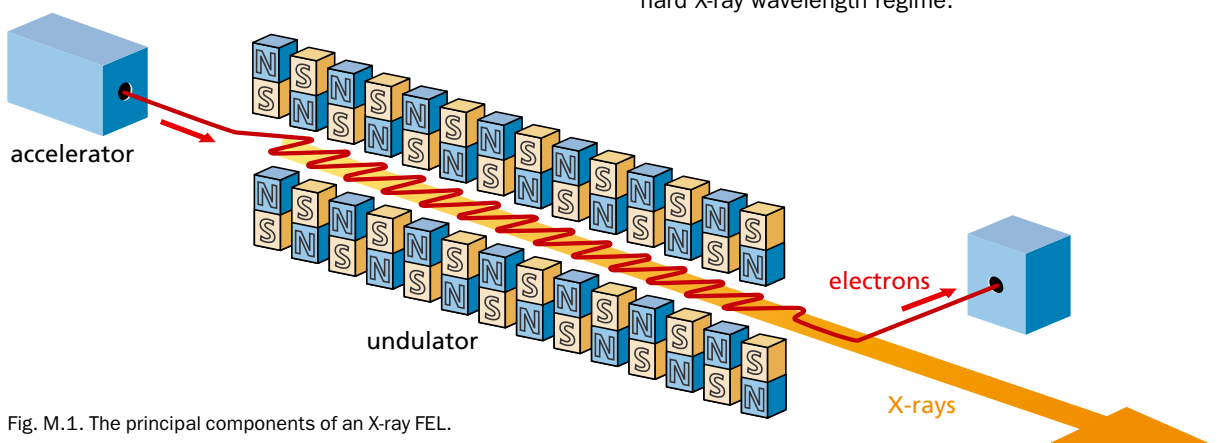


Fig. M.1. The principal components of an X-ray FEL.

where λ_U is the period length of the undulator and K is the undulator parameter, defined by

$$K = \frac{1}{2\pi} \frac{e}{mc} B_U \lambda_U$$

with B_U the peak magnetic field of the undulator. Since the path length of the electrons depends on the electron energy, the energy modulation induced by the radiation field is converted to a bunching of the electrons with the periodicity of the light wave. Thus the electrons are concentrated at the phase of the light wave where efficient energy transfer occurs, and the light wave becomes coherently amplified. As a result, the entire system acts analogously to a light amplifier in a conventional optical quantum laser. However, the FEL has the fundamental advantage that its operation does not depend on quantum transitions in a specific laser material. Therefore, the FEL scheme can be applied over a much wider photon wavelength range than the quantum laser principle (see Fig. M.2). Indeed, the FEL principle is the only proven method to provide coherent light pulses in the hard X-ray wavelength regime.

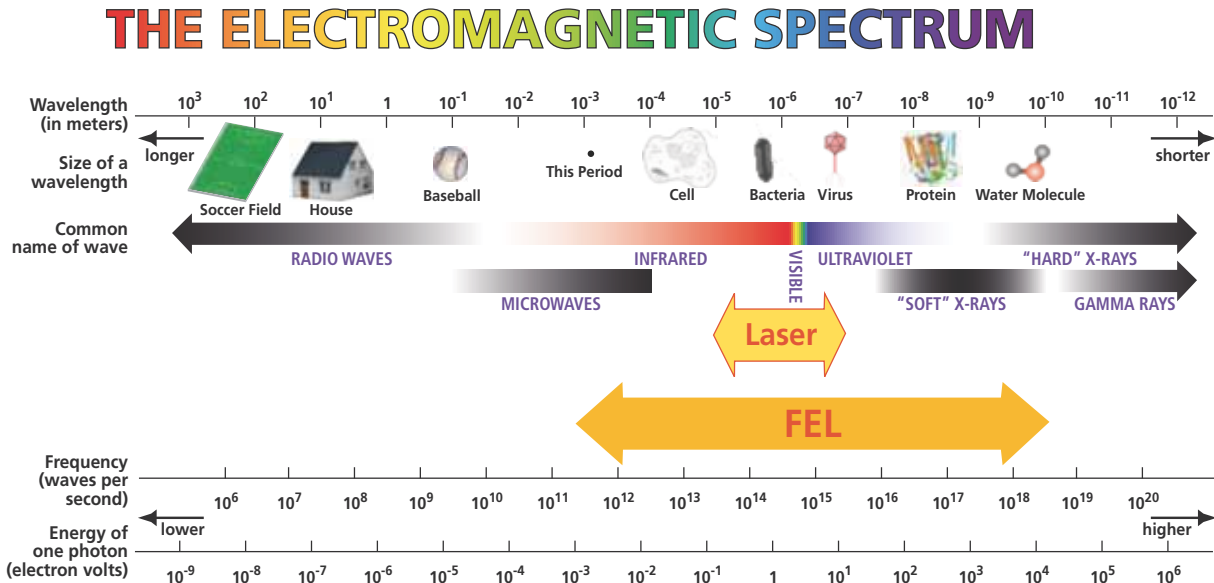


Fig. M.2. The wavelength range of a FEL vs. a quantum laser. Source: Advanced Light Source, Berkeley.

However, even the FEL scheme is faced with severe difficulties at these wavelengths. No mirrors with sufficient reflectivity exist, therefore the FEL cannot be built in an oscillator configuration but has rather to operate in a single-pass mode, requiring a large number of undulator magnets to drive the lasing process into saturation. Furthermore, no seeding source is readily available for these wavelengths. This latter problem is overcome by using the broadband signal from the shot-noise spectrum of the electron beam to start the amplification process. This type of FEL operation is called "self amplifying spontaneous emission" (SASE) and has recently been demonstrated to work for wavelengths as short as 1.5 Å [1]. There is worldwide research on alternative seeding methods at X-ray wavelengths, with the hope of achieving even better X-ray FEL performance. PSI is participating in this research, but SASE is presently the only proven method, and other approaches become increasingly difficult as the wavelength is made shorter. Another challenge arises from the requirement to maintain a good overlap between the electron beam and the light beam. Since the divergence of the light beam decreases inversely proportioned to λ , the demands on electron beam quality become more stringent at shorter wavelengths. The figure of merit for electron beam quality is the normalized emittance, which is given by the "surface" occupied by the beam particles in a plane spanned by the deviation in the transverse position from the nominal orbit and the deviation in the transverse

momentum from the nominal momentum direction. The normalized emittance is conserved under beam acceleration and therefore depends mainly on the performance of the electron injector. This makes the design of the injector a particularly challenging task for X-ray FELs. Optimum matching of the electron beam to the light beam can be achieved if the condition

$$\varepsilon_N \leq \gamma \frac{\lambda}{4\pi}$$

is met, where ε_N is the normalized emittance, γ is the relativistic factor, proportional to the electron energy, and λ is the lasing wavelength. Present injector technology requires the acceleration of electrons to very high energy in order to operate a FEL in the X-ray regime. However, it has been demonstrated that FELs can function with reduced efficiency even if the normalized emittance exceeds this optimum condition by a factor 4–5. In spite of this, progress in injector performance is very desirable until this condition is met. A very good introduction to the theory of FELs, with emphasis on short wavelength facilities, can be found in Ref. [2].

Design Rationale

The SwissFEL baseline design aims to produce FEL pulses covering the wavelength range 1 Å to 70 Å (0.1–7 nm) with a compact and economic design, which is affordable on the scale of a national laboratory (see

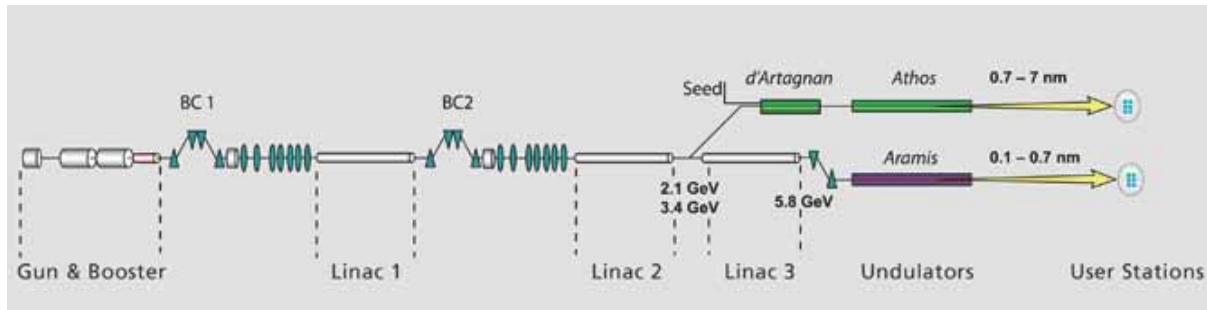


Fig. M.3. A schematic overview of the SwissFEL facility, with its main components.

Fig. M.3). The overall cost of a linear accelerator depends strongly on the final beam energy, therefore a key design goal is to minimize the required electron beam energy for a given radiation wavelength. With the dependence of photon beam wavelength on electron beam energy and undulator period discussed in the previous section, this implies the use of an undulator with a short period length and a rather low K value. The emittance achievable with the injector puts another lower limit on the beam energy. Both constraints are most stringent for the shortest lasing wavelength.

Based on these factors, and considering the best performance achievable with leading-edge undulator and electron injector technology, the following parameters were chosen to achieve lasing with the SwissFEL at 1 Å wavelength:

Parameters for lasing at 1 Å

Beam energy	5.8 GeV
λ_U	15 mm
K	1.2

The Injector

The baseline technology for the SwissFEL electron injector relies on the radio-frequency (RF) gun photo-injector concept. A photocathode placed in a high-field RF cavity is illuminated with a short laser pulse. The timing of the laser pulse is synchronized to the RF, so that electrons are emitted when the accelerating RF field on the cathode reaches an optimum value. For the past two decades, RF gun technology has been the subject of intense R&D activities at various leading accelerator laboratories worldwide, and remarkable progress has been achieved. The present state-of-the-art allows the production of

electron pulses of 200 pC charge, with normalized emittances below $0.4 \mu\text{m}$. This is sufficient to operate the SwissFEL at nominal wavelength and beam energy. Figure M.4 shows the design of the RF gun for the SwissFEL.

However, to reach these parameters, the pulses produced from the gun must be much longer, typically several ps, than the final pulse of a few fs required in the FEL. Therefore, the pulse has to be longitudinally compressed in the linear accelerator, downstream from the injector.

An improved performance could be achieved with an injector providing an electron beam of even smaller emittance. Therefore PSI is conducting R&D on an alternative injector solution. This design relies on a cathode consisting of a field-emitter array (FEA), structured on the nanometer length scale (see Fig M.5), and placed in a pulsed diode with a very high electric extraction field. Such a field-emitter array should allow emission of electrons with a very high current density and very small momentum spread, thus providing a beam with very small emittance. The SwissFEL design foresees the possibility to replace the RF gun of the baseline configuration once the FEA-diode concept has demonstrated stable production of beams with a quality superior to the baseline configuration.

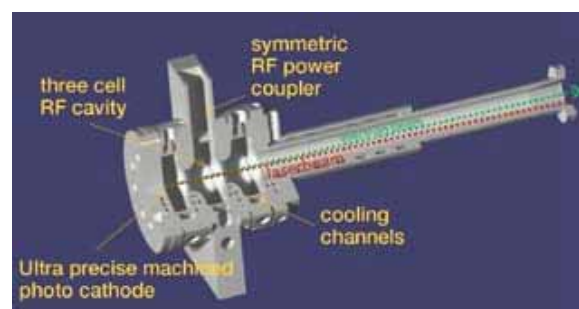


Fig. M.4. Design of the SwissFEL RF gun.

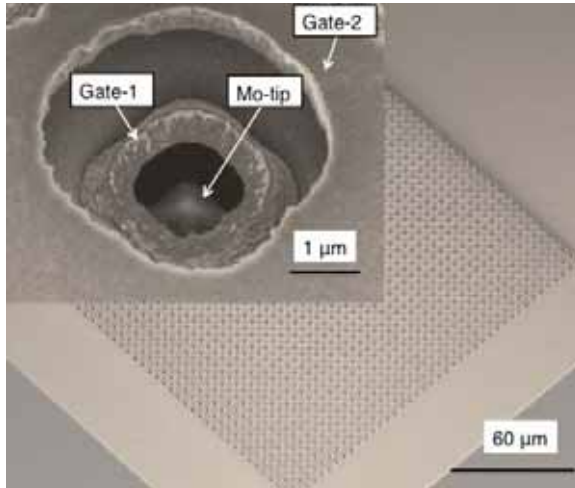


Fig. M.5. A prototype of the PSI field-emitting array electron source.

The Accelerator

The SwissFEL linear accelerator (linac) must fulfill two functions:

- acceleration of the electron pulse from the injector to the nominal energy of the FEL
- time compression of the electron pulse from 5 ps r.m.s. to 25 fs r.m.s

The demands for compactness and economy suggest the use of a normal-conducting, pulsed RF system for acceleration, with rather high accelerating fields. A key design parameter for such a linac is the total RF energy supplied per pulse by the RF transmitters to the accelerating cavities. This parameter strongly influences the

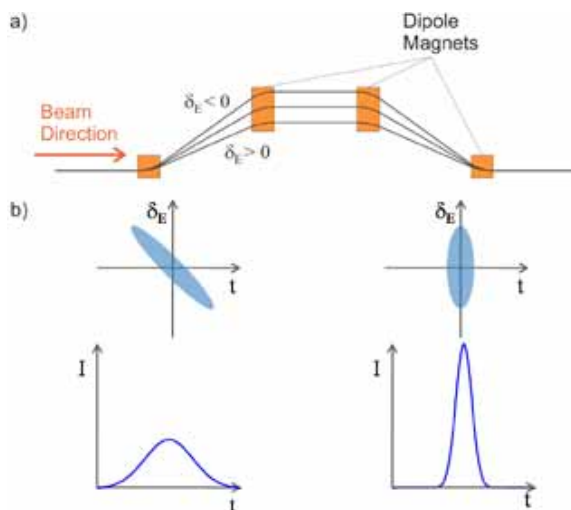


Fig. M.6. a) A magnetic chicane bunch compressor. b) The rotation of electrons in the energy – time plane.

investment cost and electric power consumption of the overall facility and can be minimized either by reducing the local accelerating field or by increasing the RF frequency. Since reducing the field increases the overall facility length, an increase of the RF frequency is the more promising approach. However, such an increase goes together with a decrease in the size of the accelerator components, thus leading to even tighter mechanical and electrical tolerances. In contrast to most normal-conducting electron linear accelerators nowadays, which operate at an RF frequency of 3 GHz, the SwissFEL foresees the use of a 6 GHz RF system. It will be the first large-scale linac of this type in Europe.

A drawback of the normal-conducting approach compared to superconducting RF systems is a considerably lower average accelerated beam current, and as a consequence, a smaller average photon flux to the experiments. This drawback is partly balanced by a more even distribution of pulses in time compared to the superconducting linac. Such an even distribution can be a major advantage for experiments with complex detector systems and/or requiring mechanical adjustments between pulses.

For temporal pulse compression, two magnetic chicanes are placed in the linac at 450 MeV and 2 GeV. The electron pulse is accelerated in the linac slightly off the crest of the RF wave. This introduces a time/energy chirp along the pulse. The energy dependence of the electron path length in the magnetic chicane leads to a time compression, as depicted in Figure M.6.

The FEL

Two SASE FEL lines will be driven by the linac: a hard X-ray FEL named “Aramis” and a soft X-ray line named “Athos”. Aramis, with the undulator parameters given in Table 1, covers the wavelength range 1–7 Å, and Athos the wavelength range 7–70 Å.

For Aramis, a planar undulator will be used, consisting of an array of NdFeB permanent magnets mounted in a vacuum tank. To reach the required parameters, the inter-magnet gap available for the beam can only be 4.5 mm. Very recent developments in permanent magnet technology allow the operation of such an undulator at room temperature, thus avoiding a costly liquid nitrogen cooling system, as is required by existing undulators with comparable parameters. A total of 12 undulator modules, each 4 m long, have to be aligned within tight tolerances to reach the SASE saturation regime.

For the Athos FEL, the undulator parameters are more relaxed, and the permanent magnet arrays can therefore be situated outside the of the vacuum chamber. This undulator is built in the so-called APPLE II configuration, which allows for full control of the FEL polarization and wavelength by adjusting the mechanical position of the magnet arrays with high precision. Movements with submicron accuracy must be performed in the presence of very strong magnetic forces, making the mechanical design of the mover systems particularly challenging. Again, 12 undulator modules, 4 m each, are needed to reach the SASE saturation regime. Polarization control will be particularly advantageous for magnetization dynamics experiments, as discussed in Chapter I of this document.

Furthermore, it is foreseen to operate the Athos FEL with seeding by an optical laser system (see Chapter III). Such a seeding scheme allows narrowing the spectral width of the FEL radiation by an order of magnitude, providing full longitudinal coherence and an increased overall brightness. However, despite of its obvious attractiveness, FEL seeding at these short wavelengths is a yet unproven technology, and considerable R&D with as yet uncertain outcome is still required in order to apply it to the SwissFEL. The subject of FEL seeding is a strong focus of FEL R&D worldwide, with PSI playing a prominent role in both theoretical modeling and technical developments. Nevertheless, without an experimental proof of feasibility, the SwissFEL baseline design

will rely on SASE operation for both FEL lines.

Parameters and schematic layout

Key parameters of the SwissFEL are summarized in Table 2.

Key parameters of the SwissFEL

Overall length (incl. experimental hall)	800 m
Total electric power consumption	3.8 MW
Electron beam energy	5.8 GeV
Technology of linear accelerator	Normal-conducting copper cavities at 6 GHz
Charge per electron pulse	0.2 nC
Normalized beam emittance	0.4 mm·mrad
Number of X-ray pulses per second	200 (100 at each photon beamline)
X-ray pulse duration	24 fs
X-ray brilliance	$1.3 \cdot 10^{33}$ photons/ (s·0.1%·b.w.·mm ² ·mrad ²)
Shortest lasing wavelength	0.1 nm

Building

The facility, with a total length of 800 meters, consists of the following sections:

- Electron injector and accelerator tunnel
- Undulator and photon transport hall
- Experimental hall.

An overview drawing of the building is depicted in Figure M.7, and cross-sections at two positions are shown in Figures M.8 and M.9. The tunnel in which the first two sections will be installed is built underground on a gravel base, with sufficient wall thickness to provide radiation protection. Due to safety and operational considerations, the accelerating power supplies and the beam steering and control units will be placed in five technical buildings on top of the tunnel, above ground, to allow easy access. A sixth building, also above ground, will be used as a preparation and development area for the undulator modules.

The facility infrastructure (general electrical installations, water cooling and air conditioning units) will be situated on one side of the technical buildings. Services will be provided through a transport runway connecting the technical buildings. Connection between the tunnel and the technical buildings is provided by three material transportation openings and by three staircases, which also serve as emergency escape routes.

Special care will be taken to provide a very low vibration level and a high temperature stability. The vibration noise must be lower than 0.2 microns in the frequency range from 0.3 to 100 Hz, and temperature variation during operation must be below 0.1° during operation.

The experimental hall will offer space for up to six beamlines of different lengths. Depending on the photon energy range, the experimental stations will be installed inside of lead-shielded cabins. Space is also reserved for the installation of ancillary equipment such as optical lasers, a terahertz pump source and preparatory space for experiments. The required temperature stabilization will be performed in two stages: a global scheme, to several °C, and dedicated systems in experimental cabins with more stringent requirements. Provision is made for future expansion to longer beamlines.

On one side of the experimental hall, space is reserved for sample preparation laboratories, computer servers and office space for users and visitors. An overview of the relevant building volumes is given in Table M.2.

The logistic installations (supply and disposal) will be connected to the existing infrastructure of PSI. For ecological reasons, facility cooling will be performed using both ground and river water. At present, two site locations near the PSI campus are under consideration for the SwissFEL facility.

Volume [m ³]	Accelerator and Experimental hall	Infrastructure	Logistics	Sum
Underground	41'000	0	5000	46'000
Overground	0	30'000	9000	39'000
Sum	41'000	30'000	14'000	85'000

Table M.2. Building volumes of the SwissFEL facility

References

- [1] Paul Emma et al., "First lasing of the LCLS X-ray FEL at 1.5 Å," *proc. of Particle accelerator conf.*, Vancouver, 2009.
- [2] Peter Schmüser, Martin Dohlus, Jörg Rossbach, "Ultraviolet and Soft X-Ray Free-Electron Lasers: Introduction to Physical Principles, Experimental Results, Technological Challenges," *Springer Tracts in Modern Physics*, 2008.

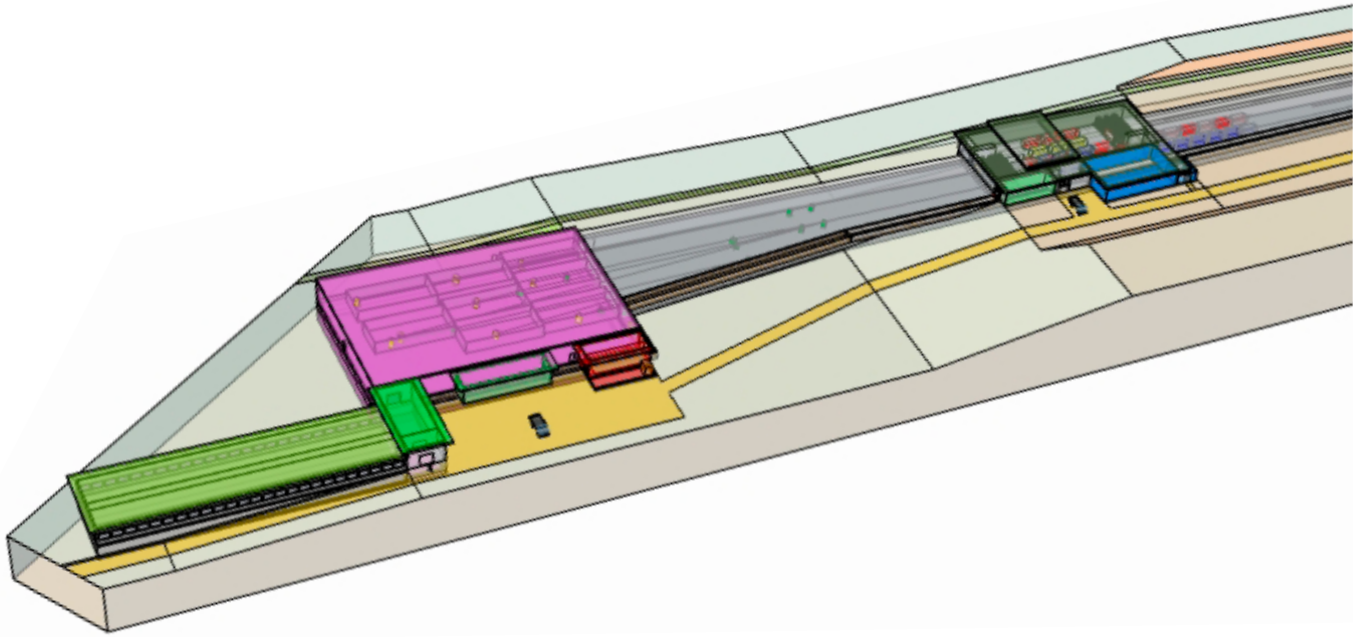


Fig. M.7. General layout showing the accelerator and undulator tunnel, the experimental hall, the laboratory building and the technical buildings.

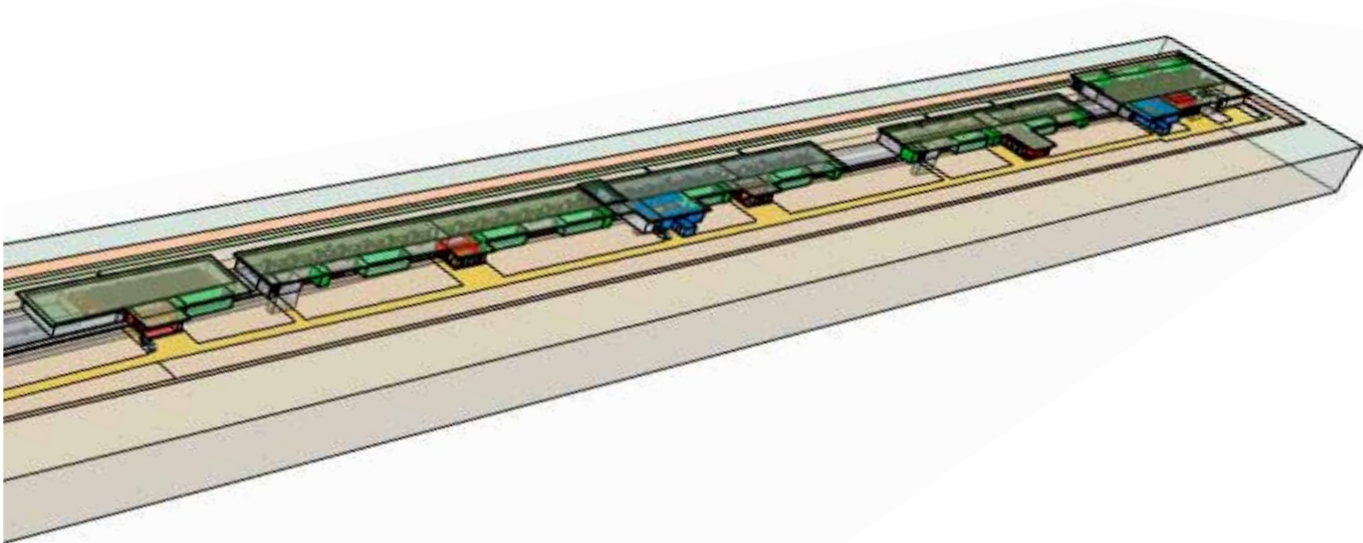


Fig. M.8. Cross-section of the accelerator, with the underground accelerator tunnel and the above-ground building for the RF-power supplies.

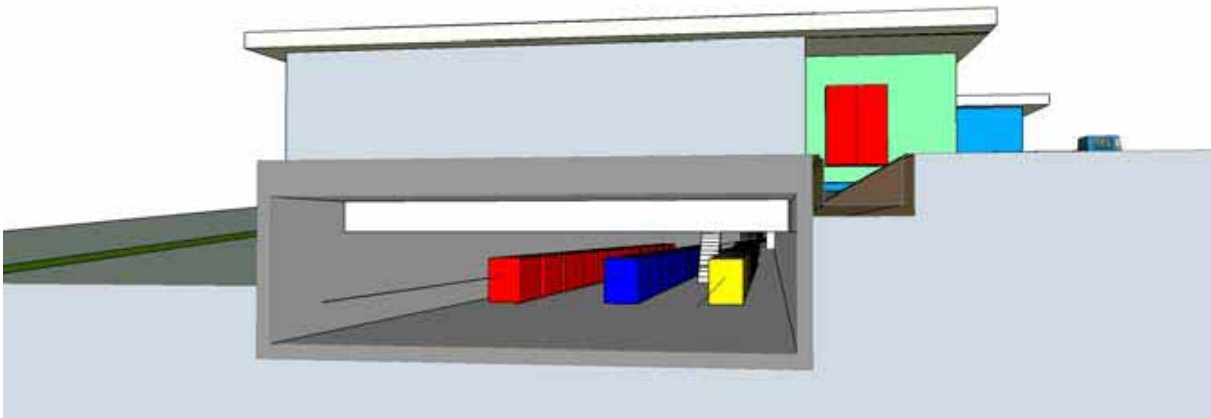


Fig. M.9. Cross section of the undulator hall.

Appendix A:

The SwissFEL Science Workshop Series

Information Day on the Use of X-Ray Free Electron Lasers, Bern, 20.4.07

R. Eichler (PSI)	Introduction
A. Wrulich (PSI)	“The PSI-XFEL project”
M. Chergui (EPFL)	“Ultrafast X-ray science with free electron lasers”
R. Falcone (Berkeley)	“Research needs for a new generation of X-ray sources”
“Ideas for use of an XFEL”	V. Sandoghdar (ETHZ)
	F. Pfeiffer (PSI)
	H.W. Fink (Uni ZH)
	M. Schiltz (EPFL)
	T. Richmond (ETHZ)
	P. Hamm (Uni ZH)
	G. Ingold (PSI)
	T. Feurer (Uni BE)
	C. Bressler (EPFL)
	A. Devaux (Uni BE)

Nanoscale Magnetization Dynamics, Bern, 5.6.08

Rolf Allenspach (IBM):	“XFEL for Magnetism Studies”
Riccardo Hertel (Jülich):	“Magnetic vortex core dynamics – ultrafast and small”
Harald Brune (EPFL):	“Open Issues in Magnetic Nanostructures”
Pietro Gambardella (Barcelona):	“Magnetic spectroscopy @ XFEL”
Christian Back (Regensburg):	“Laser Induced Magnetization Dynamics”
Michel Kenzelmann (ETHZ, PSI):	“Nanoscale Magnetization Dynamics”
Christoph Quitmann (PSI):	“Ideas for XFEL Science – Magnetization Dynamics”
Henrik Rønnow (EPFL):	“Mesoscopic dynamics in correlated electron materials – XFEL dreams”
Andreas Vaterlaus (ETHZ):	“Magnetism far from equilibrium probed with Spin Polarized Photoemission”

Sub-ps Solution Chemistry and Surface Catalysis, Lausanne, 10.10.08

Martin Nielsen (Copenhagen):	“Time-resolved X-ray scattering of an electronically excited state in solution”
Markus Meuwly (Uni Basel):	“Rapid Processes in [Biophysical] Chemistry”
Jaques-E. Moser (EPFL):	“Dynamics of light-induced interfacial electron transfer”
Emad Aziz (BESSY):	“Toward Ultra-Fast Dynamics in Solutions”
Chris Milne (PSI):	“Ultrafast x-ray spectroscopies for the study of structural dynamics in molecular systems”
Martin Wolf (F-U Berlin):	“Ultrafast surface femtochemistry and electron-phonon coupling”
Christian Bressler (EPFL):	“Exploiting Hard X-Ray Spectroscopies at XFELs”
Burkhard Zietz (EPFL):	“Simulated scattering in solution”
Jeroen van Bokhoven (ETHZ):	“Structure of catalytically active sites”
Nikolas Bukowiecki (EMPA):	“Bulk analysis of solids using XRF”
Markus Amman (PSI):	“Can a XFEL shed light on atmospheric particles?”
Gregor Knopp (PSI):	“Prospective experiments on catalytic surfaces”

Coherent Diffraction by Nanostructures, Bern, 27.11.08

Franz Pfeiffer (PSI and EPFL):	“Coherent Diffractive Imaging at future XFEL sources”
Clemens Schulze-Briese (PSI):	“Current Limitations on Synchrotron-Based Protein Crystallography”
Xiao Dan Li (PSI):	“Understanding membrane protein function: present and future”
Cameron Kewish (PSI):	“2-D Membrane Protein Crystallography at Future XFELs”
Abbas Ourmazd (Wisconsin):	“Determining the Structure of Biological Molecules & Nanoparticles”
Helena van Swygenhoven-Moens (PSI and EPFL):	“PSI-XFEL science on interface-dominated metals”
Ana Diaz (Grenoble):	“Applications of Coherent Diffraction to Semiconductor Nanostructures”
Ian Robinson (UC London):	“XFEL diffraction investigation of shock waves”

Ultrafast Biochemistry, Basel, 28.1.09

Marten Vos (Palaiseau):	“Femtosecond biology”
Jasper van Thor (IC London):	“Time resolved pump-probe studies of structural dynamics of light sensitive proteins“
Martina Havenith (Bochum):	“Terahertz excitation of biomolecules”
Maurice Goeldner (Strasbourg):	“Phototriggers in biology”
Alexandre Specht (Strasbourg):	“X-ray methodologies using caged compounds“
Ben Schuler (Uni ZH):	“Protein Folding Dynamics from Single Molecule Fluorescence Spectroscopy“
Miguel Rubi (Barcelona):	“Exploring mesoscopic scales through Mesoscopic Non-Equilibrium Thermodynamics”

Crazy Ideas and Challenges: Science Issues, Villigen, 27.2.09

Gerhard Ingold (PSI):	“Towards Pump-Probe Resonant Diffraction: 100-10 fs“
Christian Spielmann (Jena):	“Femtosecond X-ray science”
Sebastian Doniach (Stanford):	“2-wave mixing in Mössbauer Crystals“
Alexandr Chumakov (Grenoble):	“XFEL spectroscopy at the Mössbauer resonance“
Matthias Hengsberger (Uni ZH):	“Time-resolved photoelectron spectroscopy at x-ray energies using a time-of-flight spectrometer with spin analysis“
Peter Abbamonte (Illinois):	“Inelastic x-ray scattering with [crazy] coherent FEL pulses“
Malcolm Howells (Berkeley):	“Toward a Modern Version of Fluctuation Scattering“

Time-Resolved Spectroscopy on Correlated Electron Materials, Zurich, 6.3.09

Frederic Mila (EPFL):	“Correlated electron systems and XFEL”
Bertram Batlogg (ETHZ):	“Electron Correlation – Materials”
Urs Staub (PSI):	“Time Dependent Resonant Soft X-Ray Diffraction“
Hugo Dil (Uni ZH, PSI):	“Time, Spin, Space and Angle Resolved Photoemission on correlated (and other) systems“
Thorsten Schmitt (PSI):	“Pump and Probe Resonant Inelastic X-Ray Scattering at a Soft X-Ray FEL“
Steve Johnson (PSI):	“Femtosecond x-ray diffraction”
Paul van Loosdrecht (Groningen):	“Correlated matter - Time resolved optics“
Dirk van der Marel (Uni GE):	“THz spectroscopy: Polaron liquid in electron doped strontium titanate“

Appendix B:

Current SwissFEL Research Projects

List of XFEL-related PhD and student thesis projects

	Thesis-Title	Status	Funding source	University & Institute	Supervising Professor	PSI	Name of student
1	Femto Second Bunch Slicing Diagnostics Using Coherent Synchrotron Radiation and Development of a Non-Destructive Bunch Length Monitor Based on Coherent Diffraction Radiation	ongoing	SNF	Universität Bern	Thomas Feurer	Volker Schlott, Bernd Steffen, Stefan Hunziker	Felix Mueller
2	Development of a Residual Gas Photon Beam Monitor with Microstrip Detector	ongoing	PSI	Universität Zürich	Bruce Patterson	Michael Boege, Andreas Streun, Volker Schlott	Thomas Wehrli
3	Femto-Second Bunch Slicing Diagnostic and Electron Bunch Length Measurements with Coherent Synchrotron Radiation at the Swiss Light Source	ongoing	n.a. (Diplomarbeit)	Technische Universität Berlin	Thomas Moeller	Volker Schlott, Gerhard Ingold, Paul Beaud	Dirk Abramssohn
4	Development of high-brightness and low-emittance cathode based field-emitter arrays with controlled 10 nm-scale apex sizes	approved	PSI	Universität Zürich	Hans-Werner Fink	Soichiro Tsujino	n.a.
5	Femtosecond electron dynamics and nano-optic enhancement in laser-triggered field-emission from metallic nano-tip arrays with controlled apex-sizes	Submitted to SNSF	n.a.	Universität Bern	Thomas Feurer	Soichiro Tsujino, Paul Beaud, Thomas Feurer, Benedikt Oswald	n.a.

6	Resonant lossy electromagnetic structures	ongoing	SNF	ETHZ	Peter Arbenz	Benedikt Oswald	Hua Guo
7	A Self Consistent Particle-In-Cell Finite-Element-Time-Domain Solver for Large Accelerator Structures	ongoing	50% PSI	ETHZ D-INFK	Peter Arbenz	Andreas Adelman	Marcus Wittenberger
8	Simulation of Low Emittance Beam Transport at High Energies including Radiation	ongoing	50% PSI 25% ETHZ 25% CSCS	ETHZ D-INFK, Wissenschaftliches Rechnen	Peter Arbenz	Andreas Adelman	Christof Kraus
9	Multi Objective Optimisation of the 250 MEV XFEL Injector	FOKO passed / IBM? Start April 200?	50% IBM 50% PSI	ETHZ Institute for computational science	Peter Arbenz	Andreas Adelman	Yves Ineichen
10	Low-emittance electron gun development and non-relativistic laser-assisted electron bunch characterization	approved	SNF	Universität Bern	Thomas Feurer	Christoph Hauri	n.a.
11	Emittance measurements at LEG (internship)	Completed 2008	PSI	Universität Basel	Bruce Patterson	Romain Ganter	Stefan Binder
12	In-situ studies of the nanocrystallization of proteins with dynamic light scattering (internship)	Completed 2008	PSI	Universität Basel	Bruce Patterson	Bruce Patterson	Kei Mikami
13	Dynamic light scattering simulation of split-pulse XPCS	Completed 2008	PSI	Universität Zürich	Bruce Patterson	Bruce Patterson	Anastija Ichsanov
14	An ultra low emittance electron gun for the PSI-XFEL: design and construction	Completed 2008	SNF and PSI (50/50)	ETHZ	Ralph Eichler	Marco Pedrozzi	Kevin Shing Bruce Li
15	Development of a Multi Channel RF Field Detector for the LLRF Control of the Free Electron Laser at Hamburg	Completed 2008	BBW-Nr.: 03.0611-1 (Bundesamt für Bildung und Wissenschaft) CARE	Technische Universität Hamburg Harburg	K. Schuene-mann (Uni) Stefan Simrock (DESY)	Thomas Schilcher	Matthias Hoffmann
16	Characterization of electron bunches from field emitter array cathodes for use in the next-generation X-ray Free Electron Lasers	Completed 2007	PSI	EPFL	Albin Wrulich	Andreas Streun, Åke Andersson, Volker Schlott	Simon Christian Leemann
17	Single-Shot Electron Bunch-Length Measurements with a Spatial Electro-Optical-Auto-Correlation Interferometer using Coherent Transition Radiation at the 100 MeV SLS pre-injector LINAC	Completed 2006	SNF	ETHZ	Ralph Eichler	Volker Schlott	Daniel Oliver Sütterlin
18	Simulation of electron source for next-generation X-ray free-electron laser	Completed 2005	PSI/SNF/ETHZ	ETHZ	Matthias Troyer	Micha Dehler	Arno Erol Candel

Published by
Paul Scherrer Institut

Coordination
Rafael Abela

Design and Layout
Irma Herzog

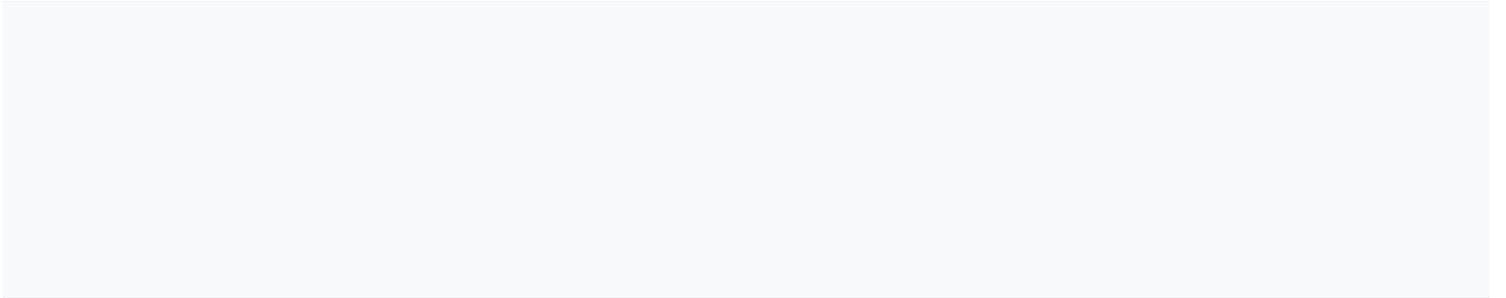
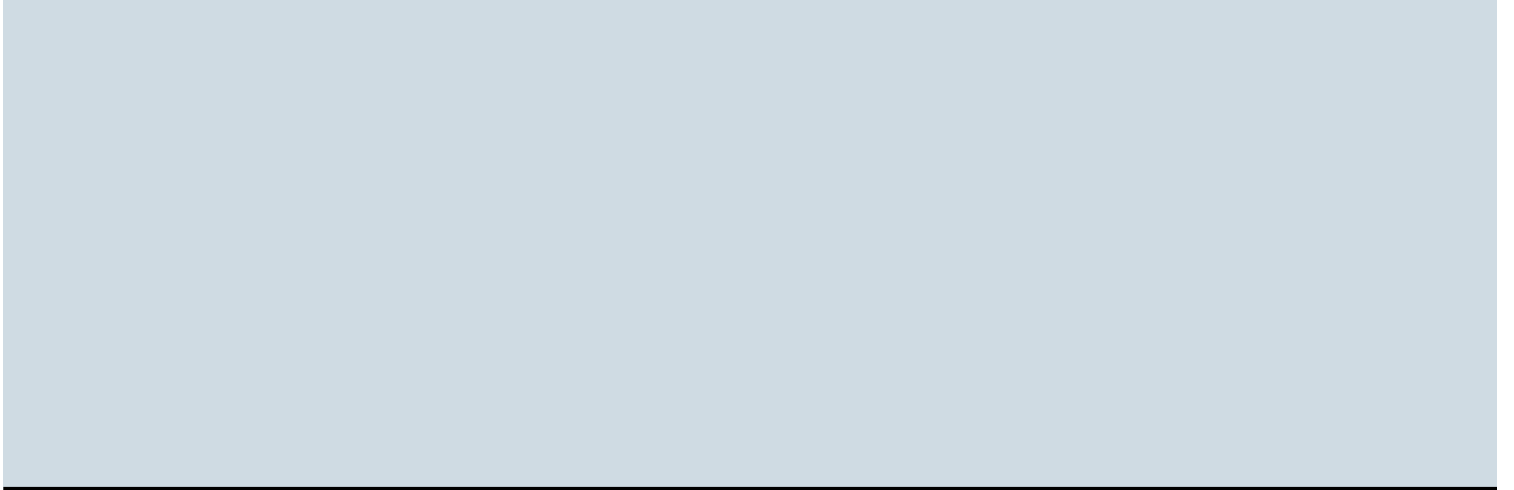
Photographs
© Paul Scherrer Institut

Printing
Paul Scherrer Institut

Available from
Paul Scherrer Institut
Communications Services
5232 Villigen PSI, Switzerland
Phone +41 (0)56 310 21 11
www.psi.ch

PSI public relations
pubrel@psi.ch

Copying is welcomed, provided
the source is acknowledged
and an archive copy sent to PSI.
Paul Scherrer Institut
September 2009



PAUL SCHERRER INSTITUT



Paul Scherrer Institut, 5232 Villigen PSI, Switzerland
Tel. +41 (0)56 310 21 11, Fax +41 (0)56 310 21 99
www.psi.ch